A 3-dimensional Analysis of the Cassiopeia A Supernova Remnant

A DISSERTATION
SUBMITTED TO THE FACULTY OF THE GRADUATE SCHOOL
OF THE UNIVERSITY OF MINNESOTA
BY

Karl Andrew Isensee

IN PARTIAL FULFILLMENT OF THE REQUIREMENTS
FOR THE DEGREE OF
Doctor of Philosophy

Lawrence Rudnick

September, 2011

Acknowledgements

A work of this magnitude is not possible without the support of many individuals. I would like to explicitly acknowledge many of the people who provided the most support, but there are many others who provided invaluable assistance to me over the years.

First and foremost, I would like to thank my family, especially my parents Kerry and Karen Isensee and my sister Kristen, for all their support over the years. Without their encouragement I would not have even started on the long path that has eventually lead to this work.

I'd also like to acknowledge all the invaluable assistance from my adviser, Dr. Lawrence Rudnick. His constant feedback was critical in my development as a scientist. He taught me how to ask (and sometimes even answer!) the important questions, and without his wisdom, this work would not have been possible.

Of course, there are many others who provided valuable scientific feedback. Dr. Tracey DeLaney was especially helpful - not only did my work build upon her previous results, but she provided huge amounts of feedback on my own research. Dr. Alexander Heger was also critical in helping me understand the mysterious inner workings of massive stars and supernova explosions.

Finally, I'd like to acknowledge all the support (both scientific and psychological) that I've received from fellow graduate students over the years. I'd like to especially thank Damon Farnsworth and Steven Warren, who were quite willing to vigorously discuss the smallest detail of my work.

Dedication

For my parents, who provided me with so much support over the years

Abstract

We present a multi-wavelength study of the nearby supernova remnant Cassiopeia A (Cas A). Easily resolvable supernova remnants such as Cas A provide a unique opportunity to test supernova explosion models. Additionally, we can observe key processes in the interstellar medium as the ejecta from the initial explosion encounter Cas A's powerful shocks.

In order to accomplish these science goals, we used the *Spitzer Space Telescope*'s Infrared Spectrograph to create a high resolution spectral map of select regions of Cas A, allowing us to make a Doppler reconstruction of its 3-dimensional structure structure. In the center of the remnant, we find relatively pristine ejecta that have not yet reached Cas A's reverse shock or interacted with the circumstellar environment. We observe O, Si, and S emission. These ejecta can form both sheet-like structures as well as filaments. Si and O, which come from different nucleosynthetic layers of the star, are observed to be coincident in some regions, and separated by $>$500 km s^{-1} in others. Observed ejecta traveling toward us are, on average, $\sim$800 km s^{-1} slower than the material traveling away from us. We compare our observations to recent supernova explosion models and find that no single model can simultaneously reproduce all the observed features. However, models of different supernova explosions can collectively produce the observed geometries and structures of the emission interior to Cas A's reverse shock. We use the results from the models to address the conditions during the supernova explosion, concentrating on asymmetries in the shock structure. We also predict that the back surface of Cassiopeia A will begin brightening in $\sim$30 years, and the front surface in $\sim$100 years.

We then used similar observations from 3 regions on Cas A's reverse shock in order to create more 3-dimensional maps. In these regions, we observe supernova ejecta both immediately before and during the shock-ejecta interaction. We determine that the reverse shock of the remnant is spherical to within 7%, although the center of this sphere is offset from the geometric center of the remnant by 810 km s^{-1}. We determine that the velocity width of the nucleosynthetic layers is $\sim$1000 km s^{-1} in a given region, although the velocity width of a layer along any given line of sight is $<$250 km s^{-1}. Si and

O are observed to be coincident in some directions, but segregated by up to $\sim$500 km s^{-1} in other directions. We again compare these observations of the nucleosynthetic layers to predictions from supernova explosion models in an attempt to constrain such models. Finally, we observe small-scale velocity structures in the recently shocked ejecta. We determine that this corrugation is likely caused during the supernova explosion itself, rather than hundreds of years later at the remnant's reverse shock.

Finally, we present a detailed multi-epoch X-ray analysis of Cas A using *Chandra X-ray Observatory* exposures from 2000, 2002, and 2004. We identify the most recently shocked X-ray ejecta with ionization timescales of $\sim 10^{10}$ cm^{-3} s, nearly an order of magnitude smaller than previously identified shocked ejecta. These ejecta are then used to determine if the original nucleosynthetic layers of the star are arriving at Cas A's reverse shock at different times. We use recent collisional ionization models that allow us to correlate observed changes in spectrum with a rough estimate of when the Mg and Fe layers reached the reverse shock. We find several regions that have a signature consistent with a separation of $\sim$200 km s^{-1} between layers, although we find that most regions show no sign of separation greater than 65 km s^{-1}. This method is able to detect substantially smaller separations between layers than earlier X-ray techniques. We test various supernova explosion models against our observations by comparing our observed velocity separation between layers to predictions from the models. We conclude that any mixing between nucleosynthetic layers is most likely caused by Rayleigh-Taylor filamentation and not partial explosive nucleosynthesis in the layers. Our observations of spectral changes provide feedback for future models which will address important physical issues such as the role of cosmic ray production at a supernova remnant's reverse shock.

Contents

List of Tables

List of Figures

Chapter 1

Introduction

Stars that explode as supernovae are fundamental to the evolution of the universe. They strongly influence the formation of newer generations of stars and create most of the elements in the periodic table, including necessary elements for life. The energy from the explosion itself, as well as winds and radiation from the progenitor star, heavily modify the interstellar medium (ISM) and affect the evolution of the host galaxy. The explosion itself is also a unique laboratory that provides insights into physics not observable elsewhere in the universe.

Supernova remnants, the remains of such a supernova explosion usually seen years to hundreds of thousands of years later, are key to understanding supernovae because they are one of the best ways of learning about the initial explosion. Supernova explosions themselves are rare in our own galaxy, occurring perhaps once every 30 years on average. Supernovae are now observed in other galaxies at a rate of about one a day, but can almost never be spatially resolved, making detailed studies difficult. But supernova remnants in our own galaxy allow for reconstructions of past explosions.

Supernova remnants also provide insight into ISM physics. The powerful shock waves produced in the supernova explosion propagate through the ISM, heating and ionizing the material they encounter. This interaction is the likely source of most galatic cosmic rays.

This thesis will concentrate on unique 3-dimensional infrared maps of supernova ejecta from the galactic supernova remnant Cassiopeia A (Cas A). A major point of emphasis will be the location of various elements with respect to one another. We

observe varying degrees of separation between elements using infrared and X-ray observations and these observations of separation to constrain supernova explosion models. We also address the geometry of Cas A on many different scales based on our 3D models. Finally, we briefly address issues such as the possibility of cosmic ray acceleration at Cas A's reverse shock.

This introduction will address important background information concerning supernova remnants. Massive stars, the progenitors to core collapse supernovae, are discussed, with special emphasis on the formation of their nucleosynthetic layers. The collapse and eventual explosion of these massive stars is then explored. Finally, we address the expansion of supernova ejecta and shock waves into the ISM.

1.1 Massive Stars

All stars, including the most massive stars, begin their lives fusing hydrogen into helium in the core of the star via either the proton-proton chain (for low mass stars) or the Carbon-Nitrogen-Oxygen (CNO) cycle (for high mass stars). This phase of a star's lifetime is defined as the "main sequence" and is, by far, the longest stage of a star's evolution. When a star exhausts its core hydrogen supply, it begins to fuse helium. If the star has enough mass, the core will continue to contract because the force of gravity is able to overcome the pressure in the core. If this continues to happen, the star gets hot enough to fuse C, Ne, O, and Si, eventually forming a core of Fe. Only stars above $\sim$8 solar masses will be able to fuse up to Fe. At this point the star no longer has any viable fuel sources since it takes net energy to fuse Fe. The star undergoes catastrophic gravitational collapse, triggering a supernova explosion. The details of the life cycle of these most massive stars and the supernova explosion itself are discussed in more depth in the sections below.

1.1.1 Models of Massive Stars

Note: The following sections are based largely on Woosley et al. (2002)

The life of massive stars is governed by a balance between the inward force of gravity and outward forces. The outward forces are a combination of radiation pressure, gas

pressure, and late in the star's life, electron degeneracy pressure. The equation of state of the star is relatively straightforward. The electrons are described as a perfect thermal gas with arbitrary degeneracy and relativity. Billikov et al. (1996) and Timmes & Swesty (2000) provide computer simulations which determines this equation of state for the electrons. The ions are approximated as an ideal gas, and the radiation pressure is described by blackbody equations. The interaction among ions and between ions and electrons is an important complication and cannot be neglected in the later stages of the star's evolution.

We need to know opacity as a function of temperature and density in order to understand the evolution of a massive star. There are two distinct opacities: that of the interior and the opacity of the cooler, low-density envelope. Most of the interior of the star is fully ionized and the opacity is mostly due to electron scattering. At higher temperatures, this opacity is decreased because of corrections to Compton scattering. At the highest energies, electron-position pairs also contribute to the opacity. At high densities, the opacity is modified by electron conduction, which may cause the opacity to become small when the gas becomes degenerate due to the filling of electron phase space. The atmospheres of stars and convective envelopes of post main sequence stars differs substantially from electron scattering. Most researchers use the tables of Rogers & Iglesias (1992) and Iglesias & Rogers (1996) to address this region.

Neutrino losses are a critical component of massive star evolution once they finish hydrogen burning. These neutrinos are mostly due to thermal processes, especially pair annihilation, although neutrino losses from electron capture become important very late in the stars evolution when it begins Si burning. The temperature sensitivity of the neutrino losses along with the need for higher temperatures leads to a rapid acceleration of stellar evolution during C, Ne, O, and Si burning. For example, the Si burning stage of a star may only last a day. Modern calculations use fitting formulas to represent these neutrino energy losses (Itoh et al. 1996).

Massive stars on the main sequence rotate rapidly. Typical equatorial rotation velocities are of order several hundred km s^{-1}, which is a significant fraction of the breakup velocity at the surface of the star. Specific angular momenta this large implies that centrifugal effects could play an important role in various stages of stellar evolution. This situation becomes even more complicated because a star can transport angular

momentum in convective regions due to circulation and other instabilities. The gradual expansion of the star slows the angular velocity of rotation due to the conservation of angular momentum. This decrease in velocity is communicated all the way to the core of the star, and angular momentum can be extracted from the core by a stellar wind. The actual velocity distribution of the star depends on the efficiency of coupling between differentially rotation regions by instabilities, magnetic torques, and the magnitude and geometry of mass loss.

The effects of rotation on the observed properties of H and He burning stars are well documented and studied, although the effect of angular momentum transfer in later stages of stellar evolution is relatively poorly understood. Deep mixing enhanced by rotation explains the observed surface enhancements of He, Na, and N and the surface depletion of B in massive stars (Heger & Langer 2000). Rotation also causes larger He cores as well as larger C-O cores. Altering the ratio of core mass to envelope substantially changes the late evolution of stars.

Massive stars have strong stellar winds while on the main sequence. These winds become even stronger once the star leaves the main sequence, and may result in a star losing much of their mass. In fact, Wolf-Rayet stars have had such dramatic mass loss that they have lost their entire hydrogen envelope and perhaps their helium envelope as well. The stellar winds of main sequence O and B stars are not a substantial source of uncertainty between models of massive stars because they are fairly well understood and main sequence mass loss rates are small compared to the mass loss rates in later phases of a star's evolution. However, we do not have reliable empirical or quantitative mass loss theories for the late stages of stellar evolution.

Constraints on the post-main-sequence mass loss rate come from the distribution of stars in the Hertzsprung-Russell (HR) diagram. The absence of red supergiants with $\log L/L_{\odot} > 5.7$ indicates that the most massive stars ($M \geq 50 M_{\odot}$) lose most of their hydrogen envelope before they undergo the supernova explosion. The observed location of unstable luminous blue variable stars gives a mass-loss rate for a given stellar model. Additionally, the substantial number of relatively faint ($\log L/L_{\odot} \sim 4.5$) Wolf-Rayet stars, which have a very narrow mass-luminosity relationship, indicates a mass of $\sim$5-8$M_{\odot}$. Along with a large number of Wolf-Rayet stars with exposed helium-burning products at the surface, this implies a very large mass loss rate in the Wolf-Rayet stage. All

solar metallicity stars initially more massive than $\sim 35 M_\odot$ are thought to end their lives as hydrogen free objects of roughly $5 M_\odot$ given current empirical mass-loss rates. This limits the mass of the iron core to $\leq 2 M_\odot$.

1.1.2 Nucleosynthesis in Massive Stars

Massive stars spend about 90% of their lifetimes turning hydrogen into helium on the main sequence. The energy released depends on the metallicity of the star, but is typically small ($\sim$4.2x10^{18} erg g^{-1} for solar metallicity stars). This is less than the energy deposited in low mass stars by the proton-proton chain because more energy is carried away by neutrinos, which are more energetic in the CNO cycle. When the star exhausts most of its core hydrogen supply it begins more advanced forms of fusion. The main nuclear reactions for each stage of nuclear burning will be discussed below, although there are often secondary reactions that may be important to the evolution of the star.

When the star leaves the main sequence, it begins He and N fusion. The main nuclear reactions are $3\alpha \rightarrow {}^{12}\mathrm{C}$ & ${}^{12}\mathrm{C}(\alpha,\gamma){}^{16}\mathrm{O}$. Before the 3α process begins, the star must first burn away most of the N, which is about 2% of the core when the star leaves the main sequence, by ${}^{14}\mathrm{N}(\alpha,\gamma){}^{18}\mathrm{F}(\beta^+\nu){}^{18}\mathrm{O}$. The principle products of He burning are ${}^{12}\mathrm{C}$ and ${}^{18}\mathrm{O}$.

Stellar evolution after central helium burning becomes qualitatively different. Once the temperature exceeds $\sim$5x10^8 K, neutrino losses from pair annihilation dominate the energy budget. Burning can now go on simultaneously in the core of the star and in multiple shells, making the structure and composition of the star very complicated. However, each burning stage occurs at unique temperatures and densities due to the extreme temperature sensitivity of the relevant nuclear reactions in each region.

Carbon fusion occurs soon after He fusion and produces excited states of ${}^{24}\mathrm{Mg}$, which then decay into ${}^{23}\mathrm{Mg}$, ${}^{20}\mathrm{Ne}$, and ${}^{23}\mathrm{Na}$. After C burning, the star is composed mostly of ${}^{16}\mathrm{O}$, ${}^{20}\mathrm{Ne}$, and ${}^{24}\mathrm{Mg}$. O has the weakest Coulomb barrier, but Ne fusion via ${}^{20}\mathrm{Ne}(\gamma,\alpha){}^{16}\mathrm{O}$ becomes feasible next due to photons from the high energy tail of the Planck distribution before the temperature necessary for O fusion is reached. The α particle released by the ${}^{20}\mathrm{Ne}$ adds back onto ${}^{16}\mathrm{O}$, creating more ${}^{20}\mathrm{Ne}$. But when this reaction reaches equilibrium, the α particle begins to add onto ${}^{20}\mathrm{Ne}$, producing

^{24}Mg. The net result is that one ^{16}O and one ^{24}Mg appear for each ^{20}Ne that is destroyed. This nucleosynthetic stage has a relatively small energy yield but is important for nucleosynthesis and alters the structure of pre-supernova stars.

Oxygen is the lightest remaining element and the next to burn. Oxygen fusion is favored over its photodisintegration. This oxygen fusion reaction produces excited nuclear states of ^{32}S that may decay by any of 4 channels:

$$^{16}O +^{16} O \rightarrow^{32} S^{*} \rightarrow^{31} P + p + 7.68MeV \tag{1.1}$$

$$^{16}O +^{16} O \rightarrow^{32} S^{*} \rightarrow^{28} Si + \alpha + 9.59MeV \tag{1.2}$$

$$^{16}O +^{16} O \rightarrow^{32} S^{*} \rightarrow^{31} S + n + 1.45MeV \tag{1.3}$$

$$^{16}O +^{16} O \rightarrow^{32} S^{*} \rightarrow^{30} P + d - 2.41MeV \tag{1.4}$$

The branching ratios for these channels are 56%, 34%, 5%, and 5% respectively at high temperatures.

Si burning mostly does not occur as a straight forward fusion reaction, unlike C and O burning. Si burns in a unique way where much of the ^{28}Si "melts" by photodisintegration into neutrons, protons, and α particles by:

$$^{24}Si(\gamma,\alpha)^{24}Mg(\gamma,\alpha)^{20}Ne(\gamma,\alpha)^{16}O(\gamma,\alpha)^{12}C(\gamma,2\alpha)\alpha \tag{1.5}$$

The α particles released by this photodisintegration add into a large quasiequilibrium group above ^{28}Si, gradually increasing its mean atomic weight. Eventually, most of the particles become concentrated in tightly bound species within the Fe group and Si is largely depleted, creating substantial amounts of ^{48,49}Ti, ^{51}V, ^{50,52,53}Cr, ^{55}Mn, ^{54,56,57}Fe, ^{32}S, ^{36}Ar, and ^{40}Ca.

The net result of this chain of nucleosynthetic reactions is that the star now has a layered or "onion-skin" structure: the core of the star consists of Fe, with Si and S immediately on top of that, followed by an O layer, then an Ne layer, a C layer, a He layer, and finally an H layer. A schematic of this structure is shown in Figure 1.1. As mentioned previously, the lighter layers can be diminished or completely removed due to mass loss from the progenitor star.

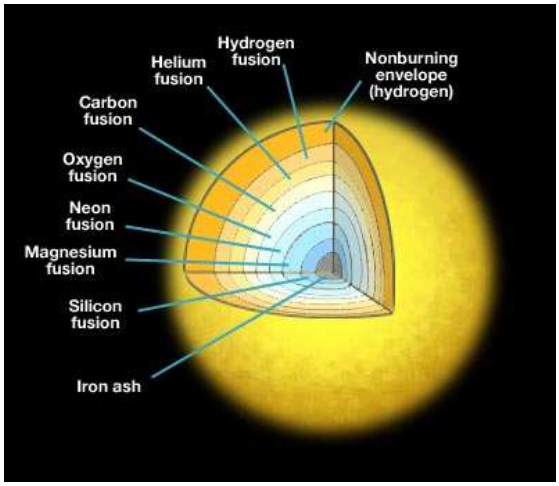

Figure 1.1: Schematic of a massive star immediately before it goes supernova. Note that this image is not to scale.

1.1.3 Modifications

The above picture can be modified by a number of factors, some of which we will discuss briefly here. For example, the effects of rotation on compositional mixing are known to be important during hydrogen burning. Models suggest that rotation is still important during more advanced burning stages, causing mixing of nucleosynthesis layers via shear instabilities. If rotation is indeed important, so are magnetic torques that exist between differentially rotating shells. Estimates of the importance of these torques vary widely in the literature.

Another important modification is the effect of mass loss. Massive stars lose a large fraction of their mass before they undergo a supernova explosion. In fact, the supernova mass of the star *decreases* with increasing zero age main sequence mass due to efficient mass loss. For example, at solar metallicity, the helium core of a 35 $M_{\odot}$ star at death reaches a maximum mass of only 12 $M_{\odot}$. Due to this mass loss, very massive stars are actually not any more difficult to detonate than $\sim$10 solar mass stars since they lose most of their initial mass before they go supernova.

The initial metallicity of the star has a large effect on how much mass the star loses, and therefore its radius immediately before the supernova explosion. For example, for zero metallicity stars, the progenitor mass of the star increases without bound with

increasing zero age main sequence mass since mass loss is minimal. This can have qualitative effects on the behavior of the supernova explosion (e.g. Joggerst et al. 2009).

1.2 Supernova Explosions

Note: The following sections are based largely on Woosley et al. (2002)

There are two major types of supernova explosions: Type Ia supernovae and core collapse supernovae. A Type Ia supernova is the detonation of a white dwarf as it exceeds the Chandrasekhar limit (approximately 1.44 $M_{\odot}$). This limit is reached when the outward pressure of the white dwarf can no longer match the inward gravitational pressure due to the mass of the star. However, this thesis will concentrate on core collapse supernovae: that is, the collapse and eventual explosion of a star with an initial mass of >8 $M_{\odot}$.

Core collapse supernovae are divided into different categories based on observation. Type II supernovae contain hydrogen in their spectrum, while Type I supernovae do not. Type Ib supernovae contain helium in their spectrum, while Type Ic supernovae do not. The progenitor stars of Type Ib and Ic supernovae are most likely Wolf-Rayet stars - that is, stars that have undergone so much mass loss that they have lost all of their hydrogen envelopes.

Type II supernovae are divided into categories primarily based on their post explosion luminosity as a function of time, or "light curve". Light curves provide a rich amount of information about the supernova explosion and are the primary method of testing theoretical predictions from models against observations. However, we do not further address light curves here since they are not a part of the observations discussed in this thesis.

The exact nature of core-collapse supernova explosions is a major area of research. There is substantial variation between models in the relevant physics behind the supernova explosion. Most groups use neutrino-driven shocks as the main mechanism causing the explosion, but some propose diffusive, magnetic buoyancy, or neutrino-bubble instabilities as the explosion mechanism (Janka et al. 2007), while yet other groups propose jet driven explosions, where the explosion is dominated by MHD driven jets formed

in rapidly rotating stars (e.g. Burrows et al. 2007). We will discuss the most widely accepted mechanism - neutrino driven shocks - in more depth in the next section.

1.2.1 Core Collapse

Beginning during C and O burning, the loss of energy due to neutrino losses causes a decrease in the central entropy of the star. Therefore, the core of the star nears and eventually exceeds the modified Chandrasekhar mass - the maximum mass that can be supported by electron degeneracy pressure against the gravitational pressure of the star. A degenerate iron core in excess of its Chandrasekhar mass will collapse. However, the core does not cross this transition instantaneously, but rather on a thermal time scale due to the fact that large amounts of neutrinos carry away the binding energy of the core.

This collapse is accelerated by two major instabilities. First, electrons capture onto iron-group nuclei as the density of the core rises. This removes electrons that were contributing to the electron degeneracy pressure. Additionally, the increase of temperature in the core of the star creates a region where nuclear statistical equilibrium favors an abundance of free α particles. This reduces the nuclear binding energy of the new composition, so the core does not gain enough thermal energy as it contracts to keep pace with gravity. Both these processes reduce the effective Chandrasekhar mass and accelerate the collapse.

1.2.2 Core Bounce

In the past, it was thought that the star would undergo a core "superelastic bounce", which would successfully explode the star. It is now known that this does not cause the explosion for models with realistically sized iron cores and realistic neutrino physics. However, the core bounce is still an important process and will be discussed in some depth in this section.

As the star collapses, the heavy nuclei persist until they touch and merge at just below nuclear density. The result is essentially one gigantic stellar mass nucleus. It was thought that the Fe core might disintegrate beyond α particles into individual nucleons at this point. Free protons and electrons would combine, dropping the density of the core

to well below nuclear, essentially causing the core of the star to bounce as it overshot nuclear density by a factor of at least several. In essence, the repulsive hard potential of the nucleus would act as a stiff spring storing up energy in the compressive phase, then rebounding as the compression ends. Part of the core, the "homologous core mass", stays in sonic communication with itself. Just outside of this, a shock wave forms as the rebounding core encounters matter that continues to fall inward. The result is a supersonic impact as the bouncing core encounters the infalling material. The infalling outer core could bounce back to the radius from which it fell (in a perfectly elastic collision) even if the inner core were stationary. This outward motion of the inner core gives rise to a "superelastic bounce".

However, two effects prohibit this from being the primary explosion mechanism. First, as the shock moves through the infalling material, much of its energy is lost as it heats and tears apart the infalling nuclei. The shock will lose roughly 10^{52} erg for each solar mass of infalling material. Secondly, neutrino emission from behind the shock causes a loss of energy. Neutrinos of all flavors scatter with electrons behind the shock. Unlike coherent scattering off of nuclei, electron scattering does not conserve neutrino energy. By reducing the neutrino energy, electron scattering makes it easy for neutrinos to escape and carry away their energy.

1.2.3 The Neutrino Driven Shock

Since the star cannot have detonated yet, we are left with a hot, dense, proto-neutron star accreting matter at its outer boundary about 10 ms after the core has bounced. A successful explosion requires a new energy source. This additional energy source is now thought to be neutrino energy deposition. Essentially, neutrinos are emitted from the dense nuclear material. The density of the medium is such that the neutrinos random walk outward, depositing much of their energy into the surrounding material. This revives the shock wave at a time of $\sim$0.1s after the initial core collapse.

Much recent progress has been made simulating this event in two and three dimensions. Multidimensional calculations are essential in order to properly address the convective flow responsible for boosting the neutrino luminosity of the proto-neutron star. This flow cools the region where neutrinos deposit their energy, increasing the efficiency of neutrino absorption (Fryer & Heger 2000).

Most recent two dimensional calculations have successfully exploded massive stars. However, the two-dimensional models have common problems when compared to observations. For example, such models tend to underpredict the expansion velocity of the explosion by a factor of $\sim$2, and tend to blow away too large a portion of the neutron star, leaving remnant masses that are too small. Many of these problems can be addressed with three dimensional models, however, such models obviously require greater computational times.

1.2.4 Forward Shock Propagation

There are instabilities that will affect the outward propagation of a shock, even for initially spherically symmetric explosions. The passage of a shock leaves regions of inverted gravitational and density gradients, leading to Rayleigh-Taylor instabilities. The importance of this instability depends on the star's mass and density structure. Stars with more massive extended envelopes that have not lost a lot of mass (e.g. red supergiants) experience the most Rayleigh-Taylor mixing.

The criterion for mixing of nucleosynthetic layers is that the forward shock must slow down in a region where density is declining. The Sedov solution shows that the shock decelerates when passing through a region where ρr^3 increases. Additionally, mixing can be introduced if the explosion inputs its energy in an asymmetric way, so the seeds for mixing may be present prior to the passage of the forward shock.

1.3 Supernova Remnants

After the initial supernova explosion, the remnant of the explosion undergoes three distinct phases of evolution. Initially, the remnant is in the free expansion phase. The density of the ejecta matter is much higher than the density of the circumstellar environment, so the expansion of the remnant is unaffected by its surroundings. This phase ends approximately when the matter swept up by the expanding envelope is of the same order as the mass of the envelope. The remnant then enters a phase of adiabatic expansion. In this phase the only relevant energy losses are due to the adiabatic expansion of the remnant, since the shocked gas is too hot to radiate energy efficiently. This phase ends when the temperature drops below 10^6K, at which point radiative losses become

large. Finally, the remnant enters an isothermal phase, during which substantial energy is lost due to radiation. This phase ends when the envelope disperses into the ISM, which occurs when the velocity drops to about 10 km s^{-1}.

Each of the phases will be addressed in more detail below after a brief discussion concerning shocks.

1.3.1 The Rankine-Hugoniot Jump Conditions

Note: the following sections are based heavily on Lequeux (2005)

Shocks with no magnetic fields experience a discontinuity (or jump) in the physical parameters of the gas at the shock front. Using the assumption that the magnetic field is negligible, and that there is no heat flux or radiative losses, the conservation of matter, momentum, and energy per unit mass equations can be written down in a reasonably simple form. We do not reproduce the equations here, but they can be found in Chapter 11.2.1 of Lequeux (2005).

By combining these conservation equations, we can write down the Rankine-Hugoniot jump conditions, which are relationships between the pre- and post-shock density, pressure, and velocities. Note that in the following sections, the subscript "1" indicates a preshock quantity, while the subscript "2" indicates a postshock quantity.

$$\frac{\rho_2}{\rho_1} = 4 \tag{1.6}$$

$$v_1 = (\frac{4P_2}{3\rho_1})^{1/2} \tag{1.7}$$

$$\frac{v_2}{v_1} = 1/4 \tag{1.8}$$

$$v_2 = (\frac{kT_2}{3\mu_2 m_H})^{1/2} \tag{1.9}$$

$$\frac{T_2}{T1} = \frac{\mu_2 P_2}{4\mu_1 P_1} \tag{1.10}$$

One of the most significant results is that material encountering a strong shock is compressed by a factor of 4 regardless of the initial speed of the shock and the temperature of the material if no energy is lost. Any energy losses (perhaps due to cosmic ray production) can cause compressions well beyond the factor of 4 seen here.

1.3.2 Free Expansion Phase

The initial velocity of the ejecta is very large - typically of order 10,000 km s^{-1}. The shock that forms as this material propagates outward is a MHD shock, rather than a classical shock that forms when the ejected matter has swept out a radius equal to the mean free path of the ejected particles in the circumstellar medium. The mean free path of a proton in a gas with density 1 g cm^{-3} is roughly 400 pc, which is much larger than the size of most supernova remnants. The presence of a magnetic field of order a few microgauss means that protons (with gyroradius $<10^{11}$ cm) cannot escape from the envelope, forming a shock. The existence of the magnetic field is confirmed by observations of synchrotron radiation, which indicates that magnetic fields (probably enhanced by Rayleigh-Taylor instabilities) are accelerating charged particles to relativistic velocities.

This phase of evolution ends when the swept up mass is of the same order as the initial mass of the ejecta:

$$\frac{4}{3}\pi r_s^3 \rho_1 \sim M_{ejecta} \tag{1.11}$$

where r_s is the radius of the shock. This radius will be reached after about 75 years for reasonable parameters. At that point, the shock "sees" the surrounding material and its velocity decreases due to conservation of momentum.

1.3.3 The Adiabatic or Sedov-Taylor Phase

The adiabatic or Sedov-Taylor phase of evolution is characterized by a strong, non-radiative shock. Therefore, there is a conservation of energy that is liberated by the initial explosion. Sedov (1959) showed that there is a self-similar solution describing the evolution of the remnant in this phase. This means that the structure of the supernova remnant stays constant as a function of time. In this solution, part of the energy is thermal (roughly 75%), with the rest being kinetic. The ratio of the pressure immediately behind the shock to the average pressure of the heated gas inside of the shock is constant. The gas is assumed to be a perfect gas, which implies that the pressure is equal to 2/3 of its specific internal energy u. Therefore:

$$P_2 = K_2 \frac{2}{3} \frac{3K_1 E}{4\pi r_s^3} = \frac{K_c E}{2\pi r_s^3} \tag{1.12}$$

with K_c=K_1K_2=1.53. The shock velocity is provided in §4.1 and is:

$$v_{shock} = (\frac{4P_2}{3\rho_1})^{1/2} = \frac{2}{3\pi}\frac{K_c E}{\rho_1 r_s^3}^{1/2} \tag{1.13}$$

Integrating this equation with respect to t gives:

$$r_s = (\frac{5}{2})^{2/5}(\frac{2K_c E}{3\pi\rho_1})^{1/5} t^{2/5} \tag{1.14}$$

The velocity of expansion depends on $t^{2/5}$, rather than just t as it did in the free expansion phase. The temperature behind the shock is:

$$T_2 = \frac{3\mu m_H v_{shock}^2}{16k} \tag{1.15}$$

It is interesting to note that the temperature behind the shock increases toward the center because the gas there was shocked at a time when the velocity and post shock temperature of the gas were larger and the cooling times are very long.

Another important effect of the transition between the free expansion and adiabatic phases is the separation of a reverse shock. The pressure behind the forward shock, which comes from the interaction between supernova ejecta and the circumstellar material, is high and propagates downstream in the ejected matter. This matter then cools radiatively, and the sound velocity decreases while the pressure perturbation turns supersonic. This forms a reverse shock which propagates toward the center of the remnant. Most visible emission lines in very young supernova remnants, including Cas A, are produced by this shock. After the passage of the reverse shock, the supernova remnant is fully into the adiabatic stage of evolution.

1.3.4 The Isothermal or Snowplow Phase

Electrons begin to recombine with the nuclei of abundant elements like C, N, O, and Si when the postshock temperature drops to $<10^6$K. The ions are then collisionally excited, causing an increase in the radiative energy loss in the remnant by a factor of >100. Since the cooling of the shock is now efficient, the propagation is no longer maintained by thermal energy, but by the momentum of the gas. The conditions necessary for the remnant to enter this phase usually occur when at a shock radius of about 15 pc, which implies an expansion velocity of ∼90 km s^{-1} and an age of ∼40,000 yrs.

The product of the total mass and mean velocity of the shell is constant due to the conservation of momentum. Most of the mass of the shell is from the circumstellar environment rather than the supernova explosion itself. Therefore:

$$\frac{4}{3}\pi r_s^3 \rho_1 v_s = constant \tag{1.16}$$

Integrating this equation:

$$r_s = r_o(\frac{8}{5}\frac{t}{t_o} - \frac{3}{5})^{1/4} \tag{1.17}$$

where r_o and t_o are the radius and age of the remnant at the beginning of the Isothermal phase. This phase ends when the supernova remnant vanishes. This occurs when the shock velocity is about the same as the dispersion velocity of the ISM, which is about 10 km s^{-1}. The kinetic energy of the remnant is transferred to the ISM. This occurs about 1 Myr after the initial supernova explosion.

1.3.5 Inhomogeneities

The above discussion mostly makes the assumption that the remnant is expanding into a homogeneous medium. The expansion velocity of the remnant can vary in some stages as a function of the density of the surrounding medium (e.g. Eqn. 1.13), so inhomogeneities in the surrounding medium can affect the overall geometry of the remnant.

Furthermore, a shock compresses any inhomogeneous clouds or filaments that it encounters. An internal shock within the cloud or filament is created due to pressure increases on the surface. Clouds and filaments are usually dense enough for energy to be radiated away efficiently, lowering the temperature. The pressure is higher on the side directed toward the center of the remnant, so the cloud is accelerated and flattened. These internal shocks are isothermal and emit lines in the X-ray, infrared, and visible.

1.3.6 Cosmic Ray Acceleration

Cosmic rays are charged subatomic particles with energies between $\sim 10^9$ - 10^{21} eV. These particles are primarily responsible for the formation for some elements like Li, Be, and B through cosmic ray nucleosynthesis. They are also responsible for a large part

of the background radiation on Earth, and will be an even stronger source of radiation beyond Earth's magnetic field.

There are multiple sources for cosmic ray production. The Sun produces many lower energy cosmic rays, while extra galactic sources are the likely source for the highest energy cosmic rays. Supernova remnants are the most likely source for moderate energy cosmic rays. The likely mechanism for the acceleration of particles is Fermi Acceleration.

In the Fermi Mechanism, charged particles are accelerated as they are repeatedly reflected by a magnetic mirror. The key for acceleration is that most of the reflections must impart energy to the particle rather than take it away. A shock propagating in a uniform medium is very inefficient at accelerating particles using this mechanism. However, irregularities in the associated magnetic field diffuse the particles on either side of the shock and are much more efficient. See secion 12.4.4 of Lequeux (2005) for a more in depth discussion of cosmic ray acceleration.

A source of current research in this process is the so called "injection problem". Only particles with energies that exceed the thermal energy by at least a factor of a few can cross a shock and begin Fermi acceleration. It is not clear what mechanism causes particles to have energies high enough to cross the shock.

1.3.7 Radiative Emission - Line Radiation

Note: This section is based largely on Osterbrock (1989)

The material which passes through a shock becomes heated and ionized. Initially neutral atoms will become collisionally ionized if the temperature of the postshock medium is high enough. Eventually, the material cools down and the temperature becomes low enough for recombination. At this point, we observe emission lines.

We will use the emission coefficient, j, to describe how much radiation is emitted via line radiation from some volume. Consider an atom with lower level i and upper level k, and let n_i and n_j be the density of particles in the upper and lower energy levels. The emission coefficient is then:

$$\int j_v dv = \frac{h v_{ij} n_k A_{ji}}{4\pi} \tag{1.18}$$

where A_{ji} is the Einstein A coefficient for spontaneous downward transitions. Assuming that the system is in local thermodynamic equilibrium and that most of the atoms are ionized once more than the emitting particles, we can use a combination of the Boltzmann and Saha equations to relate n_j to the number densities of electrons and ions. The emission coefficient then becomes

$$\int j_v dv = hva_{ji} n_e n_p \tag{1.19}$$

where a_{ji} is the effective recombination coefficient. The line emission to therefore proportional to n^2 if the number of ions is equal to the number of electrons, which is true for hydrogen.

The typical timescale for the material behind the shock to become radiative is very long because of the high speed of the shock and the low interstellar densities. However, if the shock propagates into a density enhancement, the shock speed decreases and the timescale for the shocked material to cool is much shorter. This is why we only largely observe dense knots of emitting material in Cas A in the X-ray and optical.

1.4 The Chapters

Chapter 2 of this thesis concentrates on 3-dimensional maps of ejecta interior to Cas A's reverse shock. This material has not yet been modified by the circumstellar environment, and is therefore ideal for exploring the supernova explosion itself. We focus on various asymmetries in the geometry of the ejecta and the separation between nucleosynthetic layers. We use our observations of the relative locations of various nucleosynthetic layers to constrain supernova explosion models.

Chapter 3 focuses on a similar data set to the one used in Chapter 2, but this data set is from regions on Cas A's reverse shock, where we see pre- and post-shock ejecta. We concentrate on the local and overall geometry of the ejecta, large scale asymmetries, and the separation between nucleosynthetic layers in some directions. We address issues such as corrugation in the shocked material, the velocity profile of the ejecta, and dim ejecta which has yet to be shocked.

Chapter 4 contains an analysis of X-ray observations from the Chandra X-ray Observatory. We identify regions that show evidence of separation between the Mg and Fe

nucleosynthetic layers, and find another large region that shows separation between the Si and Mg layers. We also find the most recently shocked X-ray ejecta and briefly address the possibility of using them to contrain cosmic ray acceleration at the remnant's reverse shock.

Chapter 5 is a summary of the results. It also contains a discussion of the possibilities for future work, especially using data from newer observatories like the Herschel Space Telescope and the Stratospheric Observatory for Infrared Astronomy (SOFIA).

Chapter 2

The Three-Dimensional Structure of Interior Ejecta

Note: A slightly modified version of this article appears in the Astrophysical Journal: Isensee, K., Rudnick, L., DeLaney, T.A., Smith, J. D., Rho, J., Reach, W. T., Kozasa, T., & Gomez, H. 2010, ApJ, 725, 2059

We used the *Spitzer Space Telescope*'s Infrared Spectrograph to create a high resolution spectral map of the central region of the Cassiopeia A supernova remnant, allowing us to make a Doppler reconstruction of its 3D structure. The ejecta responsible for this emission have not yet encountered the remnant's reverse shock or the circumstellar medium, making it an ideal laboratory for exploring the dynamics of the supernova explosion itself. We observe that the O, Si, and S ejecta can form both sheet-like structures as well as filaments. Si and O, which come from different nucleosynthetic layers of the star, are observed to be coincident in velocity space in some regions, and separated by 500 km s^{-1} or more in others. Ejecta traveling toward us are, on average, $\sim$900 km s^{-1} slower than the material traveling away from us. We compare our observations to recent supernova explosion models and find that no single model can simultaneously reproduce all the observed features. However, models of different supernova explosions can collectively produce the observed geometries and structures of the interior emission.

We use the results from the models to address the conditions during the supernova explosion, concentrating on asymmetries in the shock structure. We also predict that the back surface of Cassiopeia A will begin brightening in ∼30 years, and the front surface in ∼100 years.

2.1 Introduction

Cassiopeia A (Cas A) is the second youngest known supernova remnant (SNR) in our galaxy, with only the recently discovered G1.9+0.3 being younger (Reynolds et al. 2008). Extensive observations in the radio, infrared, optical, and X-ray give an estimated explosion date of around 1680 AD (Thorstensen et al 2001; Fesen et al. 2006). Emission at most wavelengths, including the infrared, is dominated by a ∼120″ radius "Bright Ring", which corresponds to ∼2 pc at Cas A's estimated distance of 3.4 kpc (Reed et al. 1995). This 30″ thick Bright Ring is formed when ejecta encounter Cas A's reverse shock and are heated and ionized. It consists of undiluted ejecta rich in O, Si, S, Ne, Ar, Ca, and Fe (Chevalier & Kirshner 1978; Douvian et al. 1999, Hughes et al. 2000; Willingale et al. 2003; Hwang & Laming 2003; Laming & Hwang 2003; Morse et al. 2004). Optical, radio, and X-ray observations have revealed the presence of a jet and counter jet in Cas A. These jets consist of a bipolar outflow nearly in the plane of the sky (Fesen & Gunderson 1996). Also visible in the X-ray is a central compact object, presumed to be the neutron star from the progenitor supernova explosion (Tananbaum 1999).

Cas A also contains central emission that is not the result of the reverse shock interaction. This material was first discovered via free-free absorption at low radio frequencies (Kassim et al. 1995) and has since been detected in the infrared (Rho et al. 2009; Smith et al. 2009). This material was demonstrated to be in substantially different physical conditions than recently shocked material on the Bright Ring through a combination of Doppler analysis and line ratio measurements (Smith et al. 2009). The central material is likely photoionized by ultraviolet and X-ray emission from the Bright Ring (Hamilton & Sarazin 1984; Hamilton & Fesen 1998; Smith et al. 2009), and is relatively poorly studied and understood since it is only visible at select wavelengths.

These ejecta are usually referred to as "unshocked ejecta" since they have yet to encounter the remnant's reverse shock. That is not an entirely accurate label since Cas A's forward shock, as well as shocks during the supernova explosion itself, have heated this material in the past. The central emission is ideal for exploring the conditions of the supernova explosion because ejecta interior to the Bright Ring have not yet interacted with the remnant's reverse shock or circumstellar material, leaving them in a relatively pristine state.

Recent studies of optical spectra of the explosion near peak light obtained with light echos have led to the observation of weak hydrogen lines, indicating a supernova Type IIb origin for Cas A (Krause et al. 2008). In this scenario, Cas A's progenitor was the explosion of a red supergiant that had lost most, but not all, of its hydrogen envelope. The estimated oxygen mass of 1-3$M_\odot$ points to a main sequence mass of about 15-25$M_\odot$ (Young et al. 2006; Vink et al. 1996). X-ray studies indicate a total ejecta mass of less than 4$M_\odot$. If one adds to this the mass of the central compact object, presumed to be a neutron star (Chakrabarty et al. 2001), Cas A's progenitor had a total mass of about 6$M_\odot$ immediately prior to the supernova explosion.

Spectropolarimetric observations of supernovae have shown that all observed core collapse supernovae contain intrinsic polarization, indicating that there is a departure from spherical symmetry (Wheeler et al. 2005). An axis-symmetric geometry, perhaps induced by jets, can be used to explain some features in some core collapse supernovae, but significant departures from axial symmetry are needed to explain most observations (Wang & Wheeler 2008).

2.1.1 Previous 3D Studies

Global mappings of Cas A have been carried out in the optical, infrared, and X-ray. In the optical, 3D Doppler reconstructions of the ejecta geometry primarily used S and O emission lines (Lawrence et al. 1995; Reed et al. 1995) and showed that ejecta on the Bright Ring lie on a spherical shell but do not uniformly fill that shell; most of the ejecta lie nearly in the plane of the sky. They also observe that the center of expansion of the ejecta is offset from the geometrical center of the spherical shell by ∼0.36pc, indicating that the ejecta are not travelling at the same velocity in all directions with respect to the central compact object. This is consistent with previous results which

indicated a non-spherical expansion for the ejecta (e.g. Braun 1987; Willingale et al. 2002). The 3D reconstructions give us a selective "snapshot" of ejecta in the sense that only material that has recently encountered the remnant's reverse shock will emit strongly in the infrared and especially in the optical and X-ray. Emission from material that has yet to reach the remnant's reverse shock is not visible in the X-ray and optical. Currently, ejecta must be travelling at $\sim$5000 km s^{-1} in order to be encountering the remnant's reverse shock (Patnaude & Fesen 2007).

DeLaney et al. (2010) utilized a spectral mapping of Cas A from the *Spitzer Space Telescope* and the *Chandra X-ray Observatory* to make a 3D infrared and X-ray map of the remnant. They found a similar distribution of ejecta to that seen in the optical and consistent with a model in which the remnant's reverse shock is a nearly spherical structure $\sim$1.5 pc in radius that is offset from the geometrical center of the remnant both in projection and along the line of sight.

X-ray Si/S and O emission is observed to be co-located in most regions (e.g. Ennis et al. 2006) in both the X-ray and infrared. This indicates that the two layers have very similar velocities (less than 80 km s^{-1} difference) so that they arrive at the remnant's reverse shock at approximately the same time. However, strong evidence of elemental differentiation is found in some directions in the X-ray (e.g. Hughes et al. 2000), the optical (Fesen et al. 2006), and the IR (Smith et al. 2009; Ennis et al. 2006), which was likely caused by the different layers of the star being ejected at different velocities in those directions, thus encountering the remnant's reverse shock at different times. In some regions, only material associated with the Si/S layer is currently encountering the remnant's reverse shock, indicating that that layer has the "correct" velocity of $\sim$5000 km s^{-1}.

In other directions, Fe is currently seen at the remnant's reverse shock, indicating that the Si/S and O layers may have a large enough velocity to have already passed through the remnant's reverse shock and ionized up to states which are not detectable in the X-ray. Ennis et al. (2006) found regions where only Ne and O are encountering the reverse shock, indicating that the Si/S layer is travelling slowly enough that it has yet to reach the remnant's reverse shock. Differentiation was also observed by Smith et al. (2009) in the form of variations in the Ar vs. O + Ne abundances. The velocity separation between the various layers needs to be several hundreds of km s^{-1} in order

for the layers to reach the reverse shock years apart and produce the differentiation observed.

We emphasize that we can only observe mixing or separation in *velocity space*. Simulations predict that the relevant nucleosynthetic layers will be $< 10^{11}$ cm thick prior to the explosion (e.g. Joggerst et al. 2009). If two such layers are ejected with different velocities, their physical separation will grow with time, and we can detect them individually as they sequentially encounter the reverse shock. However, if the layers were ejected at the same velocity, they would still form adjacent 10^{11} cm thick shells as they encountered the reverse shock, and we could not separate them. In addition to the overall shell velocity, there is likely small-scale turbulence which would stretch and broaden clumps and filaments to their observed widths of $\leq 1''$ ($\sim 10^{16}$ cm). If this turbulence also mixes the shells, but does not separate them in velocity space, then the layers will encounter the reverse shock at the same time/place. Thus, if we see separate layers, we know there was a significant velocity difference between them. If we do not see separate layers, then either their velocities were the same, or they were physically mixed; we cannot separate those two situations.

2.1.2 Interior Emission

Previous IR observations also contain information about ejecta that have yet to encounter the remnant's reverse shock (e.g. Smith et al. 2009). These are visible because some IR ionic lines, like the 34.81μm [Si II] line, will be photoionized by X-Rays and UV light from the Bright Ring even if they have yet to reach the remnant's reverse shock. They can therefore be visible interior to the remnant's reverse shock or far beyond it if the ejecta passed through it decades ago (Chevalier & Oishi 2003).

In the case of Cas A, these interior ejecta give it a filled center appearance (Smith et al. 2009), as opposed to being dominated by the Bright Ring. DeLaney et al. (2010) show that this interior emission is organized into a "Thick Disk" structure, tilted at $\sim$70 degrees from the line of sight. The material is moving perpendicular to that plane at $\sim$2500 km s^{-1}, indicating that it is only about half-way to the remnant's reverse shock. Figure 2.1 illustrates the relationship between the remnant's reverse shock, the Bright Ring, and the interior ejecta.

We present an analysis of a new, higher resolution Spitzer mapping of the ejecta

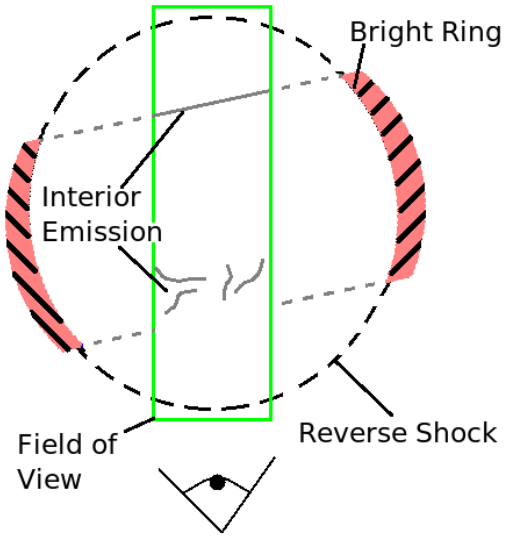

Figure 2.1: 2D projection cartoon of the shock and ejecta structure showing the connection between the observations presented here and the model of (DeLaney et al. 20010) as viewed from the top. The remnant's reverse shock is a nearly spherical structure, while the ejecta are flattened nearly perpendicular to the plane of the sky. Only part of the reverse shock is observable, while sections of the remnant's reverse shock that are not currently encountering ejecta are not currently observable (dashed black). Ejecta that are currently encountering the remnant's reverse shock will be visible as mixed X-ray, IR, and optical emission (hashed and gray), while ejecta interior to the remnant's reverse shock will only be visible in select IR lines (gray). The approximate field of view of the current observations is indicated by the box, within which are the different structures as discussed in §2.4.

towards the center of Cas A. In §2.2 we present the Spitzer observations. In §2.3 we discuss the methods used in our analysis and we describe those results in §2.4. §2.5 contains a discussion of the physical implications.

2.2 Spitzer Observations

The Spitzer Infrared Spectrograph (IRS) was used on August 30, 2007 to spectrally map select relatively bright regions of Cas A. This paper will address only the central map whose location is shown in Figure 2.2; a followup paper will address the other regions. High-resolution spectra (R$\sim$600 for all wavelengths) were taken between 10-20μm and 20-35μm using the Short High (SH) and Long High (LH) modules respectively. The

full-width-half-max of the lines at this spectral resolution is about 0.06μm at 35μm and about 0.02μm at 12μm. This represents an improvement in spectral resolution of a factor of $\sim$6 over the earlier observations of DeLaney et al. (2010). The LH data were taken in a single large map with 3x15 pointings using a 61 second exposure at each position. The SH data were taken with 6x15 pointings using a 31 second exposure at each position. The mapped area ranged from 54″x40″ (LH) to 48″x36″ (SH) at a spatial resolution of $\sim$1.25″ and $\sim$2.5″ respectively.

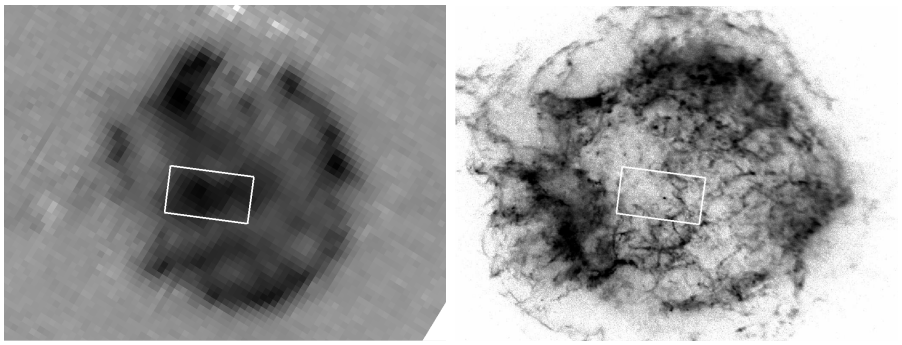

Figure 2.2: 34.81μm [Si II] *Spitzer* IRS map and X-ray Si *Chandra* map of Cas A. The region of high resolution data discussed in this text is indicated.

The spectra were reconstructed at each slit position, the background was subtracted, and 3D cubes were created using the S17 version of the IRS pipeline and the CUBISM software package (Smith et al. 2007). The statistical uncertainties for each line of sight were calculated using standard error propagation of the BCD level errors from the standard IRS pipeline.

In general, our uncertainties were limited by the undersampling of the IRS modules, which is worst at the short-wavelength end. This is a systematic error that exists in the wavelength calibration data themselves. It limits our obtainable absolute wavelength accuracy to roughly 1/2 of a spectral bin, or about 100 km s^{-1}, although the relative wavelengths for a given line can be measured with higher accuracy.

2.3 Data Analysis

Cas A's infrared spectrum is dominated by bright ionic emission lines as shown in Figure 2.3. The LH observation contains lines from [O IV] and/or [Fe II] at 25.9μm, [S III]

at 33.48μm, and [Si II] at 34.81μm. The SH observation has a [S IV] line at 10.5μm, [Ne II] at 12.8μm, and another [S III] line at 18.7μm. The lines observed in the LH module typically have peak fluxes from 200-4000 MJy sr^{-1}, with an rms noise of $\sim$15. Lines in the SH module have peak fluxes from 12-250 MJy sr^{-1} and a typical rms noise of $\sim$8. We also tentatively identify the 17.94μm [Fe II] line with 2σ significance when we spatially bin all pixels over the entire central region.

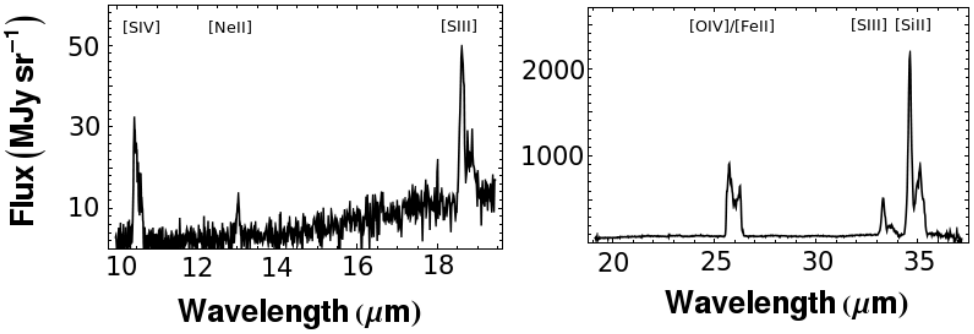

Figure 2.3: Typical spectra from the SH and LH *Spitzer* IRS modules of central emission of Cas A.

Observed emission near 25.9μm could be from either the 25.89μm [O IV] line or the 25.98μm [Fe II] line. In order to differentiate betwen the two lines, we compared the Doppler structure of the 25.9μm line to that of the [Si II] and 33.48μm [S III] lines for several lines of sight. In Figure 2.4 we display the results for one line of sight, showing the velocity structure of the [Si II] line at 34.81μm, the [S III] line at 33.48μm, as well as the 25.9μm line under the assumption that it is either composed entirely of either [O IV] or [Fe II] emission. We obtain an excellent match under the assumption of [O IV], but a poor match under the assumption of [Fe II]. The mismatch in Doppler structure under the assumption of [Fe II] cannot be due to [Fe II] simply having different velocities than [Si II] and [S III] since the [Fe II] ejecta would have to be moving more rapidly than [Si II]/[S III] on the front side of the remnant and more slowly on the back side in order to produce the observed spectrum. Thus, it is clear that the velocity structure is consistent with the line being composed entirely of [O IV]. We find no lines of sight that are consistent with having a substantial contribution from Fe. We assume for the remainder of this paper that the 25.9μm line is entirely due to [O IV] emission.

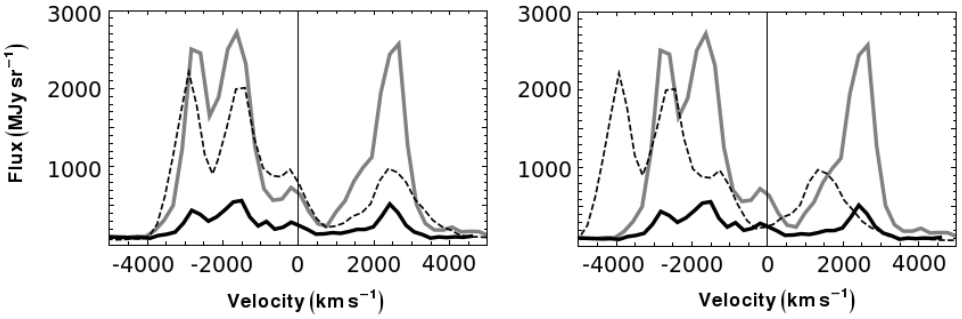

Figure 2.4: Velocity plot for the [Si II] line (gray) and the 33.48μm [S III] line (black) overplotted with the 25.9μm line (dashed) shifted under the assumption that it is either all [O IV] (left) or [Fe II] (right). The peaks match very well for the assumption that the 25.9μm line is all O, but match very poorly under the assumption that it is composed of Fe.

Th above analysis is based on the assumption of 25.8913μm for the rest wavelength of the [O IV] line (Feuchtgruber et al. 1997). This differs from the earlier value of 25.913μm (Froese Fischer 1983). Feuchtgruber et al. (1997) note that their results substantially improve upon the accuracy of previous values which were primarily based on energy level differences reconstructed from UV and optical spectroscopy.

Although [Si II] and [O IV] match up well along single lines of sight, the relative strength of [Si II] and [O IV] varies considerably from place to place. Therefore, the total line shapes from all interior emission are considerably different for the two ions as shown in Figure 2.5.

2.3.1 Doppler Deconvolution

After background subtraction, we performed a Doppler deconvolution of the spectral lines from each ion separately using a spectral CLEAN algorithm (Ding et al. 1999) for each line of sight. SH data cubes were binned 2 by 2 pixels (approximately 2.5″ by 2.5″) to increase the signal to noise ratio. A careful deconvolution is preferable to simpler techniques like measuring the peak wavelength of emission lines because the spectral CLEAN algorithm is able to separate partially blended components. An example of a CLEANed spectrum is shown in Figure 2.6. Note that flux in neighboring spectral bins was assumed to be from the same Doppler component. In this case we combined the bins and determined the peak wavelength of the Doppler component by taking a

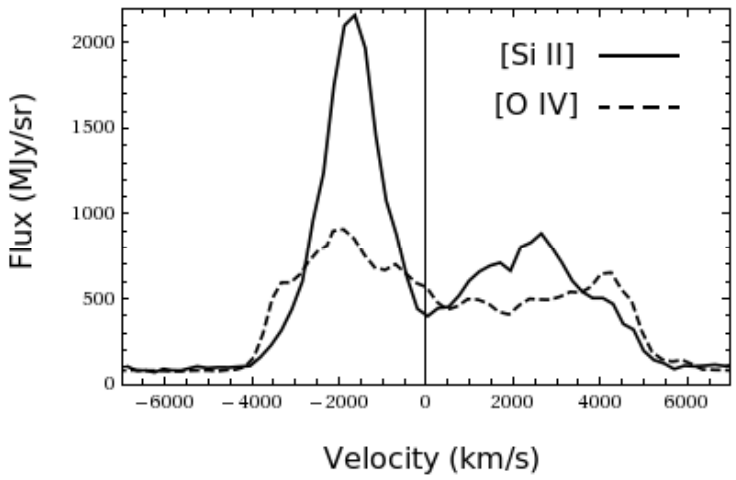

Figure 2.5: Doppler structure of [O IV] and [Si II] lines integrated over the entire central region. The average velocity of material on the back of the remnant is ∼900 km s^{-1} greater than that of material on the front.

weighted average of the wavelengths of the combined bins.

The spectral CLEAN was applied to each spatial pixel that had a signal greater than 3 times the off-line rms. We note that at our spatial resolution (∼2.5″), we may be binning over many individual knots. At the remnant's reverse shock ejecta knots which have typical sizes as small as 0.2″-0.4″ are observed (Fesen et al. 2001). We do not know the spatial size of any clumping in the interior ejecta.

Uncertainties in Doppler velocity for a given Doppler component were determined by applying the spectral CLEAN to synthetic line data with a realistic range of signal to noise ratios, and using actual line free data for the noise model. From these simulations, we determined the rms error in velocity as a function of line strength and location of the line peak within a spectral bin. In all cases, the uncertainty in velocity for a single, isolated Doppler component was determined to be less than 25 km s^{-1}. This means that our uncertainties in the absolute velocities are limited by the systematic errors in the calibration of about 100 km s^{-1} rather than random uncertainties, while the relative velocities for any given line are less than 25 km s^{-1}. We could not detect two separate components that were within 65 km s^{-1} of one another in synthetic data.

We assume that the ejecta have been freely expanding at a constant velocity in

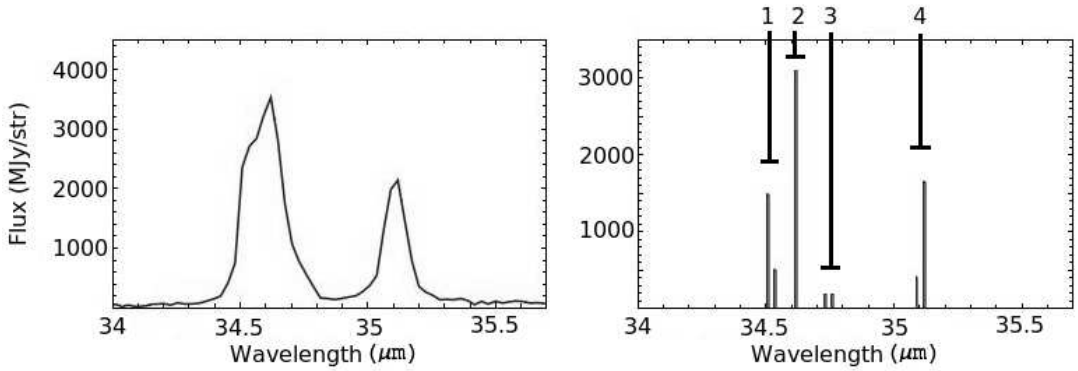

Figure 2.6: Spectral CLEAN algorithm applied to a sample spectrum (left). CLEAN components from adjacent bins were combined (as seen in the cases of the neighboring bins at ∼34.5μm, 34.75μm, and 35.1μm in the right figure) and very weak components with fluxes less than 100 MJy sr^{-1} were removed, so only 4 distinct Doppler components were extracted from this line of sight. These components are shown and numbered (right). The separation between these components is about 850, 1300, and 3000 km s^{-1} from left to right, comfortably larger than our ∼100 km s^{-1} uncertainty.

order to determine their spatial coordinate perpendicular to the plane of the sky. This assumption is still valid despite the fact that the ejecta were likely decelerated by shocks during the supernova explosion itself - any deceleration happened at the time of the explosion (that is, near t=0, z=0 where z is the spatial coordinate perpendicular to the plane of the sky) so the behavior is virtually identical to free expansion at a reduced velocity. We transformed our Doppler velocities to a z axis spatial coordinate in Figure 2.7, but leave the z axis in velocity units in Figures 2.8 - 2.13. The flux from each component is displayed by varying the transparency; the brightest voxel for a given ionic line is 80% opaque, while the opacity of all other voxels is linearly scaled downwards as a function of the intensity of the Doppler component. For a discussion of the uncertainties due to the above assumptions, see DeLaney et al. (2010).

We note that our results are consistent with the lower spectral resolution results of DeLaney et al. (2010). When plotted on the same axes, the ejecta detected in both observations trace out similar structures as shown in Figure 2.7, although our superior spectral resolution (R∼600 vs R∼100) allows us to detect many details that were previously not observed.

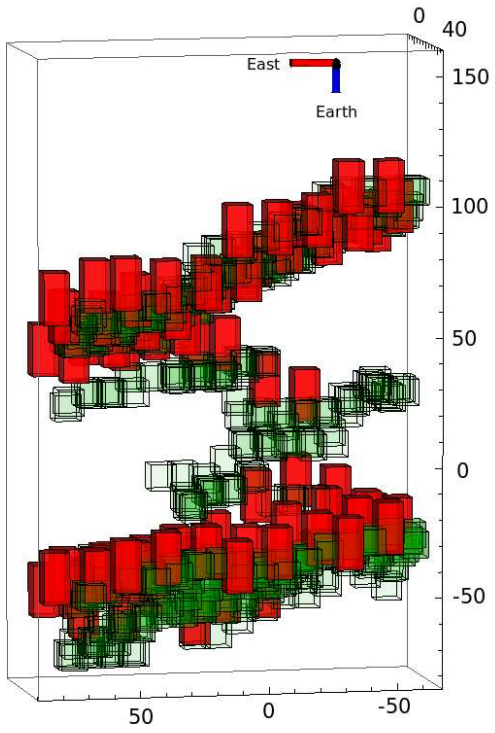

Figure 2.7: Comparison of our high resolution [Si II] line (green) to DeLaney et al. (2010) (red), which is at lower spectral resolution. The units are arcseconds from the center of the Bright Ring.

2.4 Results

2.4.1 3D Map

We plot the Doppler components from the 3 strongest lines in Figures 2.8 - 2.10 - the 25.89μm [O IV] line, the 34.81μm [Si II] line, and the 33.48μm [S III] line. The other lines are either very weak (in the case of Ne and Fe) or trace out identical structures as other lines from the same element (in the case of the other S lines). The velocity axis has been stretched by a factor of 1.8 in order to highlight features in velocity space. Due to the low density of the interior ejecta ($\leq$100 e^- cm^{-3} - Smith et al. 2009) we expect line of sight absorption to be minimal. However, we note that we are likely only observing the very densest ejecta since a small decrease in density will result in a substantial drop

in emissivity. Therefore, it is likely that there is a large amount of undetected interior ejecta present that is at too low a surface brightness to be detected.

The most striking aspect of this emission is that the center of the remnant is not uniformly filled, but consists of distinct structures. We label the material on the back side of the remnant as the "Sheet", the material on the front side of the remnant as the "Filament Band", and the material between the two as the "Bridge". The Si and S lines trace out essentially identical structures as seen in Figure 2.11.

The Filament Band and the Sheet are orientated at 10.4° and 16.4°, respectively, with respect to the plane of the sky. This is consistent with the range of $\sim 25^\circ \pm 15^\circ$ in orientation across the Thick Disk observed in the low resolution study (DeLaney et al. 2010).

2.4.2 Ejecta Structure Asymmetry

There is a striking front-back asymmetry in the geometrical structure of the ejecta. The Si, S, and O ejecta in the Sheet have a very narrow velocity profile - along any given line of sight all of the material has only one Doppler component. The structure itself is remarkably well formed in that in almost all places it is <65 km s^{-1} thick - the minimum thickness allowed by our observations. The ratio between the O and Si lines varies considerably - some regions appear almost entirely in one line or the other. As will be discussed in §2.5.5, we do not know if this is due to actual elemental abundance variations or variations in line strength due to density and temperature variations. The structure is nearly continuous except for a hole in the structure in both Si and O (indicated in Figure 2.8).

In the Filament Band the material forms an interwoven filamentary structure. About half of the lines of sight contain more than one Doppler component. In general, the filaments are nearly as narrow as possible given our spectral and spatial resolution (∼0.03pc thick) and can be up to ∼0.3pc long. The emission in the Filament Band has a total width in velocity space of roughly 1500 km s^{-1} along each line of sight, compared to a width of <65 km s^{-1} for the Sheet. Without high resolution data throughout the interior of Cas A, we cannot tell whether these structural asymmetries apply to the entire Thick Disk described by DeLaney et al. (2010).

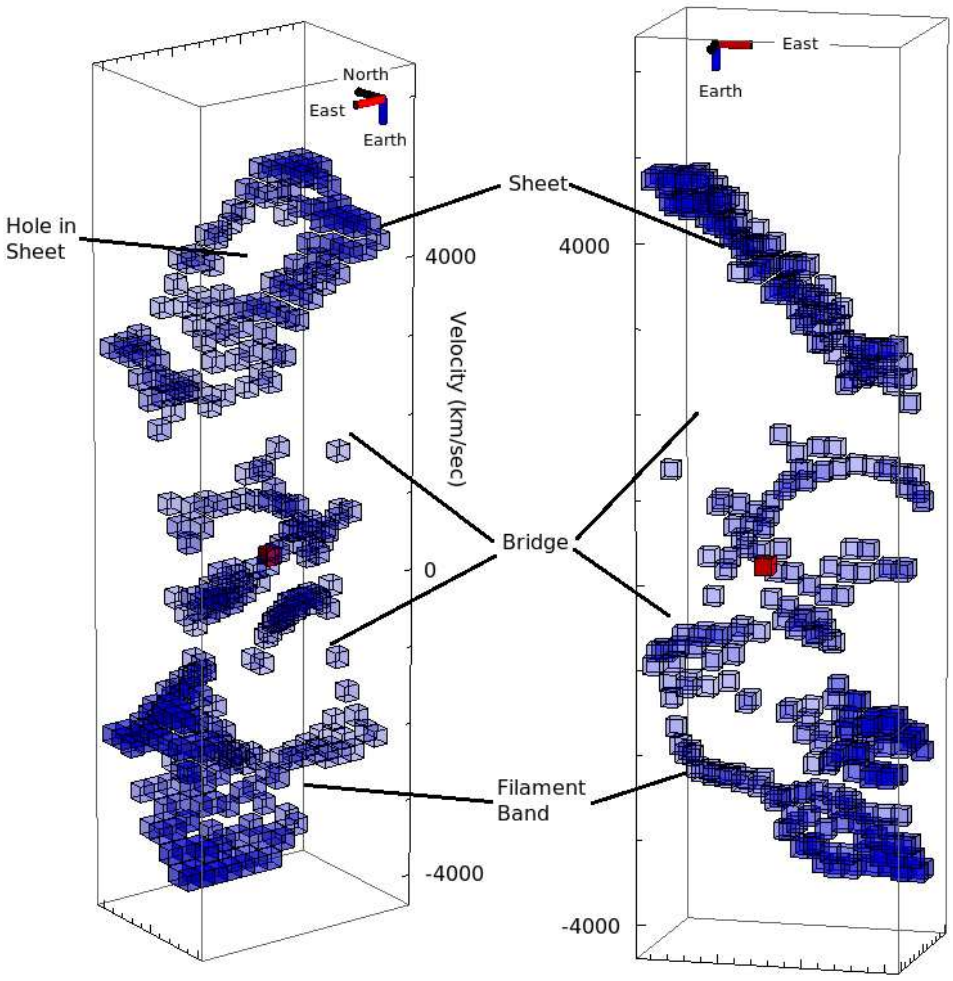

Figure 2.8: 3D plot of the the 25.9μm [O IV] line (blue) as viewed from two different angles. The three major structures discussed in the text are labeled. The red box denotes the location of the central compact object. The velocity axis has been stretched by a factor of 1.8 to highlight the velocity structures discussed in the text. The thinness of the Sheet is shown in the figure to the right, where the Sheet's thickness is roughly the minimum thickness allowed by the plotting symbols.

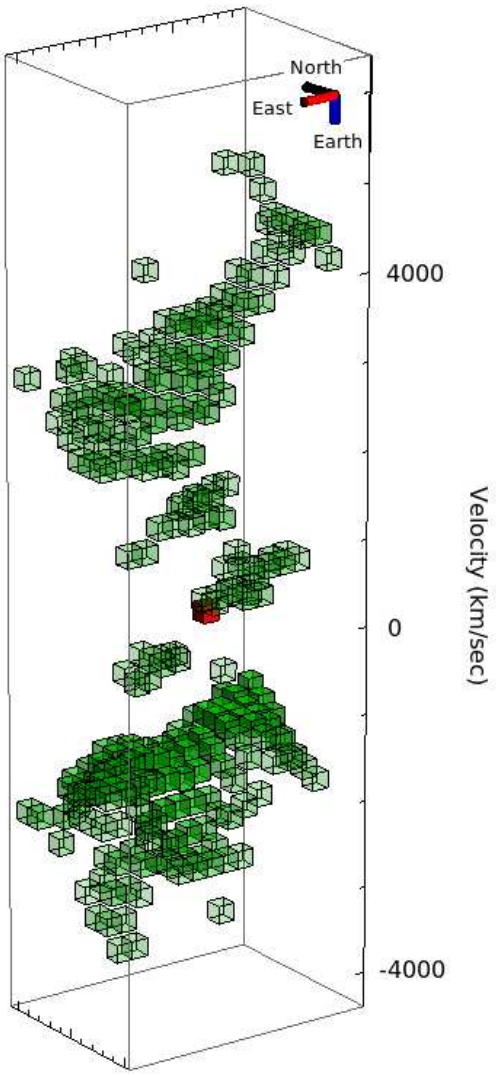

Figure 2.9: 3D plot of the 34.81μm [Si II] line (green). The red box denotes the location of the central compact object. The velocity axis has been stretched by a factor of 1.8 to highlight the velocity structures discussed in the text.

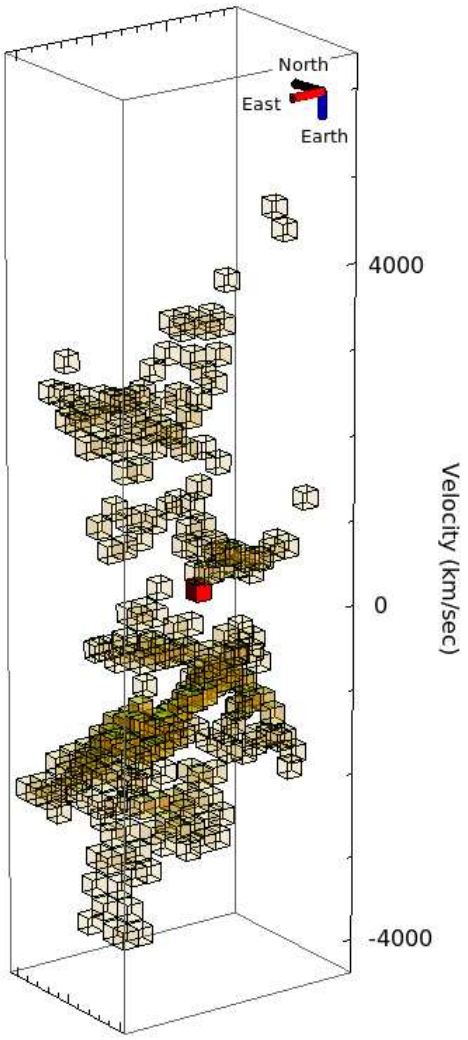

Figure 2.10: 3D plot of the 33.48μm [S III] line (yellow). The red box denotes the location of the central compact object. The velocity axis has been stretched by a factor of 1.8 to highlight the velocity structures discussed in the text.

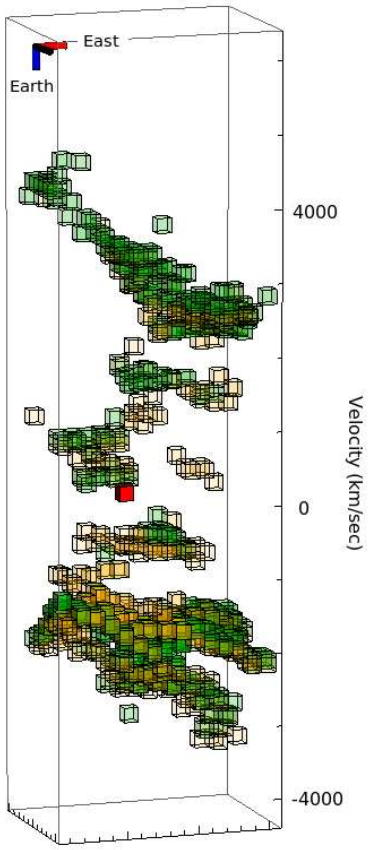

Figure 2.11: 3D [Si II] (green) and [S III] (yellow) map on the same axes. The two lines overlap very strongly.

2.4.3 Ejecta Velocity Asymmetry

There is a substantial difference in the overall velocities of the Sheet and Filament Band regions, on top of the large variations in both intensity and velocity in the various lines. The intensity weighted average velocity of ejecta in the Sheet and Filament Band are 2900 km s^{-1} and -2000 km s^{-1} respectively, as shown by the total line shapes in Figure 2.5.

The velocities of ejecta in the Sheet vary from ∼2000-4600 km s^{-1}, going from East to West. The strongest concentration of Si emission is at ∼3000 km s^{-1}, while the O is spread more evenly over the velocity range.

The average velocity of the ejecta in the Filament Band region ranges from -1500 to -3800 km s^{-1}, going from West to East. The strongest concentration of Si emission in the Filament Band is at ∼-1600 km s^{-1}, much slower than the Si in the Sheet. The O has a larger spread in velocities, but there is substantial O flux at velocities around -1500 km s^{-1}, 500 km s^{-1} slower than any O emission in the Sheet.

Put together, our observations indicate that ejecta in the Filament Band region are typically travelling ∼900 km s^{-1} more slowly than ejecta in the Sheet region.

2.4.4 Radial Velocity Profile Asymmetry

We define the radial velocity profile across nucleosynthesis layers as the mass of the ejecta that are traveling at a given radial velocity for each element. Examples of two radial velocity profiles are shown in Figure 2.12. We can characterize the radial velocity profiles of the original supernova explosion by determining if different nucleosynthetic layers are separated in velocity space. If we observe that Si and O are separated, then we know that Si and O were ejected at different velocities and thus have different radial velocity profiles.

We can qualitatively see a variety of radial velocity profiles in our data. The O and Si in the Sheet appears to be strongly overlapping in Figure 2.13 where [O IV] and [Si II] emission is plotted on the same axes, indicating that two elements were ejected at the same velocity. We quantify the velocity separation between Si and O in the Sheet as follows: for each Si component with flux greater than 100 MJy sr^{-1}, we found the nearest O component along the same line of sight provided that its velocity was within

1000 km s^{-1} of the Si velocity and its flux was greater than 100 MJy sr^{-1}. We plotted the Si velocity vs O velocity from all lines of sight in Figure 2.14. If the elemental layers had identical velocity profiles, the velocities would be equal. We find that the slope of the best fit line of the combined data and forced to pass through the origin is 1.015 $\pm$0.0025. This corresponds to the O having a mean velocity 45 $\pm$14 km s^{-1} greater than the Si at the average position of the Sheet. Since any separation between Si and O is less than the $\sim$100 km s^{-1} uncertainty induced by systematic errors, we conclude that the mean Si and O velocities are identical, within that limit, when both elements are visible.

The rms scatter of the points about the best fit line is 75 km s^{-1}. This is much larger than the random uncertainty in velocity, which is always less than 25 km s^{-1} in both O and Si velocities. This indicates that the scatter is not statistical or instrumental in nature, but is a real variation in the supernova ejecta itself. However, this scatter is very small - it represents a variation of only $\sim$1% in the average ejecta velocity in the Sheet.

Turning now to the Filament Band, in roughly half of the filaments we find no separation between the O and Si velocities. The other half of the filaments are composed almost entirely of either O or Si. The filaments have characteristic separations of order 500 km s^{-1}. This separation cannot be due to contributions from both [O IV] and [Fe II] since we would be able to individually resolve both the [Fe II] and [O IV] lines if both elements were present. We are also not mistaking the [O IV] emission for [Fe II] since the difference in rest wavelengths would result in a velocity change of $\sim$1000 km s^{-1}. Thus, the filaments would still be separated even if we were detecting Fe emission.

We do not attempt to directly compare the Si and O velocities in the Bridge or Filament Band overall, since the ejecta from each element in those regions are often in completely different structures.

We note that the radial velocity profile for every line of sight in the Sheet must be very strongly peaked in both Si and O because we observe one and only one velocity for both elements. However, the radial velocity profile in the Filament Band is much broader since we can see a range of velocities in many lines of sight.

2.4.5 Line Fluxes

We determine line ratios of the 18 and 33 μm [S III] lines for several lines of sight. These lines can be used to determine the density of the ejecta (assuming that they are at a high enough density and temperature) by balancing the collisional excitation and de-excitation rates as well as radiative transitions into and out of the relevent energy levels (e.g. Osterbrock & Ferland 2006). Smith et al. (2009) used this diagnostic on data that had not been deprojected and found that all lines of sight in our field of view had ejecta with electron densities $<$100 cm^{-3}, the lower limit of this density diagnostic. We attempted to identify any Doppler components with densities $>$100 cm^{-3} by determining the [S III] ratio for the 5 Doppler components with the strongest 18μm line. However, in all cases we found that the electron density is $<$100 cm^{-3}, confirming the results of Smith et al. (2009).

We give the integrated line fluxes for two Doppler components from the same line of sight in Table 2.1 as an example of typical values. Note the variation in the [S III] line ratio between the two components, which demonstrates that it is often necessary to deconvolve the data before attempting to extract information from line ratios. We find that this [S III] line ratio varies between roughly 0.02 and 0.4 for deconvolved components, with most ratios around a value of 0.05. Since we do not yet have the appropriate models to determine physical conditions from these line ratios, we defer further discussion of line ratios to a future paper. We address the need for additional modeling in §2.5.5.

2.4.6 [Ne II] Map

Although the 12.8μm [Ne II] line is too weak to extract a substantial number of individual Doppler components, we can map the [Ne II] flux distribution over our field of view. We compare this map to a 25.9μm [O IV] flux map in Figure 2.15. Naively, we expect substantial similarities between the two maps since the elements come from the same nucleosynthetic layer. However, the two maps do not show a strong correlation. We briefly address potential reasons for these differences in §2.5.5.

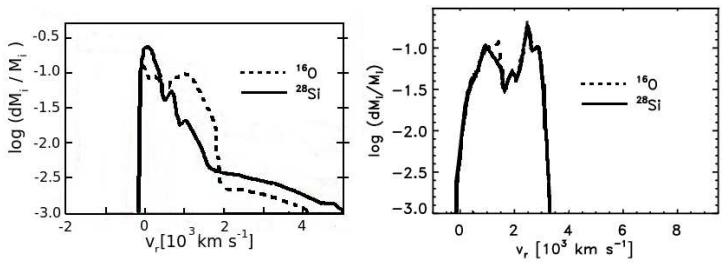

Figure 2.12: Radial velocity profiles for two supernova models, at times when the velocity structure has stabilized. These profiles have been averaged over all radial directions. Left: $15M_{\odot}$, solar metallicity star based on Joggerst et al. (2009) without rotation. Right: $15M_{\odot}$, solar metallicity star with rotation based on Kifonidis et al. (2006). Si and O layers are shown. Note that the Si and O are not easily distinguishable at move velocities. These figures have been altered from their original form for ease of comparison.

Table 2.1: Integrated line flux from front and back emission for a 2.5″ x 2.5″ example region (23:23:31, 58:48:43). Typical uncertainties in line flux are ≤15%.

	S IV 10.5 μm	S III 18.7 μm	O IV 25.9 μm	S III 33.5 μm	Si II 34.8 μm
Back Integrated Flux (10^{-17} W m^{-2})	0.0114	0.0960	1.25	0.632	4.93
Front Integrated Flux (10^{-17} W m^{-2})	0.0298	0.391	2.12	1.02	6.37

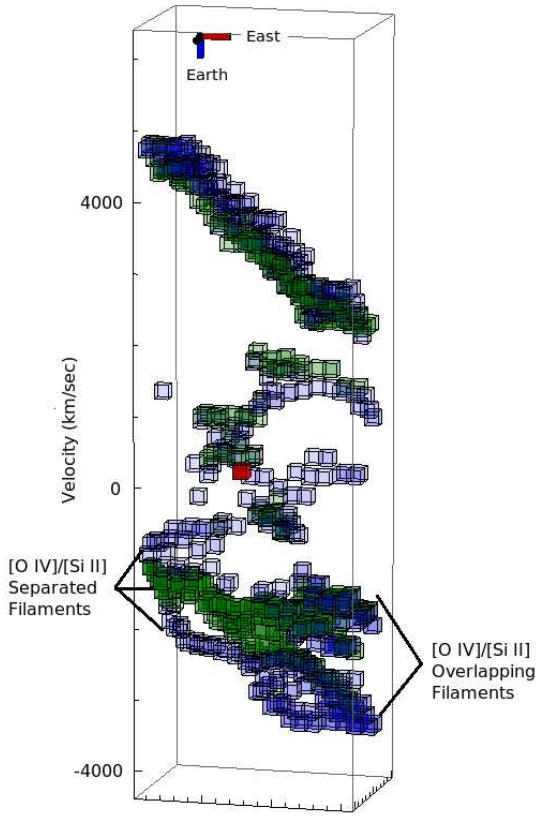

Figure 2.13: 3D plot of the 34.81μm [Si II] line (green) and the 25.89μm [O IV] line (blue) on the same axes. The red box denotes the location of the central compact object. The location of the O and Si overlapping and separated filaments are indicated.

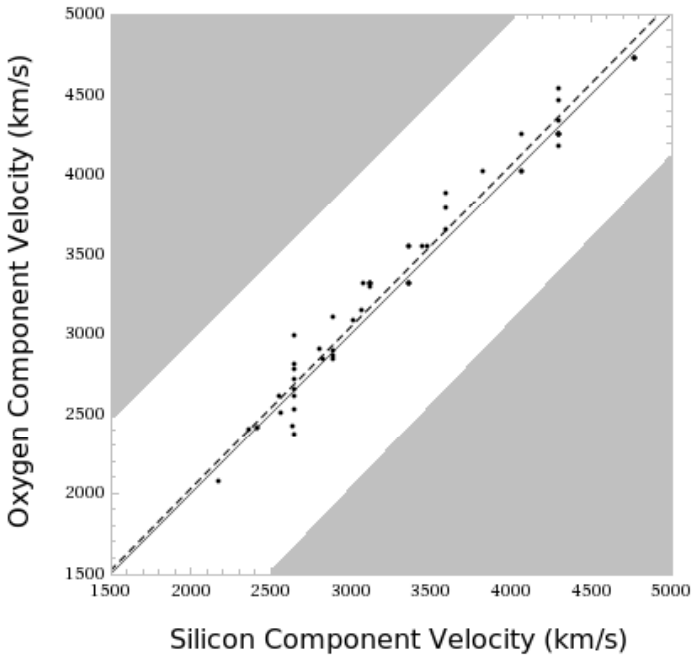

Figure 2.14: Si velocity vs O velocity diagram for the Sheet. The dashed line represents the best fit line to the data, while the solid line is a line with a slope of 1 that passes through the origin. Error bars on each point are roughly the size of the points used for plotting. The white region of the figure represents the area in which both components are within 1000 km s^{-1} of each other. In principle, points could lie anywhere within the white area and still be considered a Doppler component pair.

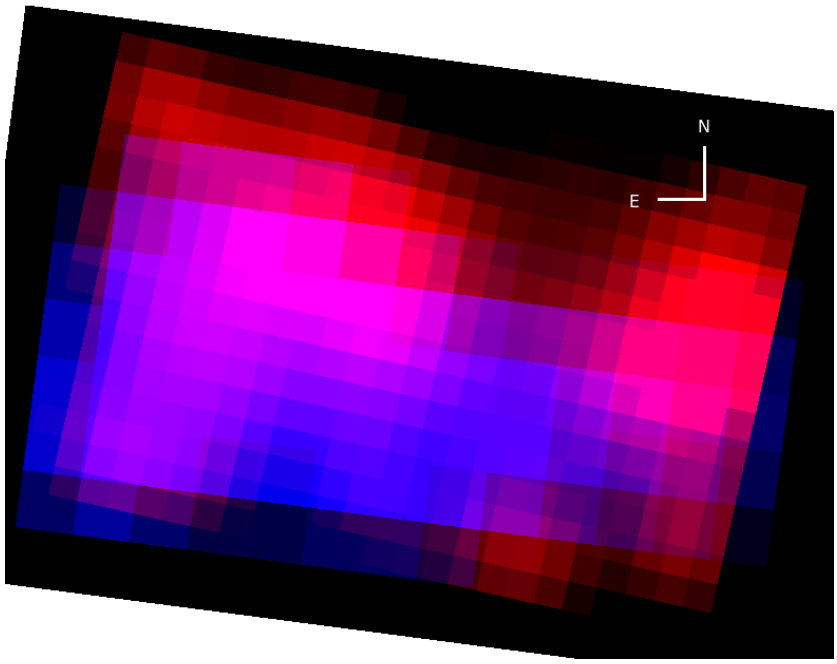

Figure 2.15: Left: Map of [Ne II] at 12.8μm (red) and [O IV] at 25.9μm (blue). The [Ne II] map has been smoothed by 2 pixels in order to increase the signal. There is little correlation between the two ions despite the fact that they originated from the same nucleosynthetic layer.

2.5 Discussion

2.5.1 Supernova Model Background

One of the great outstanding problems in theoretical astrophysics is the basic nature of core-collapse supernova explosions. In contrast, the structure of the star before the supernova explosion is relatively similar for all models. As the massive star fuses different elements during hydrostatic burning, it should produce denser and denser concentric nucleosynthesis layers, forming the classic "onion-skin" model of the star. We concentrate on the central layers of the star - the dense Fe/Ni core, the Si/S layer immediately above the core, and the O/Ne layer above the Si/S.

Any mixing between the layers during the supernova explosion itself could be caused by either partial explosive O burning (Chevalier & Kirshner 1979) or mixing between layers caused by large-scale Rayleigh-Taylor instability fingers created by shocks during the supernova explosion (Winkler et al. 1991). However, our observations indicate that the Rayleigh-Taylor filament scenario is more likely since we observe filamentary structures in ejecta which have not yet encountered the remnant's reverse shock and there is no obvious way that partial explosive O burning could create Si filaments radially flanked by O filaments. Therefore, we do not further discuss any scenarios based on mixing by explosive nucleosynthesis.

Although the initial conditions are well understood, the nature of the piston responsible for the explosion itself is not, with most groups proposing neutrino-driven shocks, while others utilize diffusive, magnetic buoyancy or neutrino-bubble instabilities (Janka et al. 2007). Regardless of the exact nature of the piston, many predictions about the early shock structure of the supernova explosion can be made. As the primary piston drives outwards, it causes a forward shock and eventually sweeps up enough material in the star to form a reverse shock *within the star itself* (Herant & Woosley 1994). This "Explosion Reverse Shock" forms about 10^3-10^4 seconds after the beginning of the supernova explosion and takes $\sim 10^2$ seconds to reach the center of the star (Joggerst et al. 2009). This is different than the "Remnant Reverse Shock", which formed $\sim 10^2$ years later in Cas A when the forward shock swept up enough material to cause the Remnant Reverse Shock to separate (Miles 2009), and has not yet reached the center of the remnant. Figure 2.16 illustrates the distinction between these two reverse shocks.

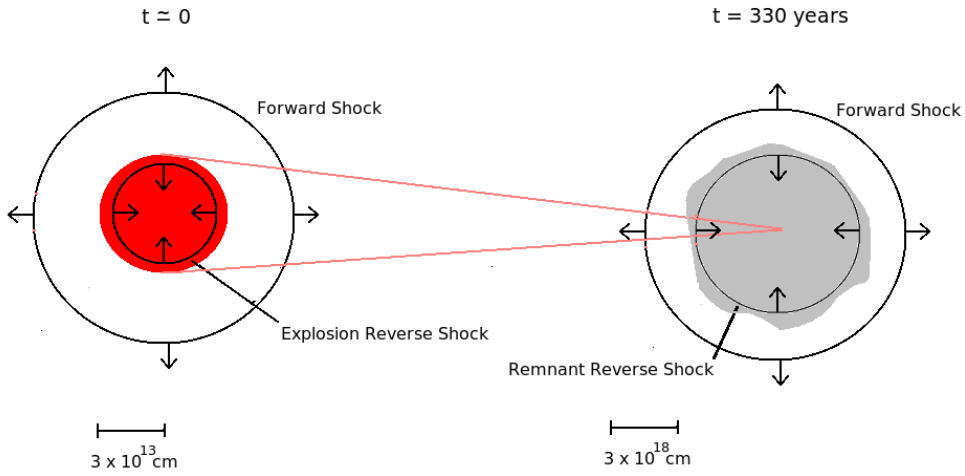

Figure 2.16: Left: The Explosion Reverse Shock and Remnant Reverse Shock with ejecta (gray). The red circle represents the progenitor star (left).

The Explosion Reverse Shock forms in the outer layers of the star and propagates toward the center of the star, forcing the less dense outer nucleosynthetic layers into the denser layers deeper within the star. This can cause mixing between the layers and potentially forms filaments from Rayleigh-Taylor instabilities (Herant & Woosley 1994). The amount of mixing and degree of filamentation depends on the the speed of the reverse shock, which can vary by roughly an order of magnitude in models of stars with different masses (Joggerst et al. 2009). A strong and fast Explosion Reverse Shock can cause complete mixing between many layers and prevents the production of filaments because it sweeps by so quickly that filaments do not have time to grow. The signature of this phenomenon is well mixed sheets of ejecta. On the other hand, a slower Explosion Reverse Shock can result in large filaments because it moves slowly enough that the filaments have time to develop. A very weak shock would not be strong enough to cause much mixing at all between most elements, leaving the nucleosynthetic layers spatially separated (Joggerst et al. 2009).

The Explosion Reverse Shock simultaneously modifies the radial velocity profile of the ejecta across concentric nucleosynthetic layers. Elements that have been well mixed by the Explosion Reverse Shock (indicating a strong and fast Explosion Reverse Shock) should have nearly identical velocities upon ejection, while unmixed layers (indicative

of a weaker and slower Explosion Reverse Shock) can have velocities that differ by 1000s of km s^{-1}. This is a key distinguishing feature between supernova models. Some models predict that the Si/S and O layers will have essentially identical velocities, while other models predict that the layers can be separated by 1000s of km s^{-1} (Figure 2.12 - Joggerst et al. 2009; Kifonidis et al. 2006). Even within very similar models, the separation between layers can be a function of the initial conditions within the explosion - Joggerst et al. (2009) predict that the Si/S and O layers will have nearly identical velocities for $25M_{\odot}$ solar metallicity stars, while they will be separated by $\sim$1000 km s^{-1} for $15M_{\odot}$ solar metallicity stars.

An alternative to spherical shocks is a jet-induced supernova explosion (e.g. Burrows et al. 2007). In this scenario, the explosion is dominated by MHD jets created in rapidly rotating stars. When these stars explode, the jets induce a bipolar outflow and create powerful bow-shocks as they move through the star. These transverse shocks eventually collide at or near the equator of the star, leading to a torus of ejecta about the star's equator (e.g. Khokhlov et al. 1999). Stars with moderate rotation may have supernovae with both spherical and weak transverse jet induced shocks (Burrows et al. 2007).

2.5.2 Nature of the Explosion

We can use supernova explosion models as a guide to which physical properties may influence the observed asymmetries. The fundamental cause of the ejecta structure, the ejecta velocity, and the radial velocity profile asymmetries described in this paper may be variations in the Explosion Reverse Shock, which were potentially caused by the variations in the forward shock. In this model, the Explosion Reverse Shock was very strong and moving very quickly in some directions, leading to the Sheet structure where the elements are mixed in velocity space and no filaments are seen. In other directions it was slower, leading to filaments composed of both Si and O. In yet other directions it was very weak and slow, leading to well separated filaments.

Another potential source of asymmetries are those that form in the forward shock within the first $\sim$100 milliseconds in the models of Burrows et al. (2007) as well as standing acoustic shock instability (SASI) models of Blondin et al. (2003). These instabilities allow the initially steady-state, spherically-symmetric forward shock to become highly asymmetric in just a few crossing times (Blondin et al. 2003). The origin of

these instabilities is the response of the post shock pressure to changes in the forward shock radius and happens while the forward shock is roughly stationary and still very near the core of the star. If the pressure in one regions becomes only slightly higher than equilibrium, it will push the forward shock outward. The preshock ram pressure drops with increasing radius, so the outward shock displacement leads to smaller pressure behind the forward shock. But, if the postshock pressure radial profile is steeper than the preshock ram pressure profile, positive feedback and a standing acoustic wave are produced (Blondin et al. 2003). This leads to a forward shock with low-order asymmetry. Presumably, the Explosion Reverse Shock would be strongly affected by this asymmetry when it separates from the forward shock.

Jet-induced supernova explosions do not appear to be an attractive alternative for explaining our observations of Cas A. The distinct, tilted front/back structures that we report here and are part of the DeLaney et al. (2010) "Thick Disk", are not orientated correctly to be formed as a torus in a jet induced supernova explosion. They are nearly in the same plane as the jet/counter-jet, not perpendicular to it as the jet models require. While the jets do produce a slight bipolar asymmetry in the ejecta, there is no obvious way in which the jets cause most of the ejecta asymmetries described in §2.4. Furthermore, Cas A's jets do not appear to have enough kinetic energy in order to cause the supernova explosion (Laming et al. 2006).

Wheeler et al. (2008) propose that the structures normally called the "jet" and "counter-jet" are not the main jets, but rather secondary instabilities. In this model, the jets responsible for the explosion are two notable Fe blowouts located in the Southeast and Northwest of the remnant. However, the 3D reconstructions of DeLaney et al. (2010) show that these two blowouts do not form an axis. The Fe blowouts also are not nearly perpendicular to the "Thick Disk" as expected in a jet induced explosion.

We do not further consider jets as the source of Cas A's asymmetries any further since both jet-induced scenarios do not seem to be plausible.

Other models can also produce ejecta asymmetries from rotation without using jets to induce the supernova explosion. However, the published results of such models (e.g. Kifonidis et al. 2006) do not document any of the key asymmetries in ejecta structure, velocity, and radial velocity profile that we need to compare with the current observations. It is clear that one key to understanding and reproducing the asymmetries

is to have models that predict the average ejecta velocity as well as the radial velocity profile *as a function of direction.*

2.5.3 Relationship Between the O and Si/S Layers

X-ray observations have led to the suggestion that Cas A's nucleosynthetic layers have undergone large-scale overturning in some regions, causing less dense layers to be interior to layers which originated closer to the star's core (e.g. Hughes et al. 2000). In most directions we find no evidence of this overturning as the the O and Si/S layers are nearly perfectly correlated in velocity space (see Figures 2.12 and 2.14). This is consistent with IR and X-ray observations that indicate that Si/S and O emission is co-located on much of the Bright Ring (e.g. Ennis et al. 2006). However, in part of the Filament Band we do find substantial separation between nucleosynthetic layers. This is roughly consistent with the separation between layers seen in the X-ray, but does not correspond to a simple overturning of the layers since the O-layer is observed on *both* sides of the initially denser Si/S layer in velocity space.

While this intertwining of O and Si/S layers may be evidence of some sort of mixing between nucleosynthetic layers in some parts of the star, it does not apply in other directions. Future supernova explosion models that better address the asymmetries seen in Cas A may shed light on this interesting phenomenon.

We also note that our results are similar to those of Fesen et al. (2006). Based on Hubble Space Telescope observations of select regions of the remnant, they also concluded that there was substantial spatial variation in the degree of mixing of the layers in Cas A. Their data consisted of knots composed of lighter elements that originated in the outer layers of the star; our results show that the variability in mixing remains even down to the denser interior layers.

2.5.4 Velocity Offset

Previous authors observing ejecta in the optical found that the center of expansion of the ejecta was offset along the line of sight from the geometrical center of the partial spherical shell (caused by ejecta interacting with the Remnant Reverse Shock) by $\sim$770 km s^{-1} (Reed et al. 1995). Our new IR results are roughly consistent with this result - we find

an offset of $\sim$900 km s^{-1} along our line of sight in the same direction. However, Reed et al. (1995) speculated that this was due to a difference in density of the circumstellar material between the back and front of the remnant. This is inconsistent with our data - the interior ejecta visible in the infrared are unaffected by the circumstellar material because they have not yet encountered the Remnant Reverse Shock. Thus, we believe that this velocity offset is the result of an asymmetry in the supernova explosion itself rather than an asymmetry in the circumstellar material.

2.5.5 Interior Conditions

Our observations raise an interesting puzzle with respect to Fe. We do not definitively detect any Fe in the interior, despite Fe II, Fe III, and Fe VII lines within the wavelengths accessible to *Spitzer*'s IRS module. This could either be due to a lack of Fe in the interior of the remnant or because the Fe present is not in the correct physical conditions to emit detectable lines. We believe that the latter scenario is more likely since recently shocked Fe is observed on the Bright Ring (e.g. Hughes et al. 2000; Eriksen et al. 2009) and we know of no mechanism which would force all the Fe, and only the Fe, to be ejected only in a narrow torus.

One possible solution to this puzzle is that the Fe is at lower density than the observed Si and O. There are multiple explanations for how this may occur, but we will only discuss one here. Although the Ni/Fe layer is initially more dense than the Si/S and O layers, it may not have experienced the same modifications to its density distribution as the outer layers. For example, if the Explosion Reverse Shock was weak when reached the Fe/Ni core, it would not cause the Rayleigh-Taylor filamentation that is likely responsible for the dense knots of Si/S/O that we observe in the interior. The phenomenon of density enhancements to outer layers but not the core is seen in some of the models of Joggerst et al. (2009). Fe may not be observable without this density enhancement.

A similar puzzle arises with respect to the Si and O lines. In some regions with coherent structure like the Sheet, we see emission which is almost entirely O or Si. These variations in line strengths could be due to either variations in local abundance ratios between the elements or density and temperature variations. We find that the brightness of a region in Si is uncorrelated with how bright it is in O and vice versa.

Similarly, we observe that the [Ne II] and [O IV] maps show substantial differences although both elements may have come from the same nucleosynthetic layer. We speculate that this is because the emissivity of the two lines is a function of density and temperature, and the variation in line flux is therefore reflecting a variation in physical conditions. Another possibility is that we are observing explosively nucleosynthesized Ne and/or O, which could mean a spatial separation between the elements.

We look forward to future models which balance photoionization rates (as opposed to the collisional ionization rates used in the usual 18/33 μm [S III] diagnostic) in order to determine line ratios as a function of temperature and density. These models should be able to probe the low temperatures and densities present in Cas A's center. Not only will we be able to better address the puzzles presented above, but we will also be able to better constrain the temperature and density of the interior ejecta.

2.5.6 Predictions for the Next 30-500 Years

Cas A's appearance in the X-ray is dominated by ejecta which have recently encountered the Remnant Reverse Shock. Thus, the central ejecta arriving at the Remnant Reverse Shock will mark a transition after which Cas A will contain bright central emission in the optical and X-ray. This situation will be analogous to the supernova remnants N132D Blair et al. (2000) and Puppis A (Winkler & Kirshner 1985). Like in N132D, we will observe a ring of ejecta with arcs and clumps of bright, recently shocked ejecta interior to the ring. We note that the two scenarios are not an exact analogue since N132D's appearance is dominated by its forward shock interacting with the surrounding environment. The remnant will still be a shell morphology remnant (since the ring will be limb brightened), but a substantial fraction of the overall X-ray emission will be from shocked ejecta in the interior. However, like in Puppis A we expect the central ejecta to be O rich since our IR observations detect strong O lines in the interior ejecta.

We can make explicit predictions about when the central ejecta should encounter the Remnant Reverse Shock with our knowledge of the current velocity structure of the ejecta and by assuming, in the limiting case, that the Remnant Reverse Shock is roughly stationary in the current epoch (Morse et al. 2004). On the back side of the remnant, we expect the Sheet to begin arriving at the Remnant Reverse Shock in slightly under 30 years at about RA: 23:23:25 and Dec: 58:48:5. The X-ray and optical emission may

initially be dominated by O group emission, since the part of the Sheet with the highest velocity is dominated by O emission in our observations. The greatest concentration of Si group emission on the back side of the remnant should arrive at the Remnant Reverse Shock in approximately 220 years. If the Remnant Reverse Shock actually begins moving inward in the external reference frame during this period, then these times will be shorter.

On the front of the remnant, the ejecta in the Filament Band will begin to arrive at the Remnant Reverse Shock in about 100 years. The ejecta in the Filament Band with the largest velocity are the overlapping filaments, so the emission will initially be strong in both O and Si. The separated filaments will begin to arrive at the reverse shock in about 260 years. The emission will intially be dominated by O. The Si group emission should begin about 500 years from the present time in this direction and will be followed by more O group dominated emission several decades later. We note that the substantial separation in arrival times of the O and Si group in this direction is consistant with the Ennis et al. (2006) result in which emission in some regions are observed to contain almost exclusively O and Ne, with little Si.

2.6 Conclusions

We create a 3D reconstruction of the central ejecta of Cas A at unprecedented spectral resolution using photoionized infrared ionic lines. We observe a large number of asymmetries that are most likely caused by asymmetries in the supernova explosion itself rather than the circumstellar environment. Si and O emission with nearly identical velocities are seen in co-located sheets less than 100 km s^{-1} thick on the back side of the remnant. Toward the front, by contrast, we observe filaments with both Si and O present, while along different lines of sight we observed well-separated Si and O filaments that are roughly consistent with X-ray observations. The average velocity of all ejecta varies strongly as a function of direction. We observe that the interior emission is offset by $\sim$900 km s^{-1} along our line of sight as was previously observed in the optical. However, we do not believe that this asymmetry was caused by the circumstellar environment because the interior ejecta can not be affected by the ISM until they reach the forward shock. We hypothesize that the asymmetries could be produced by

asymmetries in the Explosion Reverse Shock.

Photoionization models are required in order to determine the density, temperature, and ionization state of the center of the remnant. These models are likely to be produced in the near future and will allow us to further address the central conditions of the remnant. One key question to be answered is whether or not the lack of a detection of any Fe lines indicates a lack of interior Fe, or that the Fe is present, but not in the correct physical state to produce observable lines.

Finally, we note that Cas A will provide an even more fertile ground for future observations as the interior ejecta encounter the front and back Remnant Reverse Shocks, starting in $\sim$30 years.

Chapter 3

Ejecta on the Bright Ring

Note: A modified version of this article has been submitted to the Astrophysical Journal: Isensee, K., Olmschenk, G., Rudnick, L., DeLaney, T.A., Smith, J.D., Rho, J., Reach, W., Kozasa, T., and Gomez, H. 2011, ApJ in preparation

We present a 3-dimensional analysis of the supernova remnant Cassiopeia A using high resolution spectra from the *Spitzer Space Telescope*. We observe supernova ejecta both immediately before and during the shock-ejecta interaction. We determine that the reverse shock of the remnant is spherical to within 7%, although the center of this sphere is offset from the geometric center of the remnant by 810 km s^{-1}. We determine that the velocity width of the nucleosynthetic layers is $\sim$1000 km s^{-1} in a given region, although the velocity width of a layer along any given line of sight is $<$250 km s^{-1}. Si and O, which come from different nucleosynthetic layers in the progenitor star, are observed to be coincident in velocity space in some directions, but segregated by up to $\sim$500 km s^{-1} in other directions. We compare these observations of the nucleosynthetic layers to predictions from supernova explosion models in an attempt to constrain such models. Finally, we observe small-scale velocity structures in the recently shocked ejecta. We determine that this corrugation is likely caused during the supernova explosion itself, rather than hundreds of years later at the remnant's reverse shock.

3.1 Overview

In this paper, we present an analysis of high spectral resolution *Spitzer* mappings of the ejecta on the Bright Ring of Cas A. This data set is an extension of that used in the previous chapter, and it contains regions with both recently shocked and interior ejecta. In §3.2 we present the observations and discuss the methods used in our analysis. We describe those results in §3.3 and discuss the physical implications in §3.4.

3.2 Observations and Analysis

The *Spitzer* Infrared Spectrograph (IRS) was used on August 30, 2007 to create spectral maps of select relatively bright regions in Cas A whose locations are shown and labeled in Figure 3.1. High-resolution spectra (R$\sim$600 for all wavelengths) were taken from 20-35μm using the Long High (LH) module in all regions and from 10-35μm using both the Long High and Short High (SH) modules in the Southwest region. The spectral FWHM of these observations is about 0.06μm at 35μm and about 0.02μm at 13μm. The LH data were taken using a 61 second exposure at each position while the SH data were taken using a 31 second exposure at each position. The spatial resolution of the observations is $\sim$1.25$''$ and $\sim$2.5$''$ for the SH and LH modules respectively. The background, which was taken from observations adjacent to the remnant, was subtracted and 3D cubes were created using the S19 version of the IRS pipeline and the CUBISM software package (Smith et al. 2007). The uncertainties in flux for each line of sight were calculated from the IRS pipeline using standard error propagation of the BCD level errors.

The undersampling of the IRS modules limits our uncertainties. This is a systematic error that exists in the wavelength calibration data themselves, and is worst at the short-wavelength end of both the SH and LH modules. Our obtainable wavelength accuracy is limited to roughly 1/2 of a spectral bin, or about 100 km s^{-1}. The relative wavelengths for a given line can be measured with higher accuracy from position to position or within multiple Doppler components in a given position.

3.2.1 Spectra

Cas A's infrared spectrum is dominated by bright emission lines as shown in Figure 3.2. The LH observations contain lines from [O IV] at 25.9μm, [S III] at 33.48μm, and [Si II] at 34.81μm. The lines observed in the LH module typically have peak fluxes from 100-10,000 MJy sr^{-1}, with an rms noise of $\sim$20 MJy sr^{-1}. The SH observation contains lines from Ne, S, and Fe. Typical peak fluxes are $\sim$300 MJy sr^{-1}.

3.2.2 Doppler Deconvolution

We performed a Doppler deconvolution of the spectral lines for each line of sight from each ion separately using a spectral CLEAN algorithm (Ding et al. 1999). We determined the uncertainties in Doppler velocity for each Doppler component by applying the spectral CLEAN to synthetic line data with a realistic range of signal to noise ratios, and using line free data in order to model the noise. For both procedures, we use identical techniques to those described in Isensee et al. (2010).

Using synthetic data, the uncertainty in velocity for a single, isolated Doppler component was determined to be <25 km s^{-1}, however, we could not detect two components along the same line of sight that were within 65 km s^{-1} of one another. Therefore, uncertainties in the absolute velocities are limited by the systematic errors in the calibration of $\sim$100 km s^{-1} rather than random uncertainties.

As in previous studies (Reed et al. 1995; DeLaney et al. 2010; Isensee et al. 2010), we assume that the ejecta have been freely expanding at a constant velocity in order to determine their spatial coordinate perpendicular to the plane of the sky. DeLaney et al. (2010) demonstrate that this is a good assumption for IR emission by showing that nearly all ejecta plotted on a Velocity vs. Radius plot fall on a semi-circle. We make a similar Velocity vs. Radius plot in Figure 3.3 from our data set and find that ejecta in these regions fall on a semi-circle that is consistent with that found by DeLaney et al. (2010). The assumption of constant velocity is still valid despite the fact that the ejecta were likely decelerated during the supernova explosion itself. The subsequent behavior after the explosion is essentially identical to free expansion at a reduced velocity because any deceleration happened near t=0, z=0 where z is the spatial coordinate perpendicular to the plane of the sky.

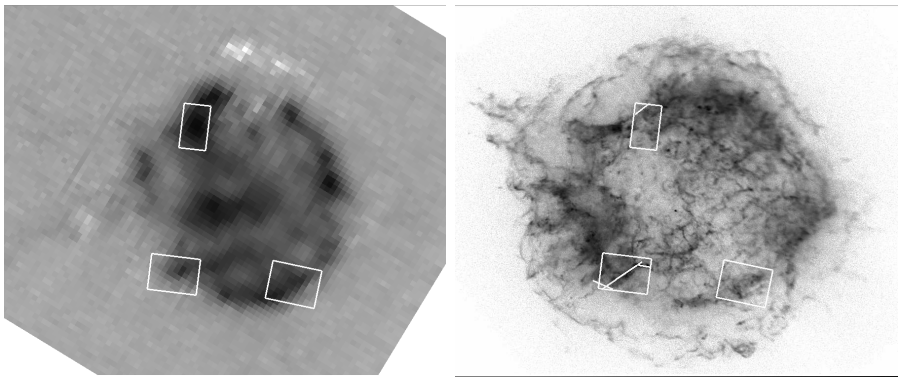

Figure 3.1: 34.81μm [Si II] *Spitzer* IRS map (left) and X-ray Si *Chandra* map (right) of Cas A. The regions of high resolution data discussed in this text are indicated by the boxes. The planes shown in Figure 3.9 are indicated by the straight lines in the X-ray image.

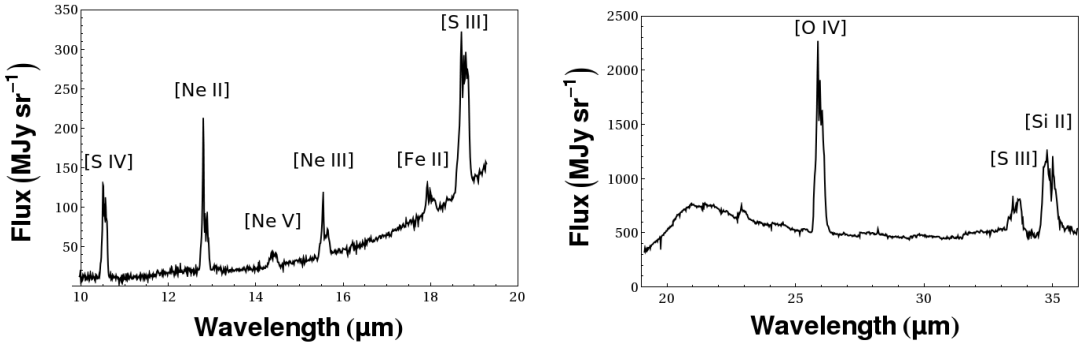

Figure 3.2: Typical spectra from the SH and LH *Spitzer* IRS module of emission in Cas A.

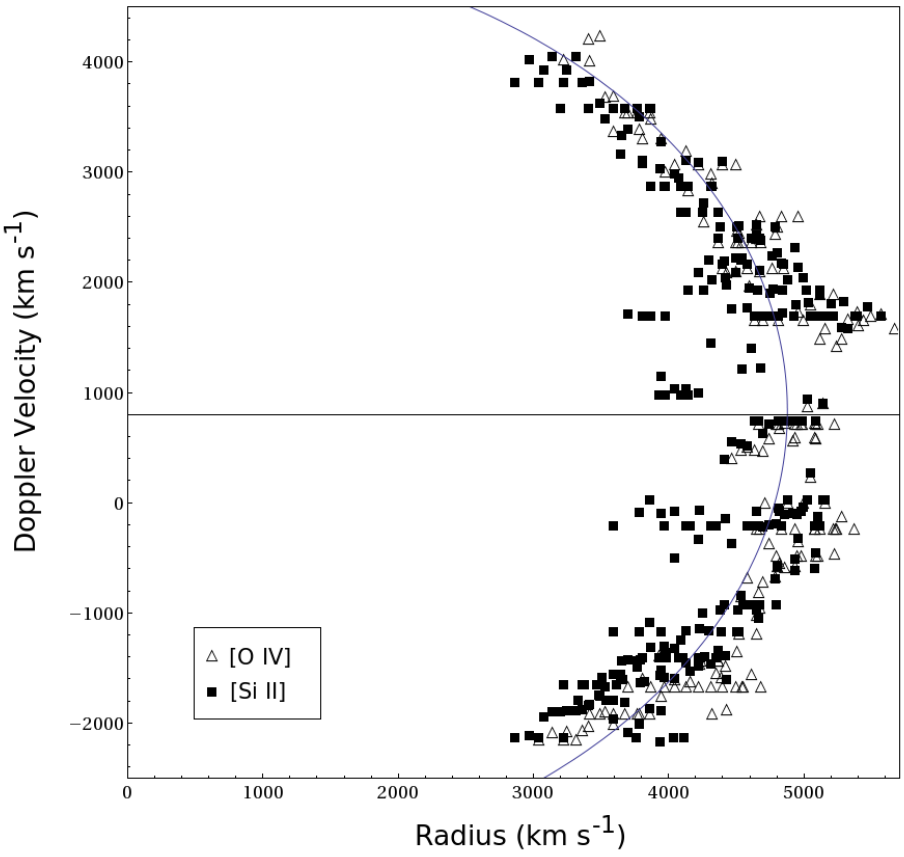

Figure 3.3: Velocity vs radius plot for Si (filled squares) and O (open triangle). Our assumption of no deceleration is good since all the ejecta lie nearly on the same semi-circle. Note that the semi-circle is offset from 0 velocity by 810 km s^{-1} as indicated by the solid horizontal line.

3.3 Results

3.3.1 3D Maps

We plot the Doppler components from both the 25.89μm [O IV] and the 34.81μm [Si II] lines in Figures 3.4, 3.5, and 3.6 for the Southwest, Northeast, and Southeast regions respectively. We converted our velocity coordinates to spatial coordinates using the conversion factor between the two determined by DeLaney et al. (2010). This conversion factor is more appropriate than one calculated from our own data since it uses data from the entire remnant rather than a few select regions. The flux from each component is displayed by varying the transparency; the brightest voxel for a given ionic line is 80% opaque, while the opacity of all other voxels is linearly scaled downwards as a function of the intensity of the Doppler component. We have not plotted very weak ejecta with total fluxes less than 15% that of the brightest velocity component. The other strong line, the 33.48μm [S III] line, is from the same nucleosynthetic layer as Si and traces out nearly identical structures to the 34.81μm [Si II] line. Therefore, we do not show it here. The low density of the interior ejecta ($\sim$100 e$^-$ cm^{-3} - Smith et al. 2009) implies that line of sight absorption will be minimal. We note that we are likely only observing the densest ejecta since a small decrease in density will result in a substantial drop in emissivity.

The ejecta in the SW region form a distinct shell-like structure. The O and Si ejecta all lie along the same shell, although they fill different parts of the shell. On average, there are only 1.3 Doppler components per line of sight, indicating that the thickness of the shell is $\leq$250 km s^{-1} along any given line of sight. The brightest ejecta in the NE region also forms part of a shell, but there are substantially more dim ejecta inside of the shell than in the SW. O and Si lie both on the shell and inside of the shell, although it appears that some of the O and Si is systematically separated in velocity space (see § 3.3.6). The SE region consists of an irregularly shaped region of both Si and O emission in addition to a region dominated by O emission in the western most part of the region.

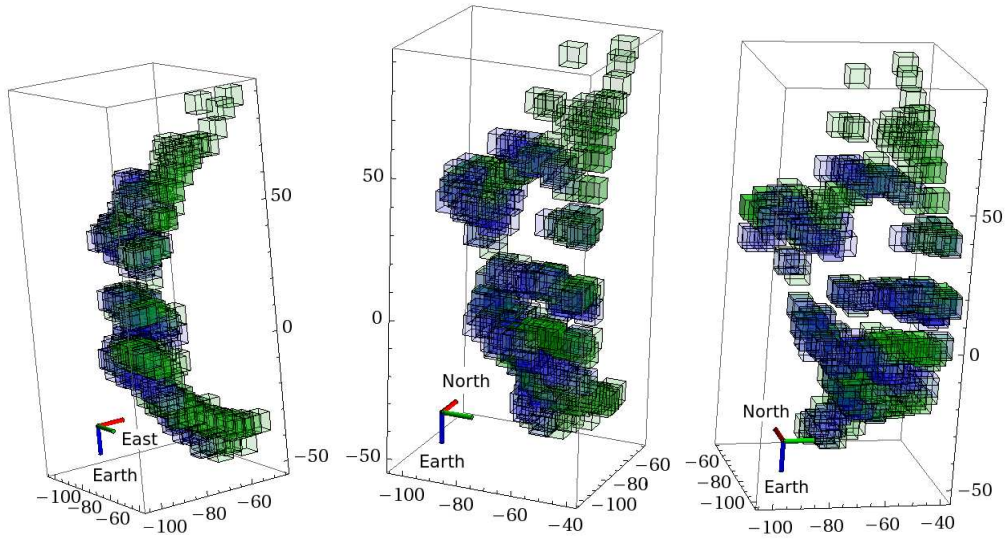

Figure 3.4: 3D plot of the the 25.9μm [O IV] line (blue) and 34.8μm [Si II] line (green) in the Southwest of the remnant as viewed from three different angles. The units on the axes are arcseconds from the center of expansion of the remnant.

3.3.2 Iron

We observe [Fe II] with the SH module at 17.9μm in the SW. We plot the Doppler components from this line with Si and O emission as shown in Figure 3.7. The SH data were binned 2 by 2 pixels to increase the signal to noise ratio. It is clear that the Fe lies on the Si+O shell described in the previous section.

We confirm that the 25.9μm line is the 25.89μm [O IV] and not the 25.98μm [Fe II] line by comparing the Doppler structure of the 25.9μm to that of the 34.81μm [Si II] line for several lines of sight in the SE, SW, and NE. As an example, we display the results for one line of sight with strong 17.9μm Fe emission in Figure 3.8. We show the Doppler structure for the 25.9μm line under the assumption that it is all [O IV] and all [Fe II]. We obtain an excellent match under the assumption of [O IV], but a poor match under the assumption of [Fe II] even along this line of sight where we see relatively strong Fe at other wavelengths. We find no evidence for Fe at 25.9μm for 10 other lines of sight, confirming the results of Isensee et al. 2010. Therefore, we assume for the remainder of this paper that the 25.9μm line is entirely due to [O IV] emission.

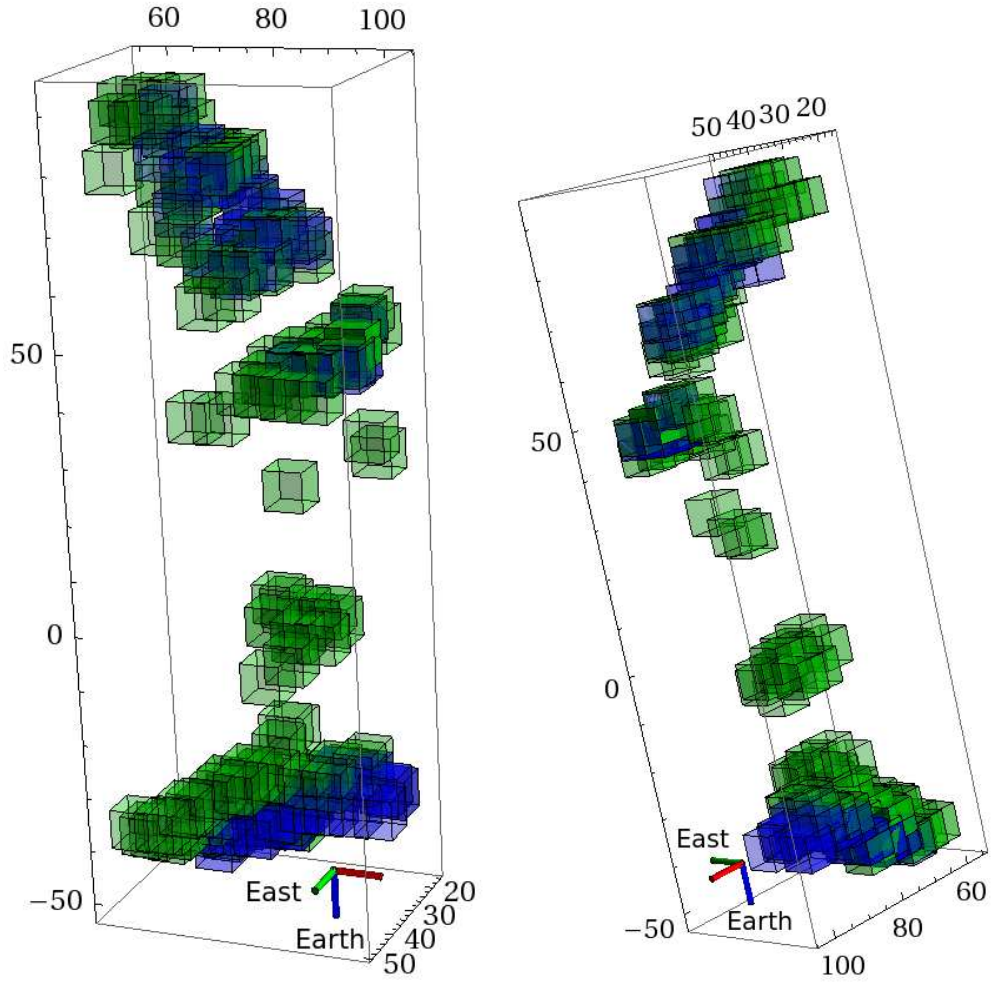

Figure 3.5: 3D plot of the the 25.9μm [O IV] line (blue) and 34.8μm [Si II] line (green) in the Northeast of the remnant as viewed from two different angles. The units on the axes are arcseconds from the center of expansion of the remnant.

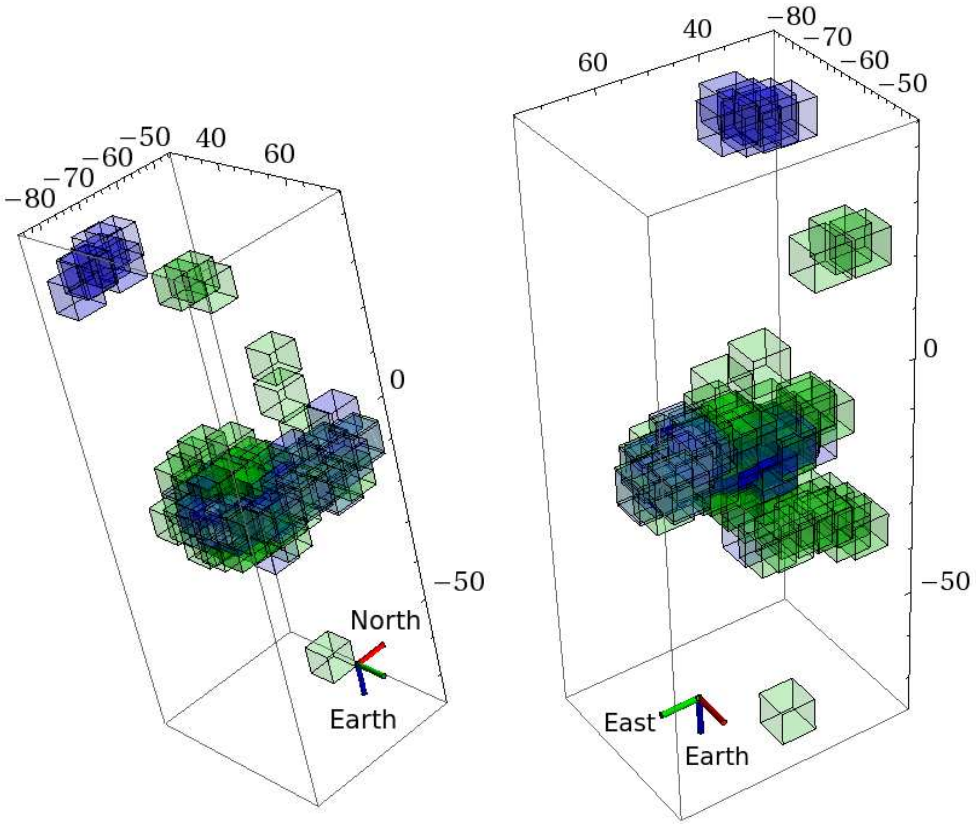

Figure 3.6: 3D plot of the the 25.9μm [O IV] line (blue) and 34.8μm [Si II] line (green) in the Southeast of the remnant as viewed from two different angles. The units on the axes are arcseconds from the center of expansion of the remnant.

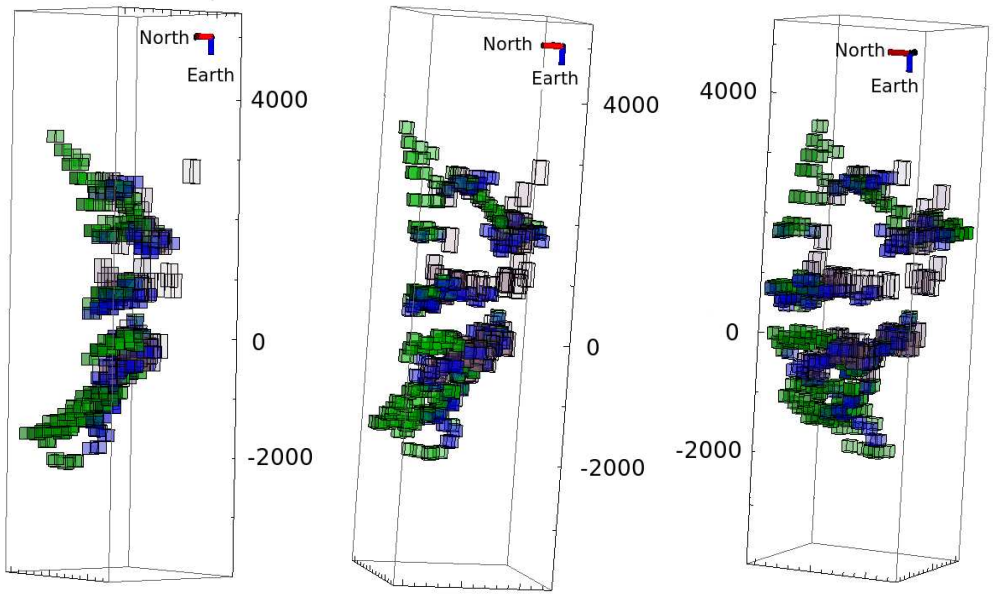

Figure 3.7: 3D plot of the the 25.9μm [O IV] line (blue), the 34.8μm [Si II] line (green), and the 17.9μm [Fe II] line (purple) in the Southwest of the remnant as viewed from three different angles. The velocity axis has been stretched by a factor of approximately 1.8 in order to better highlight the Doppler structure of the region. The Fe emission lies on the same shell as the O and Si emission.

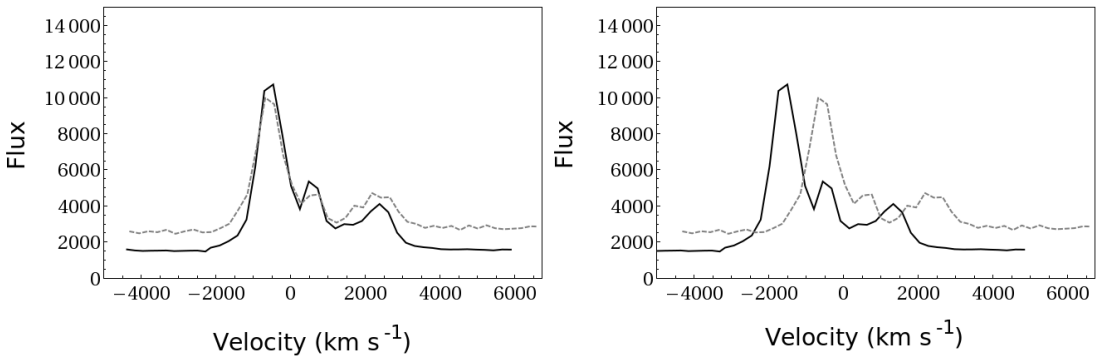

Figure 3.8: Velocity plot for the [Si II] line (solid) over-plotted with the 25.9μm line (dashed) shifted under the assumption that it is either all [O IV] (left) or [Fe II] (right). The lines have been normalized such that the integrated flux is equal for both lines. The velocity structure matches very well for the assumption that the 25.9μm line is all O, but matches very poorly under the assumption that it is composed of Fe.

3.3.3 Comparison to X-ray Emission

We compared the locations of the IR ejecta to X-ray ejecta detected in the 2004 *Chandra* observations of Cas A (see Hwang et al. 2004). The spectral resolution of the X-ray images is not sufficient to accurately determine the Doppler velocity for most lines. Therefore, we show the 3D location of the X-ray ejecta as planes perpendicular to the plane of the sky in Figure 3.9. These planes represent the forward edge of the X-ray ejecta as seen in Figure 3.1. We know that the X-ray material has been recently shocked since the ejecta will only be at the appropriate ionization states and temperatures if it has recently encountered the reverse shock - the ejecta will ionize up to states that are difficult to observe in the X-ray within ∼100 years (Mazzotta et al. 1998).

Most of the bright IR ejecta are immediately behind the leading edge of the X-ray material. Since it takes some time for a plasma to up ionized to ions visible in the X-ray, this is consistent with the picture that the brightest IR ejecta have been recently shocked.

3.3.4 Geometric Structure of Ejecta

We observe that the ejecta plotted in the previous section appear to have a distinct shell-like geometry in the Southwest and Northeast regions. We attempt to characterize the shape of this shell with an ellipsoid by fitting bright emission with a total flux at least 15% that of the brightest Doppler components from all 3 regions.

We determined the best-fit ellipsoid characterized by 8 components - the 3 spatial coordinates for the center of the ellipsoid, the 3 axes lengths, and 2 rotation angles. We minimized the intensity weighted RMS residuals in the 3D space by iteratively stepping through all plausible combinations of parameters. We show our best fit ellipsoid in Figure 3.10. The lengths of the axes in the plane of the sky are $103''$and $98.3''$, and the length of the axis perpendicular to the plane of the sky is $97.2''$. The ellipsoid is a sphere to within 7%. The average residual from the best fit ellipsoid is 270 km s^{-1}, which is roughly 5% of the total velocity for ejecta on the ellipsoid. The center of this sphere is offset from the geometric center of the ejecta by 810 km s^{-1} along our line of sight. This offset can also be seen in the Velocity vs. Radius plot shown in Figure 3.3.

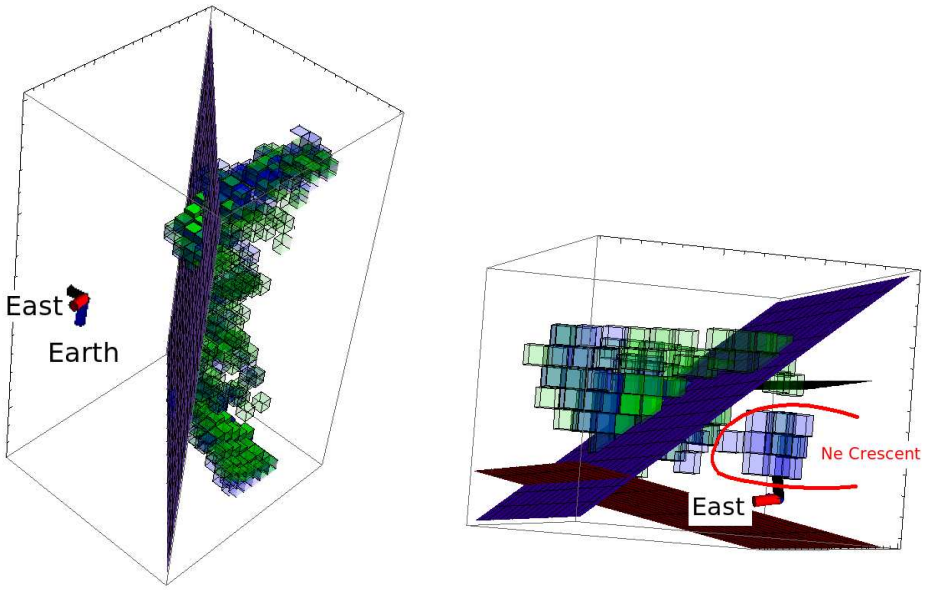

Figure 3.9: 3D plot of the the 25.9μm [O IV] line (blue) and 34.8μm [Si II] line (green) in the Northeast (left) and Southeast (right) of the remnant along with planes of X-ray emission whose location are indicated in Figure 3.1. The IR ejecta are just behind the front edge of the X-ray shock in the Northeast. The same is true in the Southeast, and we see a substantial amount of Oxygen dominated material where our field of view overlaps with the Ne-crescent detected by Ennis et al. (2006). This is not surprising given that Ne and O come from the same nucleosynthetic layer.

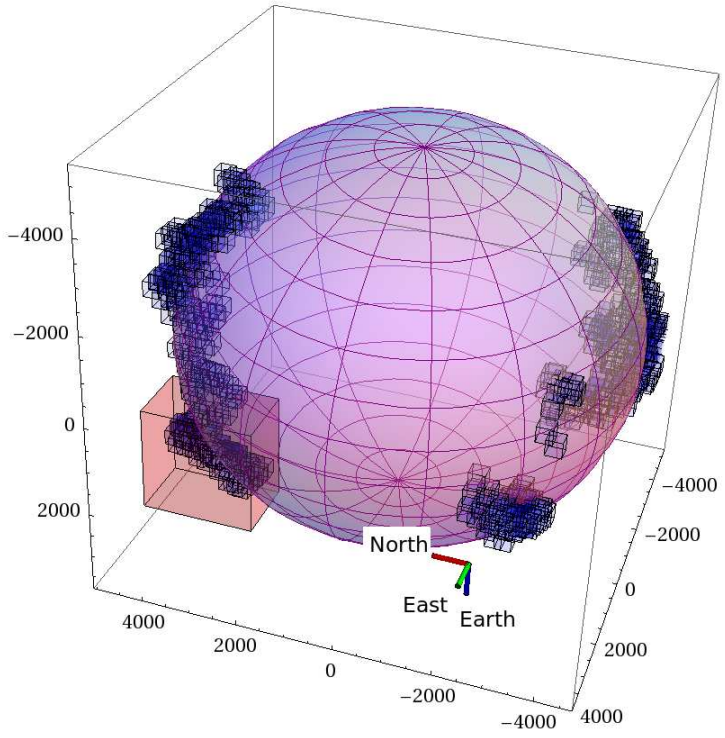

Figure 3.10: 3D plot of ejecta from all regions and the best fit ellipsoid. The units of the axes are km s^{-1}. The ellipsoid is a sphere to within 7%. The zoomed in region in Figure 3.12 is indicated.

3.3.5 Corrugation

Although the brightest ejecta lie near a spherical surface, the ejecta appear to be corrugated about that surface. In fact, the residuals from our best fit surface are dominated by systematic $\sim$250 km s^{-1} corrugations about the surface rather than random small-scale fluctuations. This is most clearly seen in the Southwest region, as shown in Figure 3.11. We find that the average wavelength of the corrugation is $\sim 24''$ and the amplitude is $\sim 8''$ about the best fit surface. We further address the issue of corrugation in the next sections by looking at radial plot of the net intensity of the ejecta.

3.3.6 Separation of Nucleosynthetic Layers

We plot the the brightest [Si II] and [O IV] ejecta, which come from different nucleosynthetic layers, for the Southwest and Northeast in Figures 3.4 and 3.5. There is clearly some separation between these layers in some directions. We show a closeup of one such region in Figure 3.12, where the layers are separated by a few hundred km s^{-1} (corresponding to $\sim 5''$or $\sim$0.1 pc). The location of this region is shown in Figure 3.10.

In the SE, we observe a clump of O rich ejecta with almost no corresponding Si emission. We address this interesting region in more depth in §3.4.2.

We further examine and quantify the separation between layers by plotting the intensity of the emission as a function of three-dimensional radius for all intensities of ejecta for both O and Si in the Southwest. Since Doppler velocity and spatial coordinates are equivalent and we want to determine the velocity separation between nucleosynthetic layers, we converted all our spatial coordinates into velocity units in order to determine the 3 dimensional velocity from the center of expansion found in §3.3.3. This was accomplished by using the arcseconds to km s^{-1} ratio determined by DeLaney et al. (2010). We then plotted the line flux as a function of 3D velocity by binning the emission in 200 km s^{-1} increments.

Because we expect the behavior of the layers to vary as a function of direction, we created plots for many different lines of sight. For each plot we only plotted emission from a solid angle $\pi/12$ steradians wide. Our initial beam was centered $\pi/8$ radians above the plane of the sky and is wide enough to include the entire width of the region, and then incremented by $\pi/12$ radians downward for subsequent lines of sight.

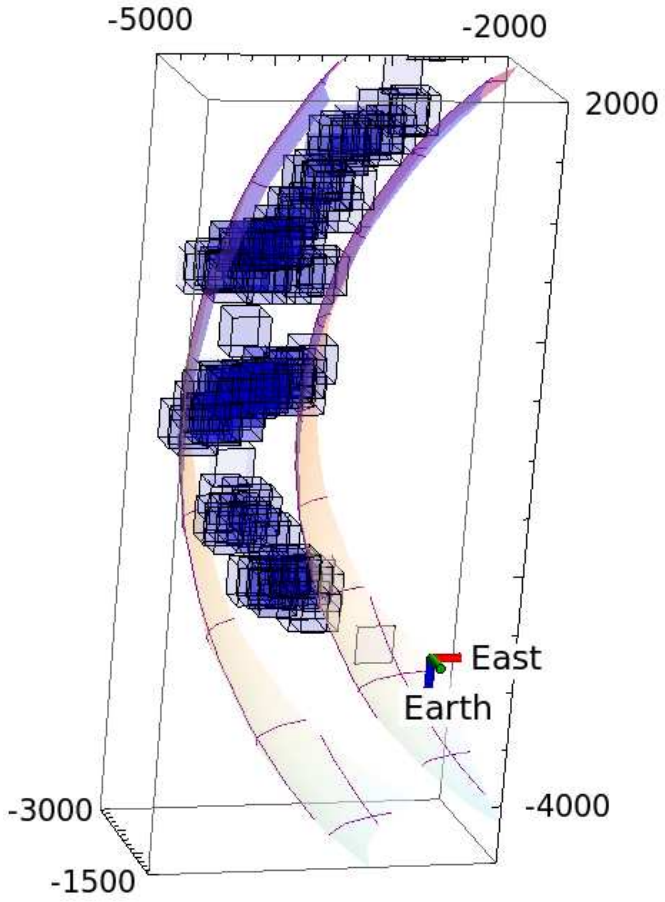

Figure 3.11: 3D plot of the 34.8μm [O IV] line in the Southwest of the remnant. The units of the axes are km s^{-1}. Two ellipsoids with radii 250 km s^{-1} greater than and less than the best fit ellipsoid are also plotted. Although the shell in this region is only $\sim$200 km s^{-1} thick along any single line of sight, the overall velocity of the components systematically varies by $\sim$250 km s^{-1} both above and below the best fit ellipsoid.

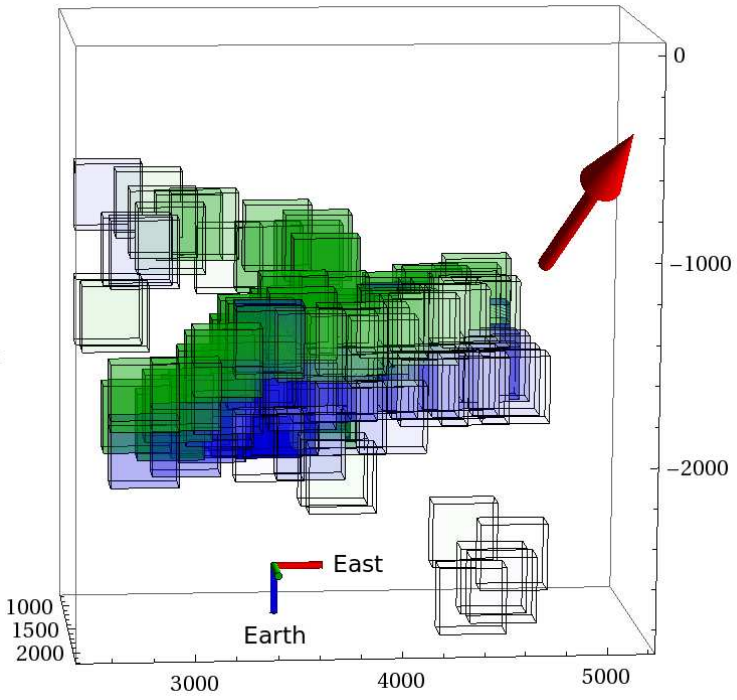

Figure 3.12: 3D plot of the the 25.9μm [O IV] line (blue) and 34.8μm [Si II] line (green) in a select region of the Northeast whose location is indicated in Figure 3.10. The units of the axes are km s^{-1}. The red arrow points to the center of the remnant. We detect clear separation between the O and Si layers along this line of sight.

We show the flux vs. 3D velocity plots for the Southwest in Figure 3.13. The average radial distance of the O with respect to Si varies significantly between locations. Along some lines of sight, they overlap to within one 2″ bin. In different lines of sight, the O peak is at a velocity up to ∼500 km s^{-1} greater than the Si. And along yet other lines of sight, the Si and O peak at roughly the same velocity, but much of the O still is at larger radii than the Si.

Furthermore, the peak velocity of both the Si and O changes as a function of direction from ∼4400 km s^{-1} to ∼5200 km s^{-1}. This is consistent with corrugation in the velocities of the ejecta along different directions.

The velocity width averaged over the solid angle of the Si and O ejecta in the previous section are physical widths, and not just instrumental effects. We find that, to first order, the FWHMs are all ∼1000 km s^{-1} for both Si and O. The velocity uncertainty in our bins is roughly 130 km s^{-1} (since we have an uncertainty of roughly 65 km s^{-1} in each direction) and the bins are 200 km s^{-1} wide.

We note that the velocity width of the peaks is much larger than the velocity width for any given line of sight determined in §3.3.1. The velocity widths of the peaks is dominated by averaging the 3D velocities over the entire solid angle and is not necessarily indicative of the velocity spread over any single line of sight.

3.3.7 Faint Ejecta

Although we dealt mostly with bright ejecta that are found to lie on a distinct spherical structure in the previous sections, there are weaker ejecta which lie interior to this bright shell, especially in the NE region. On average, these ejecta are ∼10% as bright as the ejecta on the shock. We plot these ejecta along with the bright material in Figure 3.14. We note that nearly all the dim ejecta lie interior to the bright ejecta.

3.4 Discussion

3.4.1 Supernova Explosion Physics

3D maps of different nucleosynthetic layers in Cas A provide a unique opportunity to test and constrain the various models. Our observations focus on the layers that were

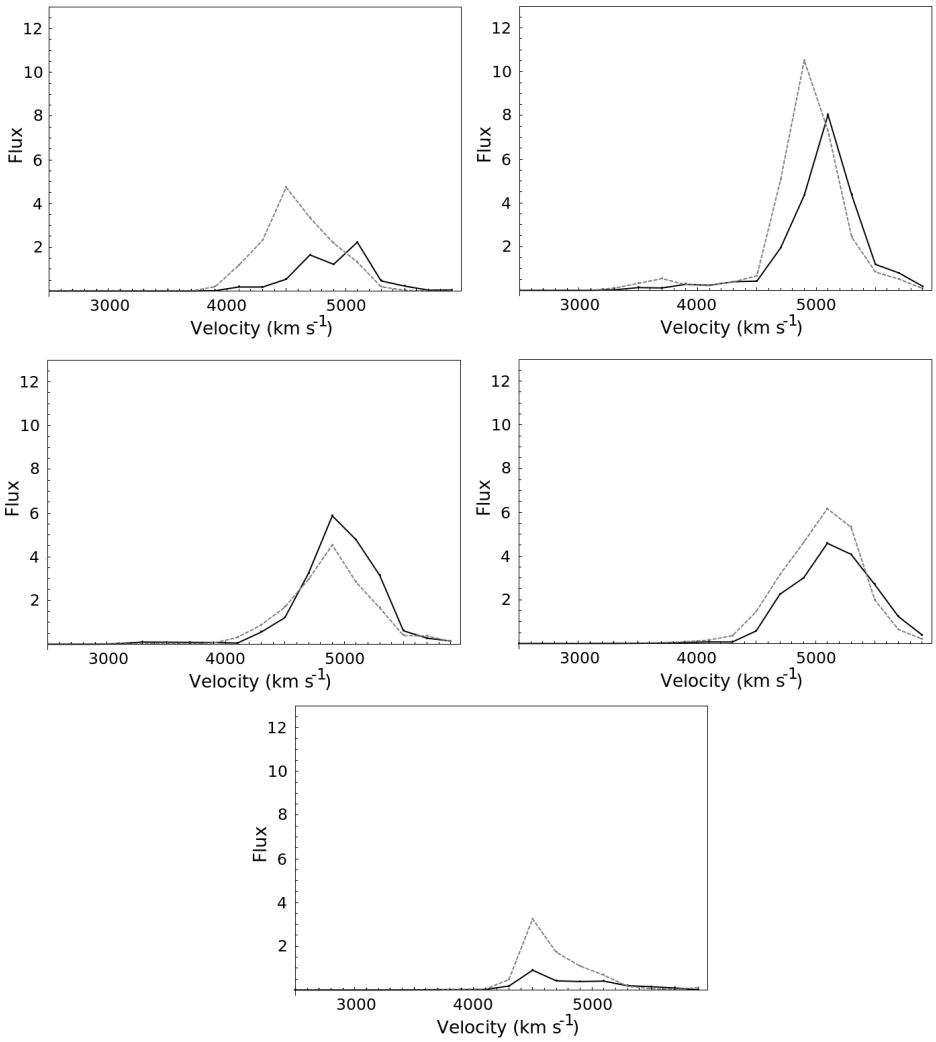

Figure 3.13: Flux vs. radius plot for the Southwest region. The O (dashed) and Si (solid) distributions overlap along some lines of sight, but are offset by up to ∼500 km s^{-1} along others. The peak velocity of the O line and the Si line also vary from about 4400 km s^{-1} to 5200 km s^{-1} depending on the line of sight. This is a clear signature of corrugation. The full-width-half-max of the distributions is ∼1000 km s^{-1} along all lines of sight.

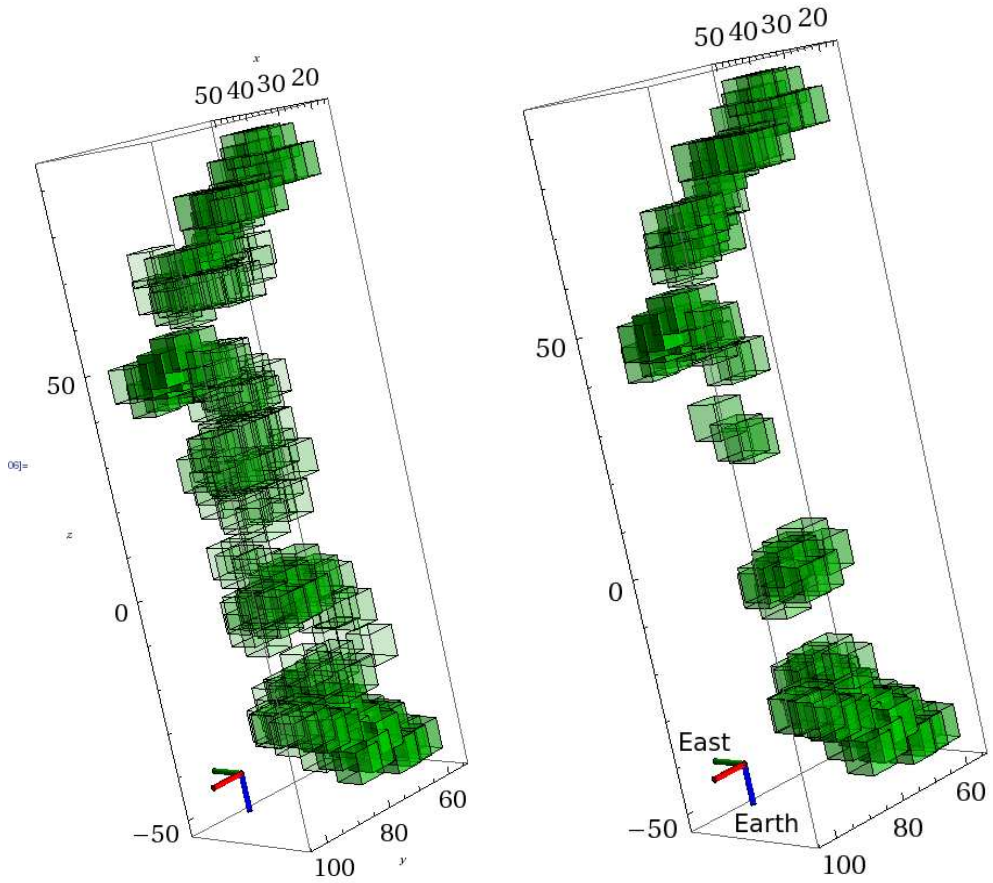

Figure 3.14: 3D plot of all ejecta with at least 10% the flux of the brightest Doppler component (left) and all ejecta with at least 25% the flux of the brightest doppler component (right) . The units on the axes are arcseconds from the center of expansion of the remnant. The dimmer ejecta lie interior to the bright shell formed by the brightest ejecta, indicating that it may not yet have encountered the reverse shock.

initially near the core of the star, where the supernova explosion begins - the Fe/Ni core, the Si/S layer immediately above the core, and the O/Ne layer above the Si/S. We can observe the post-explosion geometry and velocity profile of the different layers. Some models predict that Si and O will be ejected at nearly the same velocity (e.g. Kifonidis et al. 2006), while others predict that they will be ejected at velocities that differ by $\geq$500 km s^{-1} (e.g. Joggerst et al. 2009).

Along many lines of sight, our results are consistent with the models of Kifonidis et al. (2006) and the 25M$_\odot$ models of Joggerst et al. (2009) - we see little difference between the peak velocities of O and Si. However, along other lines of sight, we find that the O and Si peaks are offset by hundreds of km s^{-1} which is inconsistent with above models, but is consistent with the results of the 15M$_\odot$ models of (Joggerst et al. 2009). However, even though this 15M$_\odot$ model produces a reasonable separation between O and Si, it predicts that the velocity width of O will be nearly twice that of Si, while we observe that both layers have roughly the same width along all lines of sight. Furthermore, the model predicts overall velocities of $<$2000 km s^{-1}, which is only half of what we observe. Put together, available models can reproduce most of the various behaviors that we observe, but no single model, so far, can reproduce observed velocity structure of the nucleosynthetic layers of the Cas A supernova explosion.

3.4.2 The Southeast

Ennis et al. (2006) found a Neon "crescent" of ejecta in the Southeast and Northeast of Cas A where Neon was seen in the IR, but little Si was detected in the IR or X-ray. Our Southeast region overlaps slightly with the Neon crescent. Most of the IR emission in this region consists of overlapping Si and O immediately behind the X-ray ejecta. However, in the Neon crescent, we see only O emission that is more than an order of magnitude stronger than Si emission as shown in Figure 3.9. This is consistent with Ennis et al. (2006) and Smith et al. (2009) since Neon and O come from the same nucleosynthetic layer. The most likely explanation for this Neon/O crescent is that the Neon and O are currently encountering the reverse shock and therefore becoming brighter as they are compressed, while the Si has yet to encounter the reverse shock. It is therefore not bright enough to be detected in the IR since it is not yet at high enough densities, and cannot be detected in the X-ray because it is not in the correct ionization

state.

3.4.3 Geometry

We observe that the center of expansion is offset from the center of the remnant by ∼810 km/s along our line of sight. This is consistent with previous results from 3D reconstructions in the optical (Reed et al. 1995) and the IR (DeLaney et al. 2010; Isensee et al. 2010). There are three major possible sources for the cause of this offset - asymmetries in the circumstellar environment, movement by the progenitor star, and the supernova explosion itself.

Reed et al. (1995) speculated that this offset was due to asymmetries in the pre-supernova circumstellar environment. Isensee et al. (2010), using one patch toward the center of the remnant, argue that this cannot be the case since the ejecta interior to the reverse shock show the same velocity asymmetry, despite the fact that they are unaffected by the circumstellar material. The interior ejecta are expanding into a bubble that has been cleared of any circumstellar material by the shocks associated with the supernova explosion. Since our new results, which span the Bright Ring, are consistent with those of Isensee et al. (2010), the velocity offset is not specific to the central regions of Cas A, but applies to the entire remnant.

In principle, the velocity offset could be caused by progenitor motion, but the observed 810 km s^{-1} offset is much too large a velocity for a star. Neutron stars may have velocities >500 km s^{-1} (e.g. Satterfield et al. 2011), but such large velocities are the result of "kicks" during the supernova explosion, which are caused by asymmetries in the supernova explosion itself or a binary companion (Shklovskii 1969; Chatterjee et al. 2005).

Therefore, the observed offset it most likely caused by asymmetries in the supernova itself. A likely culprit is asymmetries formed in the first ∼100 milliseconds as seen in the models of Burrows et al. (2007) and the SASI models of Blondin et al. (2003). Both of these instabilities allow the initially spherically symmetric forward shock to become highly asymmetric in just a few crossing times. These instabilities arise due to the response of the post shock pressure to changes in the shock radius. If the pressure in one region becomes slightly higher than the surroundings, it will push the shock outward. The preshock pressure drops with increasing radius, which leads to smaller pressures

behind the forward shock due to the outward shock displacement. If the postshock pressure radial profile is steeper than the preshock pressure profile, a standing acoustic wave is produced by the positive feedback loop. Ejecta can "slosh" between the standing shocks, resulting in substantial asymmetries (Blondin et al. 2003). Presumably, the ejecta will maintain this asymmetry as they expand outward, resulting in a low-order asymmetry that is not necessarily centered on the location of the progenitor star. Note that although the shock may initially be asymmetric, it will gradually become spherical over time (Bisnovatyi-Kogan & Blinnikov 1982), producing the nearly spherical surface that we observe today.

3.4.4 Faint Ejecta

The faint ejecta seen interior to the bright ejecta on the nearly spherical shell are likely ejecta that have yet to encounter the reverse shock. We expect to observe both [Si II] and [O IV] even if they are not yet shocked because they will be photoionized by energetic UV and X-ray photons from the reverse shock. Such ejecta were previously detected in the center of the remnant and interior to the reverse shock by DeLaney et al. (2010), Smith et al. (2009), and Isensee et al. (2010). The flux of the ejecta appears to be roughly an order of magnitude less than that of nearby material which has been shocked. This is consistent with what is expected from a strong shock - a compression factor of about 4 is expected for a classic strong shock, which would cause a rise in emissivity of a factor of 16.

We note that the interior ejecta in the center of the remnant (see Figure 3.1) discussed extensively in Isensee et al. (2010) are much brighter than the interior ejecta in all the regions shown here. The most obvious explanation for this is that they are at a higher density, since the emissivity of the ejecta varies as the square of the density. This difference in density is probably caused by geometric effects. The central material from the remnant is traveling at roughly half the velocity as the material currently encountering the reverse shock in the plane of the sky DeLaney et al. (2010). If the ejecta are expanding adiabatically and were initially ejected at roughly the same density, the material in the plane of the sky would be denser by a factor of 4 than material at the center of the remnant. Therefore, we would expect the emissivity of interior, central ejecta to be roughly 16 times that of material in the plane of the sky that is interior to

the reverse shock. This is roughly what we observe - interior material in these regions have an average flux of $\sim$300 MJy sr^{-1}, while material in the center of the remnant have fluxes around 4000 MJy sr^{-1} (Isensee et al. 2010).

3.4.5 Corrugation

Corrugation has been previous observed in several supernova remnants, including SN1006 (Winkler & Long 1997) and the Cygnus Loop (Raymond 2003). There are several possible explanations for this corrugation. If the shock is radiative, the ripples could be caused by the thermal instability (Bertschinger 1986) or the thin shell instability (Vishniac 1983). The thermal instability is especially relevant for high speed (>150 km s^{-1}), high temperature (T>10^5 K) shocks where the sound speed crossing time greatly exceeds the cooling time. This "instability" is actually an overstability that results from the high radiative cooling rate. The thin shell instability is another overstability. In this scenario, the ram pressure and thermal pressure are misaligned, causing ripples in the initially smooth distribution of ejecta. Neither of these explanations is likely for Cas A since the shocks are not highly radiative.

Another possibility is that the ripples are caused by inhomogeneities in the ejecta encountering the shock. This inhomogeneity could be caused by Rayleigh-Taylor filaments created at the contact discontinuity between the ejecta and the ISM as the remnant enters its Sedov-Taylor phase (Wang & Chevalier 2001). While this is a likely explanation for the corrugation observed in SN1006 (Long et al. 2003), it is not likely in Cas A since the ISM has already been swept away by the time the ejecta encounter the reverse shock.

A final explanation is that the corrugation is caused by density variations in the ejecta itself (Raymond 2003). In this model, dense ejecta encountering the reverse shock would be slowed less than less dense clumps of ejecta. Raymond (2003) argues that this instability is the most likely cause for the corrugation in the Cygnus Loop, where the density variations may have been caused by ISM turbulence.

Regardless of the mechanism, there is also a question of where the corrugation occurs. The observed ejecta have encountered several shocks - the forward shock during the supernova explosion itself, a reverse shock during the supernova, and most recently, a larger scale reverse shock in the supernova remnant (Isensee et al. 2010). Which shock

encounter creates the observed corrugation?

Most studies expect corrugation at the second, larger forward or reverse shocks associated with the remnant. However, we conclude that the most likely location for the corrugation is during one of the two shocks that the ejecta encounter during the supernova explosion itself. Previous studies find little evidence for deceleration of IR ejecta after the explosion, including recently shocked ejecta (DeLaney et al. 2010). Our data are also inconsistent with recent deceleration of the ejecta. If the ejecta were suddenly decelerated, the ejecta would be closer to the plane of they sky in our models due to the reduction in Doppler velocity, forming a flattened surface. However, we do not observe this pattern in the shocked ejecta - we still see a nearly perfect sphere. In other words, if the corrugation were being caused at the reverse shock, the ejecta would need to be decelerated by at least several hundred kilometers per second in order to create the observed corrugation since being shocked. This effect would be easily visible with our Doppler reconstruction of the global geometry, but is not observed. Thus, the corrugation must occur during the supernova explosion itself, perhaps at the initial forward or explosion reverse shock.

3.5 Conclusions

We create a 3D model of shocked ejecta of Cas A in select regions at unprecedented spectral resolution using IR ionic lines. We confirm previous studies that indicate that the remnant is offset by $\sim$800 km s^{-1} along our line of sight. We find evidence for velocity separation between the O and Si layers along some, but not all, lines of sight. We measure the velocity width of these layers roughly 250 km s^{-1} thick for a single line of sight, although the ejecta are often in bands that are $\sim$1000 km s^{-1} thick averaged over several nearby lines of sight due to corrugation. We find evidence for corrugation in some regions of the remnant, and speculate that the corrugation was caused during the explosion itself rather than hundreds of years later. We use our observations of Si and O velocities to begin constraining models of supernova explosions, and to motivate future models to explore velocity profiles as a function of azimuth.

Chapter 4

The X-ray Evolution of Shocked Ejecta

Note: A modified version of this article has been submitted to the Astrophysical Journal: Isensee, K., Rudnick, L., DeLaney, T.A. 2011, ApJ in preparation

We present a detailed multi-epoch X-ray analysis of the supernova remnant Cassiopeia A using *Chandra X-ray Observatory* exposures from 2000, 2002, and 2004. We identify the most recently shocked X-ray ejecta with ionization timescales of $\sim$1x10^{10} cm^{-3} s, nearly an order of magnitude smaller than previously identified shocked ejecta. These ejecta are then used to determine if the original nucleosynthetic layers of the star are arriving at Cas A's reverse shock at different times. We use recent collisional ionization models that allow us to correlate observed changes in spectrum with a rough estimate of when the Mg and Fe layers reached the reverse shock. We find several regions that have a signature consistent with a separation of $\sim$200 km s^{-1} between layers, although we find that most regions show no sign of separation greater than 65 km s^{-1}. This method is able to detect substantially smaller separations between layers than earlier X-ray techniques. We test various supernova explosion models against our observations by comparing our observed velocity separation between layers to predictions from the models. We conclude that any mixing between nucleosynthetic layers is most likely caused by Rayleigh-Taylor filamentation and not partial explosive nucleosynthesis

in the layers. Our observations of spectral changes provide feedback for future models which will address important physical issues such as the role of cosmic ray production at a supernova remnant's reverse shock.

4.1 Introduction

Emission at most energies in Cas A is dominated by a "Bright Ring" with a radius of $\sim 120''$ (or $\sim$2 pc at Cas A's estimated distance) and a thickness of $30''$ (e.g. Chevalier & Kirschner 1978). This Bright Ring is formed when ejecta encounter Cas A's reverse shock and are heated and ionized. The result is a strongly emitting plasma with a thermal X-ray spectrum dominated by emission lines. This plasma is observed to be clumpy and irregular. This reflects the inhomogeneous nature of the supernova ejecta, and was probably caused by radiative cooling instabilities and the possible turbulent mixing of different chemical layers of the progenitor star during the supernova explosion (Hughes et al. 2000; Hwang et al. 2000). The ejecta are rich in O, Si, S, Ne, Ar, O, Mg, and Fe (Chevalier & Kirshner 1978; Douvian et al. 1999, Hughes et al. 2000; Willingale et al. 2003; Hwang & Laming (2003); Laming & Hwang (2003); Morse et al. 2004). At a radius of $\sim 150''$ there is a fainter ring consisting of X-Ray filaments associated with the interaction of Cas A's forward shock and the circumstellar medium (Gotthelf et al 2001; DeLaney & Rudnick 2003).

In most regions, Cas A's reverse shock has only been roughly located by observations of a sharp rise in azimuthal averages of X-Ray emission (Gotthelf et al. 2001). In a few regions the reverse shock's location has been pinpointed to arcsecond accuracy through the use of high-resolution Hubble Space Telescope images - evidence for ejecta recently encountering the reverse shock are observed as a rise in emission and increase in ionization timescale as the region is shocked, heated, and decelerated (Fesen et al. 2001; Morse et al. 2004). Eventually the ejecta cool, leading to an observable decline in emission (Patnaude & Fesen 2007).

4.1.1 Supernova Explosion Models

The basic nature of supernova explosions is one of the great outstanding problems in modern theoretical astrophysics. Models predict different velocity profiles across concentric nucleosynthesis layers when the star explodes: for example, the models of (Joggerst et al. 2009) predict a velocity separation of $\geq$100 km s^{-3} between several neighboring layers, while (Kifonidis et al. 2006) predict minimal velocity separation between neighboring layers. These models generally incorporate different physics - for example, Kifonidis et al. (2006) models a blue supergiant with rotation, while Joggerst et al. (2009) models a red supergiant without rotation. Observations of supernova remnants are critical for testing the various supernova explosion models since the velocity profile should be preserved for hundreds of years after the supernova explosion due to the lack of observed deceleration of ejecta (DeLaney 2004).

An expanding debris field with a velocity distribution will show spatial separation over time assuming that it does not experience any acceleration. Velocity differences of $\sim$100 km s^{-1} are observed along some lines of sight between nucleosynthetic layers in Cas A (Isensee et al. 2010). This would imply a spatial separation of $\sim10^{17}$cm. Such a spatial separation should be observable since, at Cas A's distance, $1''$ corresponds to $\sim10^{16}$cm. Note that we cannot observe any *initial* spatial separation between layers since simulations predict that the relevant nucleosynthetic layers will be 10^{12}-10^{14} cm thick prior to the explosion (e.g. Joggerst et al. 2009), which makes them much too small to spatially resolve.

As discussed in previous chapters, a variety of observational studies have provided different results concerning the relative velocity of the nucleosynthetic layers in supernova remnants. Isensee et al. (2010) find that along most lines of sight toward the center of the remnant, Si and O were ejected at the same velocity (that is, with a velocity separation of $<$65 km s^{-1}, the instrumental limit of the observations). These results from Cas A match those from other core collapse supernovae. For example, (Flanagan et al. 2004) argue that many different nucleosynthetic layers were ejected at the same velocity in the supernova remnant 1E 0102.2-7219. They detect Mg XI and O VIII situated between Ne XI and Ne X emission. This pattern of emission can be explained if Ne, O, and Mg reached the reverse shock at the same time because it will take different amounts of time for each element to reach the various detectable ionization states,

resulting in a radial distribution of different ions.

However, some studies argue for a separation between nucleosynthetic layers. Hughes et al. (2000) observed Fe at larger radii than Si and O emission in the Southeast and Northwest of Cas A. This might be evidence of the overturn and velocity separation between nucleosynthetic layers, although DeLaney et al. (2010) argue that the other layers are in front of the Fe, but just not easily visible. However, the DeLaney et al. (2010) model still requires a spatial separation between the Fe and Si/S layers, with the Fe traveling at a different velocity than the Si/S and O layers of ejecta so that it encounters the reverse shock at a different time. Fesen et al. (2006) also report a spatial separation between N and O optical knots in a few select parts of the remnant. Finally, IR observations detect "crescents" of Ne emission that are uncorrelated with strong Si emission, indicating that the O/Ne layer of the star is currently interacting with the reverse shock, but the Si/S layer is not (Ennis et al. 2006; Smith et al. 2009).

Recent high resolution 3D maps of the various layers in the IR using Spitzer show velocity separations between nucleosynthetic layers in some directions, but identical velocities between the layers in other directions (Isensee et al. 2010). O and Si ejecta that are interior to the reverse shock were observed to be at the same spatial locations in most observed directions, with a velocity separation of $<$65 km s^{-1}. However, in some directions O and Si ejecta were observed to be separated by hundreds of km s^{-1}. This separation does not correspond to the layers maintaining their order from the initial onion skin layering, or a simple overturn, because the O ejecta were observed traveling *both* more quickly and more slowly than Si in those directions.

Taken together, it appears that there is a substantial amount of spatial variability in the degree of velocity separation between the nucleosynthetic layers for both the light layers that originated near the surface of the star as well as the denser interior layers.

4.1.2 Shock Models

Cas A also allows us to address current issues in shock physics, such as the roles of cosmic ray acceleration and diffusive shock acceleration in the evolution of a supernova remnant (e.g. Bell 1978) and the efficiency of energy transfer between the ions and electrons as ejecta encounter the reverse shock. Cosmic ray acceleration results in substantial differences in shock compression ratios, and both cosmic ray acceleration and difference

in energy transfer between ions and electrons affect postshock plasma temperatures and ionization states (Patnaude et al. 2009; Borkowski et al. 2001; Jones & Ellison 1991; Berezhko & Ellison 1999). These issues are usually only addressed at a supernova remnant's forward shock. However, it is also possible for cosmic ray acceleration to happen at the remant's reverse shock (Ellison et al. 2005; Anderson & Rudnick 1995). Therefore, it is important to understand the physics of the encounter of the ejecta with the reverse shock in young supernova remnants, where heating and ionization create multi-temperature, non-equilibrium plasmas with bright infrared, optical and X-ray line and continuum emission.

Fermi-LAT MeV gamma ray observation found evidence for cosmic ray acceleration in several supernova remnants, including Cas A (Abdo et al. 2010). However, Fermi-LAT does not have the necessary spatial resolution to differentiate between cosmic ray acceleration happening at the reverse or forward shocks, and the efficiency of cosmic ray production is only crudely constrained.

Patnaude & Fesen (2007) have used broadband (0.3-10 keV) Chandra images to spot changes over 2 year baselines in small, compact X-ray knots located on Cas A's Bright Ring. They find a handful of knots that are becoming brighter over time, indicating a recent encounter with the remnant's reverse shock. Substantial changes ($\sim$20%) in both electron temperature and ionization timescale were reported for these knots. However, there are currently no models that allow one to use these observations to constrain cosmic ray production.

In this paper, we present an analysis of *Chandra* ACIS data from 3 epochs. We concentrate on the temporal variability in spectra of ejecta, and use the variability to address the velocity separation of the nucleosynthetic layers. This method is capable of picking up velocity differences of a few hundred km s^{-1} between the layers. This is often a superior technique to simply looking for spatial separation between nucleosynthetic layers because it is not confused by projection effects. Furthermore, we identify knots that were more recently shocked than similar knots identified in previous studies, and whose variability could be used as a test for shock acceleration models. In §4.2 we present the Chandra observations and discuss the data reduction. In §4.3 we present the results of our analysis and we interpret those results in §4.4. §4.5 contains a summary of our conclusions.

4.2 Data Analysis

4.2.1 Observations

Cas A was observed in GRADED mode with the ACIS-S3 chip as part of the *Chandra* Guest Program for 50 kiloseconds in January of 2000 and February of 2002 (for details of data reduction see Hwang et al. 2000; Gotthelf et al. 2001; DeLaney & Rudnick 2003). It was also observed for 1 megasecond in February of 2004 (see Hwang et al. 2004). We reprocessed these data using version 3.4 of the Chandra Calibration Database and also generated detector response matrices for spectral fitting as discussed below.

We are attempting to observe small changes in brightness and spectra in supernova ejecta. However, *Chandra*'s azimuthally varying point spread function can make comparisons between epochs difficult. The 2000 and 2002 epochs were taken at nearly identical spacecraft roll angles in order to minimize this issue. A 50 ks subset of the 1 megasecond 2004 observation was also taken at an identical roll angle to the previous epochs. Therefore, we use only the appropriate 50 kilosecond subset of the 1 megasecond observation.

There are substantial energy dependent issues primarily due to dithering at the node boundaries that result in spurious detections of spectral changes between the epochs. In order to minimize this effect, we divided the event file from each epoch into five energy bands (0.3-2 keV, 2-4 keV, 4-6 keV, 6-8 keV, and 8-10 keV) and reprocessed each band separately in order to improve our handling of any energy dependent effects across the node boundaries. Even after the cuts were added back together to reconstruct the original image, there are still substantial issues at the node boundaries, so we blanked out those regions of the remnant when appropriate.

Great care was taken to assure that any observed spectral changes between the epochs were not due to calibration issues. This is especially important because our observations were made in GRADED mode, as opposed to the much more commonly used and better understood FAINT and VFAINT modes. In order to test whether or not calibration issues would cause spurious detections of spectral change, we extracted spectra from the 2004 and 2000 data sets from an area whose spectrum should not change by a substantial amount - the circumstellar material interacting with the forward shock (the extraction region for the circumstellar material is shown in Figure 4.1). We then

subtracted each 2000 energy bin from each 2004 energy bin and plotted the "difference spectrum" in Figure 4.2. We also divided each 2004 energy bin by the corresponding 2000 energy bin and plotted the "ratio spectrum" in the same figure. These figures show that the calibration between these control regions is good to within 7%.

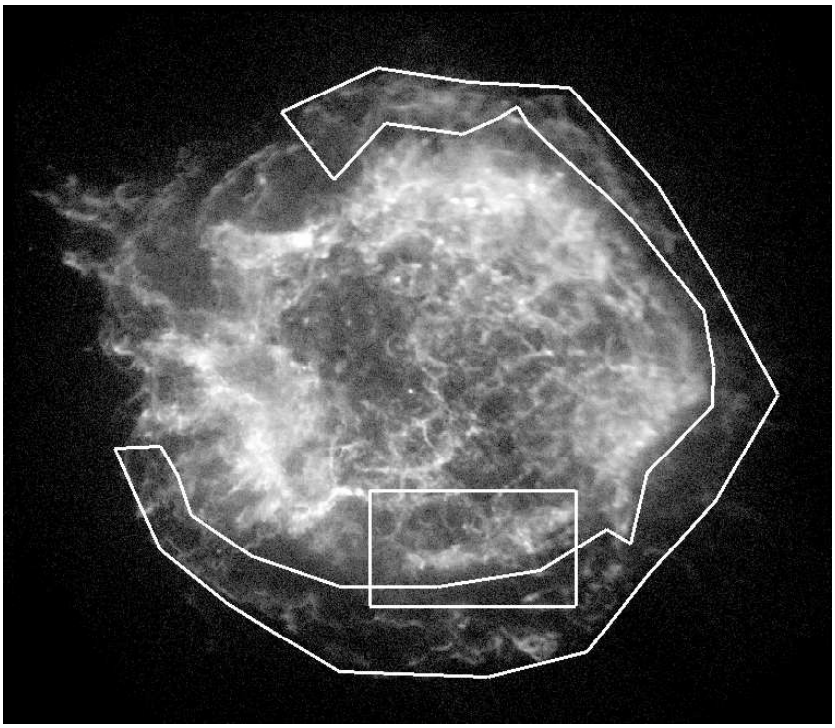

Figure 4.1: 0.3-10 keV Chandra image of Cas A from the 2000 data set. The region from which we extract the 2000 and 2004 circumstellar medium spectra is indicated. The box indicates the zoomed in region where we observe spatial separation between the Mg and Si layers in Figure 4.13.

4.2.2 Spectral Fitting

Much of the work described below relies on spectral fitting. Backgrounds were subtracted from all spectra by selecting regions close to the region of interest. This method is preferred to using ACIS Blank-Sky images since the dominant source of background counts from our observations are scattered X-Rays from the remnant itself. The background and source spectra were binned so that there are at least 15 counts per detector channel.

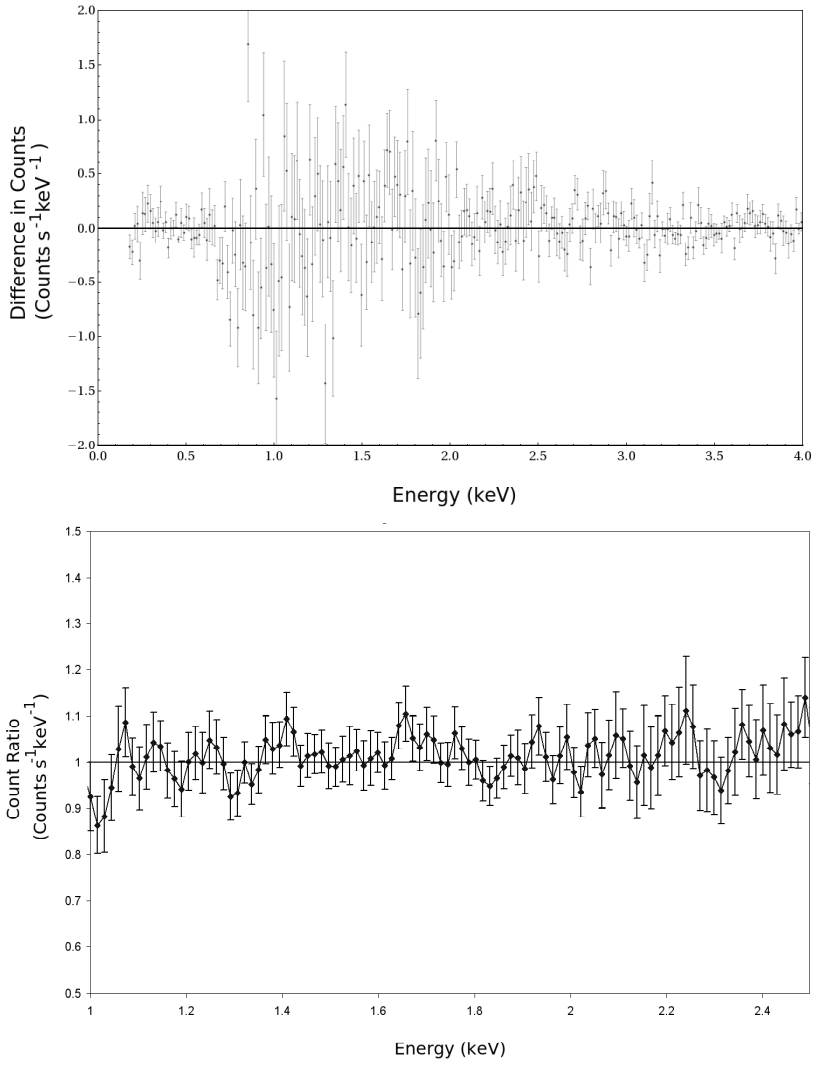

Figure 4.2: Difference spectrum (top) and ratio spectrum (bottom) from 2004/2000 circumstellar medium test region. The calibration of the images between 1 and 2.5 keV is good within 7%.

We model the spectra of the ejecta by using a single temperature, single ionization timescale nonequilibrium ionization model modified by interstellar hydrogen absorption. This was done by using the VNEI model modified by the PHABS model as implemented in XSPEC version 12.4. Previous studies have extensively argued for the appropriateness of this model for fitting the spectra of young supernova remnants like Cas A (e.g. Borkowski et al. 2001; Hwang & Laming 2009). This model fits spectra from supernova remnants such as Cas A quite well - typical reduced chi-squareds from our fits are $\leq$2.0.

Similar to previous authors (e.g. Hwang & Laming 2009), we assume that the continuum comes primarily from ionized O and heavier elements, with a negligible contribution from lighter elements. While it is possible to model the continuum with lighter elements, their inclusion has little effect on the derived parameters, so we set their abundances to 0. Given the large bulk velocities of the ejecta (e.g. Markert et al. 1983) we also allow for a Doppler shift of the spectral lines. This allows us to derive the electron temperatures, ionization timescales, and elemental abundances for modeled ejecta.

4.2.3 Line Identification

We identify the ionic emission lines responsible for observed changes at about 1.05 and 1.35 keV. Identification of these lines can be difficult since there are many potential Ne, O, Ni, Mg, and Fe lines near these energies. We used ATOMDB[1] to find a list of lines near the relevant energies, along with estimates of the relevant line strengths. This model uses several simplifying assumptions in generating its data, including assuming coronal abundances of elements and local thermodynamic equilibrium. These assumptions likely break down for recently shocked supernova ejecta, making line strength estimates unreliable. Therefore, we carefully examined the detailed spectral shapes as described below.

We take a spectrum of the whole remnant and zoom in on lines near 1.05 and 1.35 keV. We note the exact energies for several strong lines on this plot. As shown in Figure 4.3, it is clear that Fe XXII/XXIII and Mg XI are primarily responsible for the lines near 1.05 and 1.35 keV. We cannot differentiate between the 1.053 and 1.056 Fe XXII and Fe XXIII lines since they are too close together in energy.

[1] The online version of this database is available at http://www.atomdb.org/Webguide/webguide.php

We create synthetic spectra near 1.35 keV in order to address the effects of potential contaminating lines. This is done by using the VNEI model modified by PHABS as implemented in XSPEC version 12.4 as discussed in §4.2.2. We model a purely Fe/Ni gas at τ=6x10^{10} and 8x10^{10} cm^{-1} s in Figure 4.4, keeping the electron temperature constant at 1.75 keV. Although the Fe lines near 1.25 keV are getting dimmer as the ionization timescale increases, the blended line peak is moving to higher energies due to the increase in ionization timescale. There is a slight excess of counts near 1.35 keV that could be contaminating our Mg dominated energy cut.

We then modeled a Fe/Ni + Mg/Ne gas where the Mg/Ne and Fe/Ni were at different ionization timescales. We set the temperature of both gasses to 1.75 keV, but the ionization timescale of Mg was set at 8x10^{9} and 1x10^{10} cm^{-1} s while Fe/Ni was set at 6x10^{10} and 8x10^{10} cm^{-1} s. We then subtracted the lower ionization timescale combined models from the higher ionization timescale models in order to create a difference spectrum and compared the model difference spectra for a pure Fe/Ni gas to the difference spectra for a Fe/Ni+Mg/Ne plasma in Figure 4.5. The key difference is the substantial positive residual near 1.35 keV in the model with Mg due to changes in the Mg XI line strengths, while the peak of the residual is at 1.42 keV in the case of a purely Fe/Ni gas. We can therefore conclude that changes at around 1.35 keV are due to Mg XI line strength changes if the increase in line strength peaks at roughly 1.35 keV. Changes that peak at >1.40 keV are likely caused by changes in Fe line strengths.

The details of this modeling change as a function of temperature, redshift, elemental abundance, and ionization timescale differences. However, the qualitative picture does not change - for any reasonable set of parameters, the peak of the change near 1.35 keV will occur at >1.40 keV for a purely Fe/Ni plasma, while it will occur near 1.35 keV once Mg is included.

4.3 Results

4.3.1 Recently Shocked Ejecta

We identify recently shocked knots by looking for rapid changes in their observed line strengths. The largest fractional changes over a fixed time period (4 years in this case) should occur when the ionization timescale is low. Mg XI reaches peak intensity at the

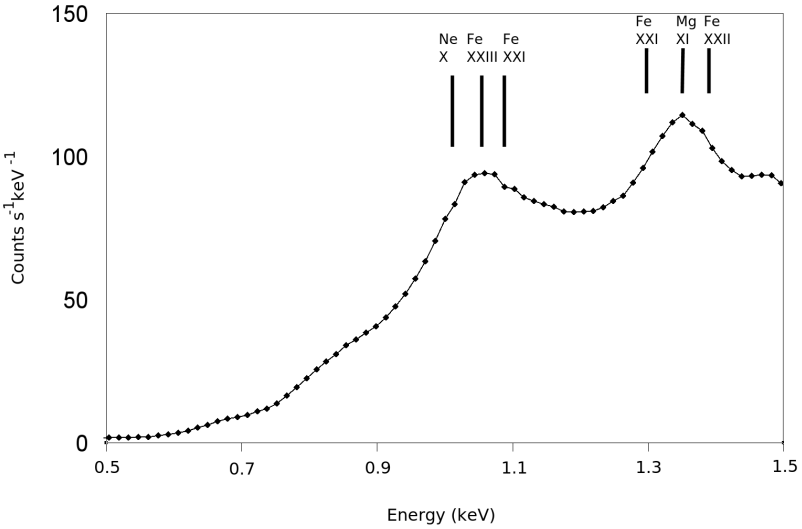

Figure 4.3: Spectrum from relevant energy range for all of Cassiopeia A. The exact energies of several candidate lines are shown. We identify the line near 1.05 keV as Fe XXII/XXIII and the line near 1.35 keV as Mg XI.

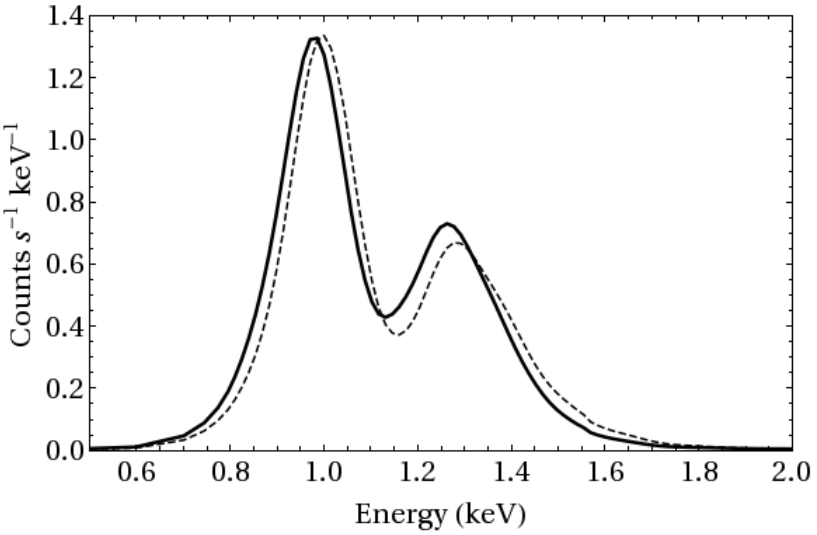

Figure 4.4: Model spectrum of a pure Fe/Ni plasma at τ=6x10^{10} (solid) and 8x10^{10} (dashed) cm^{-3}s. Both models were generated using a VNEI model modified by hydrogen absorption at an electron temperature of 1.75 keV. Note that there is a slight excess of counts at higher ionization timescales at and above 1.4 keV.

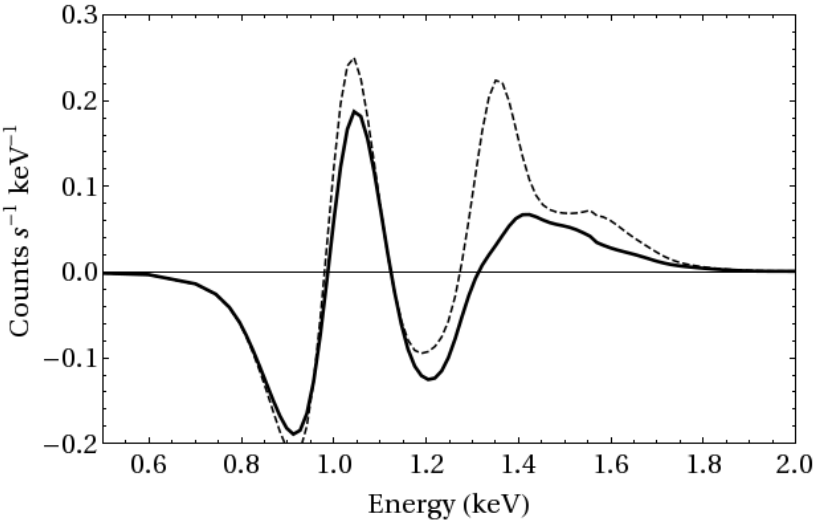

Figure 4.5: Residuals from model spectrum of a purely Fe/Ni plasma (solid) and a Fe/Ni+Mg/Ne plasma (dashed). The Fe/Ni varied from τ=6x10^{10} to 8x10^{10} cm^{-3} s, while the Mg/Ne varied from τ=8x10^{9} to 1x10^{10} cm^{-3} s. Both models were generated using a VNEI model modified by hydrogen absorption at an electron temperature of 1.75 keV. The lower ionization timescale models were subtracted from the higher ionization timescale models. The residual purely Fe/Ni model has an excess that peaks at 1.42 keV, while the residual Fe/Ni+Mg/Ne model peaks at 1.35 keV.

lowest ionization timescale of any of our easily observable lines (Mazzotta et al. 1998). Thus, the regions which show the largest fractional changes in the Mg XI line strength are likely to be those with some of the lowest observable ionization timescales. The location of the Mg XI line is indicated in the spectrum in Figure 4.6.

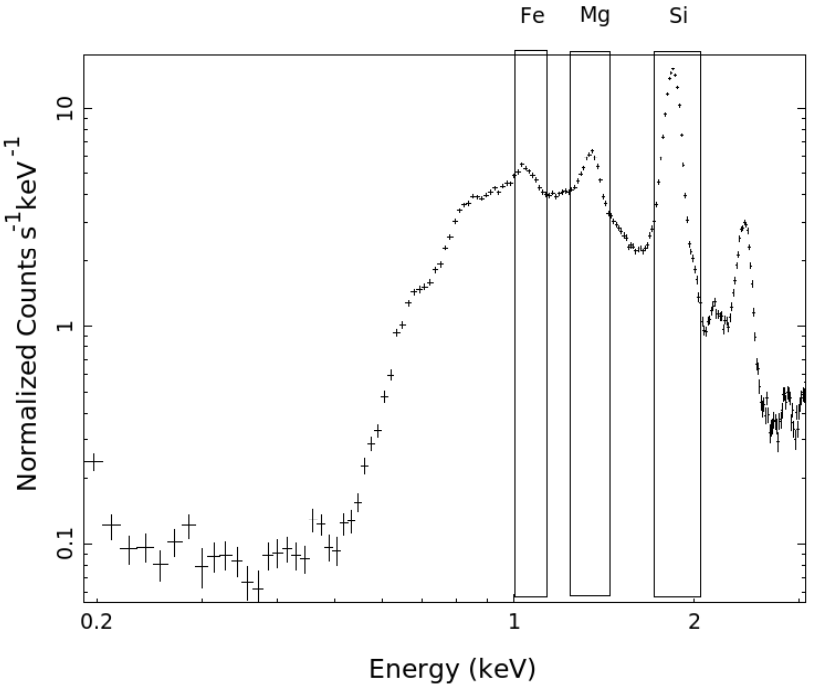

Figure 4.6: Spectrum of Cas A. Relevant emission lines are indicated. The energy bins for our "energy cuts" are indicated by the boxes.

We made "energy cuts" of Cassiopeia A by mapping the counts from select energy ranges. In this case, we made a Mg XI energy cut by mapping counts from 1.31-1.41 keV in both the 2000 and 2004 epochs. We identify the regions with the strongest changes in the Mg XI line by making a ratio map of the Mg energy cuts that have been normalized such that there are an equal number of counts over the whole remnant in both the 2000 and 2004 epochs. We then convolved the map to 5″. We extracted spectra from the 2000, 2002, and 2004 epochs from 6 regions which showed large fractional changes and fit a VNEI spectrum modified by hydrogen absorption as described in §4.2.2 to each spectrum. The results from the spectral fits are shown in Table 4.1.

The typical ionization timescales associated with these knots are often approximately a factor of 5 smaller than those of Patnaude & Fesen (2007), who also identified recently shocked ejecta ($\sim$1x10^{10} vs $\sim$5x10^{10}). This is because Patnaude & Fesen (2007) used the entire Chandra energy band to look for changes. The Si line around 2.0 keV dominates these observations for shocked ejecta (roughly 50% of the total counts), so they are primarily sensitive to changes in the Si lines, which occur at later ionization ages than changes in the O, Mg, and some Fe lines.

Table 4.1: Spectral parameters for 6 recently shocked regions. Typical uncertainties are $\sim$10%

	2000 n_et cm^{-3} s	2000 T keV	2002 n_et cm^{-3} s	2002 T keV	2004 n_et cm^{-3} s	2004 T keV
Region 1	1.12x10^{10}	0.84	1.21x10^{10}	1.4	1.26x10^{10}	1.5
Region 2	1.32x10^{10}	1.3	1.35x10^{10}	1.4	1.55x10^{10}	1.4
Region 3	2.18x10^{10}	1.5	2.20x10^{10}	1.7	2.26x10^{10}	1.8
Region 4	1.02x10^{10}	0.9	1.34x10^{10}	0.9	1.49x10^{10}	1.3
Region 5	3.38x10^{10}	1.4	3.36x10^{10}	1.6	3.48x10^{10}	1.6
Region 6	1.78x10^{10}	1.8	1.84x10^{10}	1.8	1.90x10^{10}	2.0

4.3.2 Ionization Models and Methodology

The primary method we use to identify velocity separation between layers is determining whether or not the spectral lines detected in a knot are consistent with each of the observed elements having the same ionization timescale. Our technique is to observe changes in the line strengths between the 2000 and 2004 epochs. We selected two lines from elements that originated from different nucleosynthetic layers - the 1.35 keV Mg XI and 1.05 keV Fe XXII/XXIII lines (see Figure 4.6). We then compare the observed changes in the strength of the lines to predictions of ionization state as a function of ionization timescale from a simple ionization state model (Mazzotta et al. 1998). We show the expected ion fraction as a function of ionization timescale in Figure 4.7 for the relevant ions of Fe and Mg.

The ionization state model is based on the total ionization rates for each element as determined by the coefficients for the rates of collisional and autoexcitation ionization for a plasma at a given temperature. These coefficients were calculated with an IDL

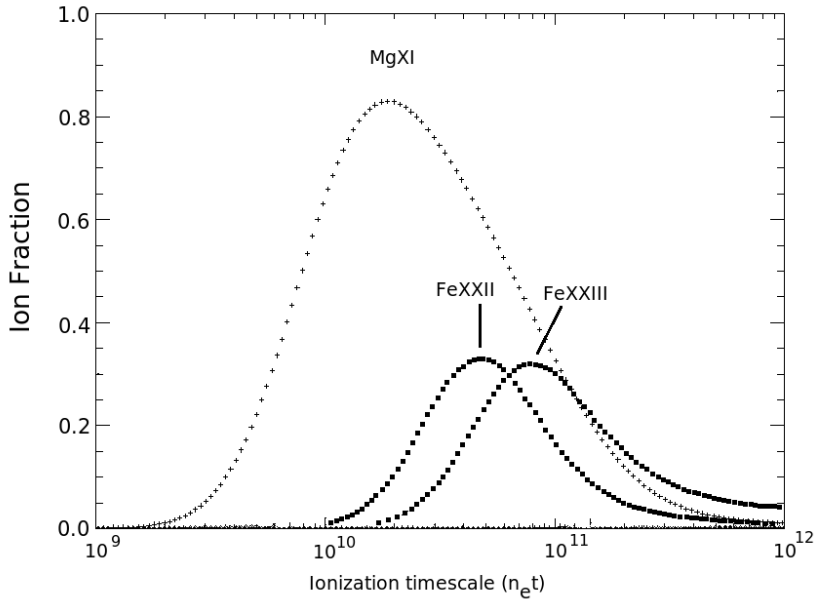

Figure 4.7: Ionization fraction of Fe and Mg as a function of ionization timescale. Relevant lines are labeled. We note that we should not observe Fe XXII/XXIII and Mg XI increasing in strength at the same time and place if the two ions are at the same ionization timescale. We should also not observe Fe XXII/XXIII becoming weaker while Mg XI is becoming stronger (Mazzotta et al. 1998).

routine (private communication, C. Badenes) that is a translation of a FORTRAN program described in Mazzotta et al. (1998). The ionization fraction for all ions as a function of ionization timescale was determined by iteratively calculating the ionization rates for ionization timescales incremented from 0 to about 1x10^{12} cm^{-3} s.

If the Mg and Fe have the same ionization timescale, we should see the Fe XXII/XXIII and Mg XI lines decreasing in strength at the same time, or the Mg XI line decreasing in strength while the Fe XXII/XXIII lines increases in strength. However, there are two patterns of change that we should not observe if the Mg XI and Fe XXII/XXIII lines have the same ionization timescale. We should not observe both the Mg and Fe lines increasing in intensity at the same location, nor should we observe the Mg XI line increasing while the Fe XXII/XXIII line is decreasing in strength. Therefore, we will attempt to identify regions which have one of those patterns in order to accomplish our goal of observing spatially overlapping knots with different ionization timescales. These possible combinations of spectral changes between the two elements are summarized in Table 4.2.

Typical electron temperatures for knots near the reverse shock range from 1-2.5 keV (e.g. Hwang & Laming 2009). Therefore, we adopt a standard temperature of 1.5 keV for our ion fraction model described in the previous paragraphs. We note that assuming any temperature between 1 and 2.5 keV does not change our conclusions. In general, the ionization state of an element is only mildly sensitive to electron temperature (Flanagan et al. 2004) - a higher temperature will cause more collisions per unit time, which leads to a higher ionization state at a given time (e.g. Smith et al. 2009), but does not qualitatively change the overall picture.

Table 4.2: Potential changes in Mg and Fe line strengths under the assumption that the ionization timescale is the same for both lines (see §3.2 and Figure 4.7).

Change in Mg XI	Change in Fe XXII/XXIII	Model
Increase	Increase	Forbidden
Increase	Decrease	Forbidden
Decrease	Increase	Allowed
Decrease	Decrease	Allowed

4.3.3 Line Strength Changes

In order to detect the changes described in the previous section, we made energy cut maps both the 2000 and 2004 epochs. The energy cuts were from 1.01-1.08 keV for the Fe XXII/XXIII line and from 1.31-1.41 keV for the Mg XI line (see Figure 4.6). We then normalized each of the band maps to contain an equal number of counts. The 2000 maps were subtracted from the 2004 maps for each energy cut and convolved to $5''$ to make difference maps. We display the Fe XXIII/XXIII difference map as red and the Mg XI difference map as green in the RG plots of magnified regions of Cas A shown in Figures 4.9 and 4.10. The location of these regions with respect to the entire remnant is shown in Figure 4.8. In most locations, we see either an increase in Fe XXII/XXIII or Mg XI, but not an increase in both lines. However, we are interested in finding regions that show increases in *both* colors, which would be inconsistent with a single ionization timescale. We identify 7 such regions and indicate their locations in Figures 4.8, 4.9, and 4.10. Typical fractional changes in line strengths for these regions are $>$15%, substantially larger than the 7% changes seen in the control regions.

We then searched for regions that showed a decrease in the Fe XXII/XXIII line strength but an increase in Mg XI since that is also not expected for regions at a single ionization timescale. This was accomplished by multiplying the convolved and normalized Fe XXII/XXIII difference map by -1 and displaying the maps using the same techniques as described in the previous paragraphs. We found no regions with this pattern of change.

Our energy cuts centered on Fe XXII/XXIII and Mg XI might be contaminated by nearby lines. Therefore, we always perform followup spectroscopy on regions of interest to make sure that we are not being confused by contamination from nearby lines (see §4.2.3 for more detail).

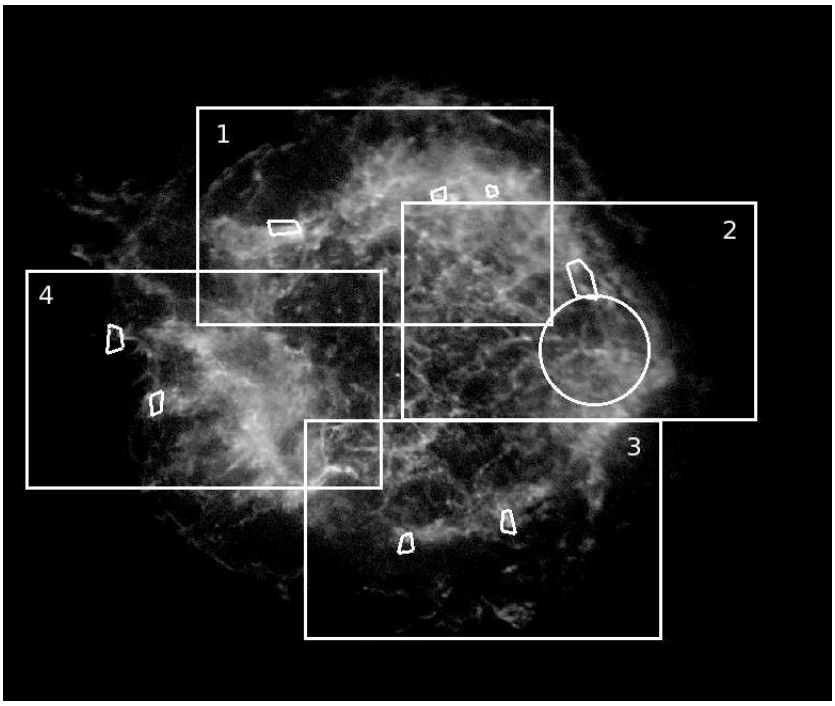

Figure 4.8: 0.3-10 keV Chandra image with regions in which we observe Fe XXII/XXIII and Mg XI increasing in strength at the same time. The circular region indicates the randomly selected control region whose spectral changes we display in Figure 4.12. The large boxes indicate the fields of view for the images which make up Figures 4.9 and 4.10. The regions identified in Figures 4.9 and 4.10 as having increases in both Mg XI and Fe XXII/XXIII line strength are indicated by the irregular regions.

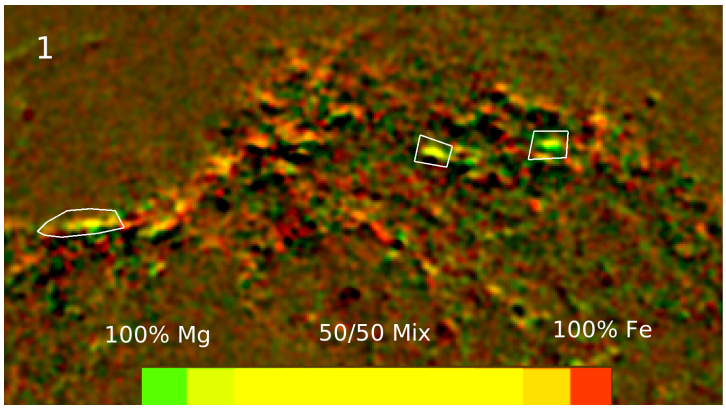

Figure 4.9: Close-up RG images of Fe (red) and Mg (green) changes from 2000 to 2004 convolved to 5″ for the northern region. The location of these frames with respect to the rest of the remnant is shown in Figure 4.8. Regions which show substantial change in both lines appear yellow and are indicated.

4.3.4 Follow-up Spectroscopy

We confirmed that the spectrum of each region picked out by the method described in §4.3.3 was consistent with a difference in ionization timescale between layers by performing follow-up spectroscopy. We extracted the spectrum from each region of interest for both the 2000 and 2004 epochs. The spectra were then normalized to the same number of counts in both epochs and subtracted to form a difference spectrum. The normalization accounts for the possibility of any compression in our regions. If a region is compressed, the strength of the lines and the continuum should increase by the same amount. We determined that the changes in our regions were not due to compression since the strength of the lines and the continuum increased by different fractional amounts.

We show such a difference spectrum from a randomly selected portion of the remnant of average brightness in Figure 4.11. This spectrum shows that overall there is very little change in the Mg XI and Fe XXII/XXIII lines. By contrast, we do observe increases in strength in both the Fe XXII/XXIII and Mg XI lines in the 7 regions identified by observing changes in the energy cuts as described in the previous section. We show an example difference spectrum from one of these regions in Figure 4.12. Special care was taken to make sure that any changes near 1.35 keV were due to Mg XI line strength

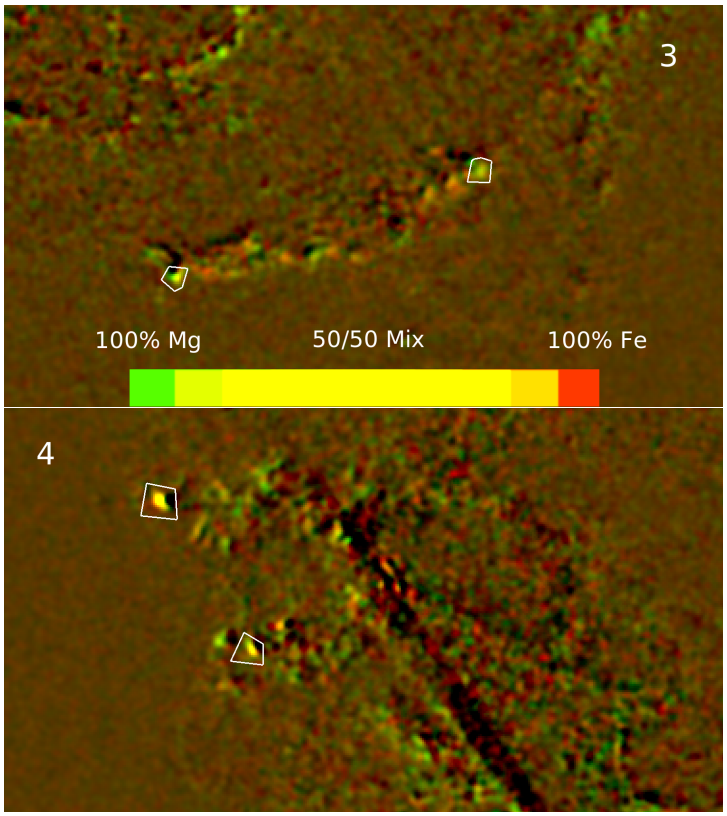

Figure 4.10: Close-up RG images of Fe (red) and Mg (green) changes from 2000 to 2004 convolved to 5″ for the southern regions. The location of these regions with respect to the rest of the remnant is shown in Figure 4.8. Regions which show substantial change in both lines appear yellow and are indicated.

changes and not the ∼1.25 keV Fe XXI line by making sure that the residual drops off at 1.35 keV instead of beyond 1.4 keV (see §4.2.3).

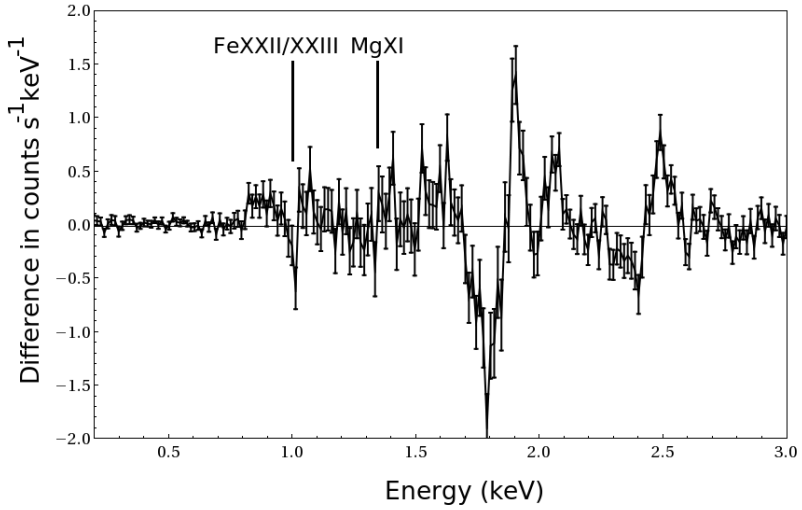

Figure 4.11: Difference spectrum of the randomly selected control region whose location is indicated in Figure 4.8. We see no substantial change in the line strength of the Mg XI line. The small change near the Fe XXII/XXIII line is indicative of a small change in ionization timescale, but not a change in the overall strength of the line. The large changes near 2.0 keV and 2.5 keV are consistent with changes in ionization timescale in the Si and S lines respectively.

4.3.5 Proper Motion

Large proper motions in the ejecta could cause spurious detections of increases or decreases in all line strengths, including both Mg XI and Fe XXII/XXIII, for individual pixels. However, we note that the ejecta will only move by a fraction of a pixel over the 4 year baseline of our observations. In order to make sure that we are not being confused by proper motions, we made sure that all regions in which we observed spectral changes included at least 4 pixels in each dimension. Additionally, our spectra will be dominated by changes not associated with proper motion since the extraction regions for our follow-up spectroscopy is much larger than any proper motion.

4.3.6 Projection Effects

A complication arises in that we may be observing Fe and Mg emission that are only projected onto the same line of sight and not spatially coincident. We can rule out large differences in Doppler velocities with spectral fits. We fit the Mg and Fe lines independently with the VNEI+PHABS model described in §4.2.1, allowing the redshift to vary in each spectral fit. We then compare the redshift of both lines. We find identical redshifts within the uncertainties of our fit in all 7 regions of interest. We note, however, that the uncertainties in redshift are typically ∼1000 km/sec.

However, if we observe separation, then this represents physical separation even in the case of confusion from projection effects. If Mg and Fe are spatially coincident, we should always observe Fe XXII/XXIII emission paired with Mg XI emission as seen in 4.7. So even if we are observing the Fe and Mg ions at two different Doppler velocities projected onto the same line of sight, we are still observing a separation between the layers.

4.3.7 The Southwest

We briefly explored the possibility of looking for a separation between the Si/S and Mg/O layers by comparing an energy cut map of the Si XIII (He-like Si) emission from 1.75-1.90 keV from the 2000 data to the corresponding Mg XI map. The maps were normalized such that there were an equal number of counts in each map and convolved to 5″. Most regions show no clear spatial separation between layers. However, in the Southwest we observe clear differentiation between elements since the Mg emission appears to be at greater radii than the Si emission. The location of this region is shown in Figure 4.1. A closeup of this region is shown in Figure 4.13.

We show the ionization state as a function of ionization timescale for the relevant lines in Figure 4.14. Since several patterns of change are consistent with Mg and Si having the same ionization timescale (and therefore having no velocity separation), these lines cannot provide a diagnostic for separation between the Si and Mg lines using the techniques described in §4.3.2.

We extracted spectra from the two concentric regions shown in Figure 4.13. As shown in Figure 4.15, the region at the larger radius clearly has stronger Mg emission

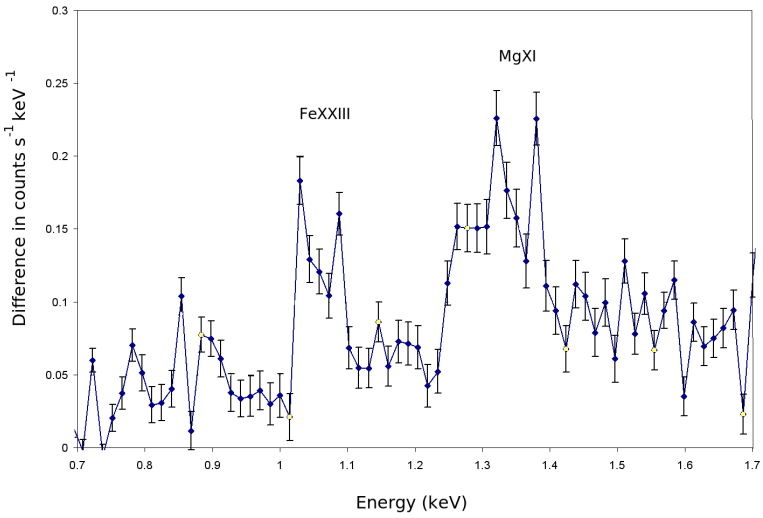

Figure 4.12: Difference spectrum of example region of interest located near (23:23:36.17, 58:50:08.3). We observe substantial increases in both the Mg XI and Fe XXII/XXIII line strengths. There is a substantial positive residual at energies below 1.40 keV, indicating that it is due to changes in the Mg XI line strength (see §4.3.4).

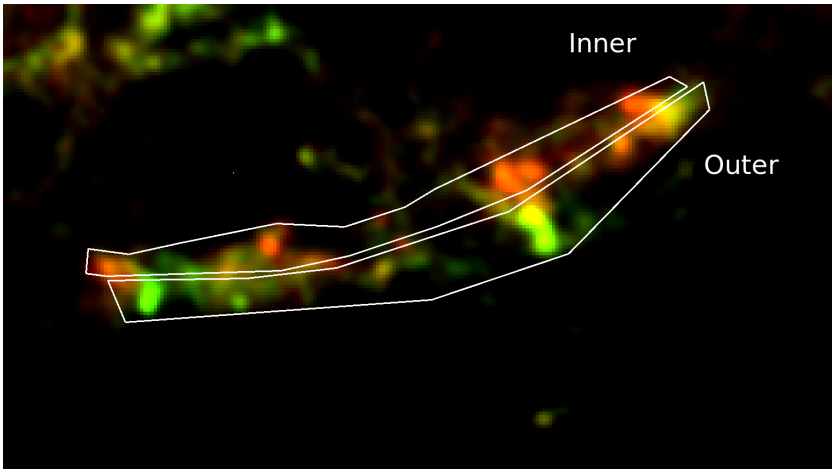

Figure 4.13: Map of Si (red) and Mg (green) emission from the 2000 epoch observation convolved to 5″ in the Southwest. We note clear differentiation between the Mg and Si emission. The field of view in this image with respect to the rest of the remnant is indicated in Figure 4.1. The regions from which we extract spectra are indicated.

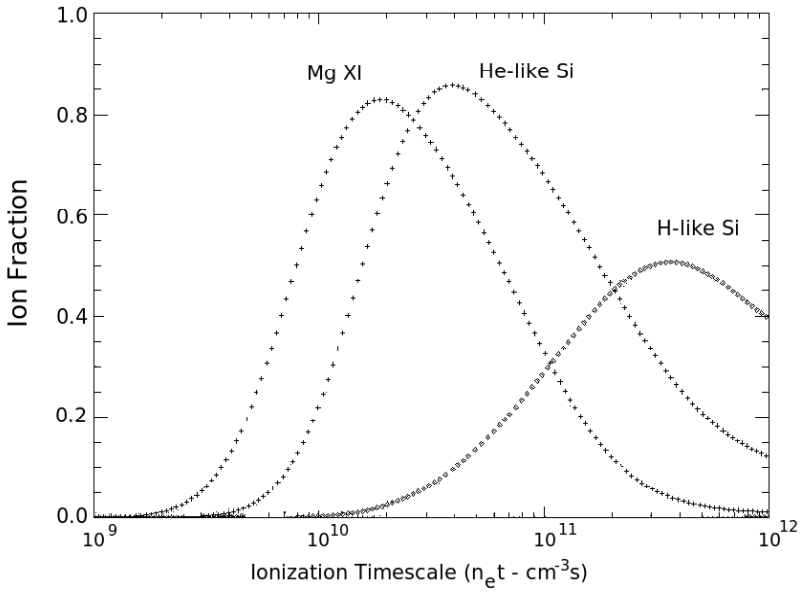

Figure 4.14: Ion fraction for the relevant Mg and Si ions assuming a temperature of 1.5 keV from the models described in §4.3.2. Note that the Mg reaches the observable ionization state at smaller ionization timescales than Si.

compared to the Si emission. This is inconsistent with the Mg and Si layers reaching the reverse shock at the same time. As shown in Figure 4.14, Mg should reach its visible Mg XI state at lower ionization timescales than when Si should reach its visible Si XIII state. Thus, we expect to observe Si at larger radii than Mg if Mg and Si were at the same ionization timescale, but instead we observe Mg at larger radii than Si in the southwest. This implies that the Mg is traveling at a larger velocity than Si in the southwest.

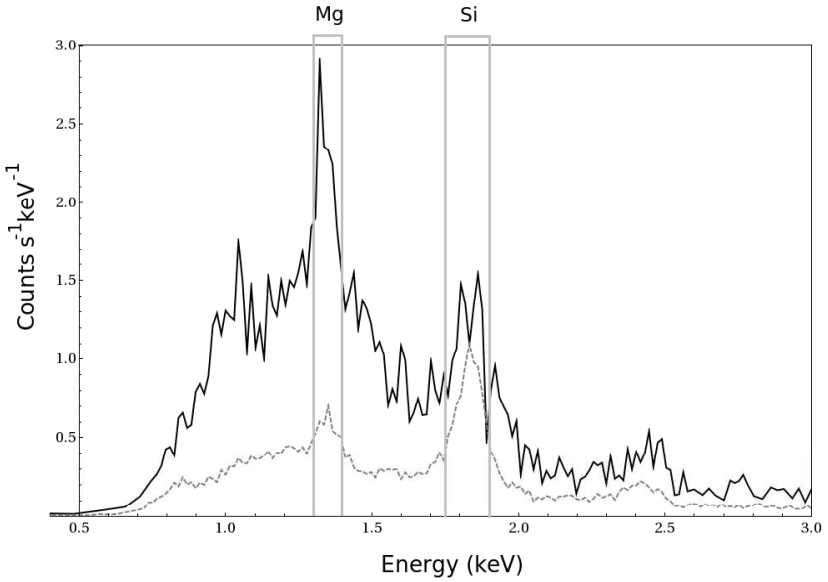

Figure 4.15: Spectra of concentric southwest regions indicated in Figure 4.13. The spectral ranges used for making our energy cut maps are indicated. The inner radius spectrum is indicated by the dashed gray line, while the outer radius spectrum is indicated by the solid black line. The spectra are normalized such that there are an equal number of counts at 1.83 keV, the approximate center of the Silicon line complex. Mg emission is relatively strong at larger radii in this direction.

We have found differences between nucleosynthetic layers using several different techniques. We find differences in ionization timescale between Mg and Fe in 7 small regions by observing changes in line strength between the 2000 and 2004 images. We also identified spatial separation between the Mg and Si layers in one larger region of the remnant. We discuss the implications of these findings in the next section.

4.4 Discussion

4.4.1 Separation of Layers During the Supernova Explosion

If two layers are at the same spatial location in the current epoch, we expect them to have similar electron densities and to be shocked at the same time. Therefore, if we observe spectral changes that are inconsistent with similar ionization timescales for the two layers, we know that there must currently be a spatial separation between the layers. As argued in §4.1.2, this separation cannot be the initial separation between the nucleosynthetic layers, but must arise after the explosion due to velocity gradients between the layers. This velocity separation is not easily observed with other techniques such as observing a spatial separation between layers due to confusion by projection effects or a lack of adequate spatial resolution.

Our results confirm and extend the results from previous studies that indicate that in most directions, the nucleosynthetic layers have nearly identical velocities (within $\sim$100 km s^{-1}), but in some directions they are separated by hundreds of kilometers per second (Fesen et al. 2006). Because a knot must be traveling at roughly 5000 km/s in order to be currently encountering the reverse shock, we estimate that a velocity separation of at least 100 km/s is needed in order for the layers to be arriving at least 4 years apart. This is of the same order of magnitude as what was observed in IR ejecta that have not yet encountered the reverse shock; Isensee et al. (2010) report separations up to 500 km s^{-1} from high resolution Spitzer data.

Current models predict velocity separations of 0-2000 km/s between nucleosynthetic layers, but azimuthally average the velocity of the ejecta over the whole star (e.g. Joggerst et al. 2009; Kifonidis et al. 2006). However, many models do predict great variability in the behavior of the layers as a function of direction (e.g. Hammer et al. 2010), so a difference in radial velocity structure that varies as a function of direction should not be surprising. Explicitly predicting the separation of layers as a function of direction would be useful in future models since it would allow them to be better tested against our observations.

We can detect a separation between the Mg and Fe layers if the two elements are in the correction ionization state to be observed. However, most of the Mg and Fe present in the remnant are probably in the wrong ionization state to be observed in the X-ray

since the ejecta have not recently encountered the reverse shock. This makes it difficult to make statistical statements about the relative amounts of ejecta with significant velocity separation.

It is tempting to look in the IR for Fe and Mg that have not yet encountered the reverse shock since Si, S and O lines are detected in the IR from ejecta that have yet to be shocked (DeLaney et al. 2010; Isenee et al. 2010). However, there are no Mg lines at energies available to Spitzer, and Fe interior to the reverse shock is not detected in any of several possible ionization states in the IR for unexplained reasons (Isensee et al. 2010).

4.4.2 Spatial Mixing Mechanism

The term "mixing", as it is used in the literature, is an ambiguous one. Two nucleosynthetic layers can be observed to be spatially coincident in the current epoch *either* because they have been spatially mixed during the supernova explosion *or* because they emerge with the same velocity from the explosion, and therefore maintain their undetectably small initial separation. We note that when we observe a physical separation between layers at the current epoch, this means that there has not been spatial mixing and that there is a different velocity for each layer. In this paper we have also introduced another technique, i.e., using spectra to determine ionization timescale changes, to see whether two layers arrive at the shock at the same or different times.

When we see no physical separation between layers, and simultaneously see no spectral indications of differences in their velocities, then it is possible that the layers have actually been mixed during the explosion. There are two proposed mechanisms to cause such large scale mixing – partial explosive O burning (Chevalier & Kirshner 1979) or mixing between layers caused by large-scale Rayleigh-Taylor instability fingers created by shocks during the supernova explosion (Winkler et al. 1991).

The observation of Fe dominated X-ray emission exterior to emission from less dense layers (Hughes et al. 2000) has caused many groups to consider the Rayleigh-Taylor mechanism to be much more likely since there is no obvious way that variability in the degree of explosive O burning could cause the overturn of the Fe layer (Fesen et al. 2006). Isensee et al. (2010) create a 3D map of the interior ejecta of Cas A at relatively high spectral resolution. In some directions they observed filaments that have large

ranges in velocity - O filaments are observed both exterior and interior to Si filaments. This pattern of emission can only be explained with the Rayleigh-Taylor model since there is no known way for partial O burning to produce well separated O filaments both exterior and interior to Si filaments.

Our results confirm those of Isensee et al. (2010). In some directions we find velocity separations between the Mg/O and Si layers as well as between the Mg/O and Fe layers. In other directions, we observe both pairs of layers to be at similar velocities. The mixing of Mg and Fe layers cannot readily occur in a partial explosive burning scenario since O/Mg explosively burns to Si, not Ni/Fe. Therefore, it is much more likely that the variability in velocity differences between layers is caused by Rayleigh-Taylor filamentation.

4.4.3 Knot Evolution

Models predict changes in the physical properties of ejecta knots as they encounter a supernova's reverse shock and become heated and collisionally ionized (e.g. Patnaude & Fesen 2007; Borkowski et al. 2001). We have observed such changes, although a detailed comparison with models is not possible.

To date, nearly all models explicitly deal with the forward shock of a SNR (Ellison et al. 2005). Additionally, they do not generally predict the behavior of individual knots over time, but rather the relevant properties (ionization timescale and electron temperature) as a function of radial distance from the center of the remnant (e.g. Patnaude & Fesen 2007). This is a difficult prediction to test observationally since we experience a very strong selection effect in that we can only detect ejecta that have recently encountered the reverse shock.

The details of the evolution of recently shocked material in a SNR are uncertain for several reasons. The exact efficiency of energy transfer from the ions (which carry most of the energy) to the electrons is unknown (Borkowski et al. 2001). But the bigger question is that of cosmic ray acceleration. Cosmic rays can carry away a substantial fraction of the energy present in material encountering a shock (perhaps greater than half), although this process has never been demonstrated at a SNR's reverse shock. This energy loss should have a substantial effect on the evolution of the remnant as a whole, as well as individual knots of ejecta as they encounter the shock. For example,

the loss of energy to cosmic rays can cause compression ratios much greater than the factor of 4 expected for a strong shock (e.g. Patnaude et al. 2009).

We anticipate that future models will be able to predict the time-based evolution of individual knots at the reverse shock as more observations of well resolved remnants such as Cas A are made. In Table 4.1, we provide the key changes in the properties of the knots over time in anticipation of this future work.

4.5 Conclusions

We have built upon the previous work of DeLaney et al. (2010) and Isensee et al. (2010) by finding evidence of a separation of nucleosynthetic layers in the X-ray in some, but not most, directions. We attribute this to both velocity gradients and Rayleigh-Taylor instabilities in the supernova explosion itself. We have also identified regions that have encountered the reverse shock very recently, and observe the changes in key physical properties of these regions.

This work could be improved upon with a second epoch of high resolution grating images from Chandra similar to the work of (Lazendic et al. 2006). This would allow the comparison of changes in many more lines due to the superior spectral resolution. Lines of special interest would be the Ne and O lines at about 1.5 and 0.8 keV respectively, which are difficult to work with at lower resolution due to the blending of nearby lines. Furthermore, projection effects would be less of an issue since the superior spectral resolution would better allow us to more accurately determine the redshifts of the relevant lines.

Chapter 5

Conclusion and Discussion

In this thesis we have presented a series of new infrared spectral maps of Cas A, and performed a new analysis of *Chandra* X-ray data. We identify the following primary results:

- We created 3D maps of select parts of Cas A for O, Si, S, and Fe lines. Ejecta which both have and have not been recently shocked were identified.
- The ejecta can form a variety of different geometric 3D structures, including sheets, filaments, and shells.
- The reverse shock of the remnant is spherical to within 7%.
- Si and O are observed to be separated by $\sim$500 km s^{-1} in some directions, but are coincident in most regions.
- Ejecta traveling toward us are, on average, $\sim$800 km s^{-1} slower than ejecta traveling away from us.
- The velocity width of the nucleosynthetic layers is $\sim$1000 km s^{-1} averaged over the entire central, SE, and SW regions, although the velocity width of a layer along an individual line of sight is $<$250 km s^{-1}.
- We observe small-scale velocity structures in the recently shocked ejecta. This corrugation is likely caused during the supernova explosion itself, rather than at the remnant's reverse shock.

- We compare our observations to recent supernova explosion models and find that no single model can simultaneously reproduce all the observed features. However, models of different supernova explosions can collectively produce the observed geometries and structures of the interior emission.

- The back surface of Cas A will begin brightening in ∼30 years, and the front surface in ∼100 years.

- We identify the most recently shocked X-ray ejecta with ionization timescales of ∼1x10^{10} cm^{-3} s, nearly an order of magnitude smaller than previously identified shocked ejecta.

- Several regions which have a spectral signature consistent with a velocity separation of ∼200 km s^{-1} between layers, although we find that most regions show no sign of separation greater than 65 km s^{-1}.

- We find one large region where Mg is traveling at a greater velocity than the Si layer.

- Any mixing between nucleosynthetic layers is most likely caused by Rayleigh-Taylor filamentation and not partial explosive nucleosynthesis.

5.1 Future Observations

The recent launch of the Herschel Space Telescope and the Stratospheric Observatory for Infrared Astronomy (SOFIA) provide the opportunity for exciting extensions of the work presented in this thesis. Both observatories have imaging spectrometers with superior spectral resolution, different operational wavelengths, and in the case of Herschel, substantially superior sensitivity to Spitzer. An issue with these instruments is that they lack the necessary instantaneous bandwidth to efficiently create spectral cubes of Cas A. Typical instantaneous bandwidths are ≤1000 km s^{-1}, while we need to sample a velocity range of ≥10,000 km s^{-1} in order to observe all the ejecta in Cas A. However, both observatories will soon implement scanning modes on their spectrometers, which should allow the efficient scanning of the necessary wavelength ranges.

The superior sensitivity and spectral resolution of these instruments would allow us to address several key questions related to Cas A. We would be able to better constrain the separation between nucleosynthetic layers and the width of individual layers. This would allow more accurate comparisons to supernova explosion models. We would also be able to better observe Fe lines, especially in the interior of the remnant. As discussed in Chapter 2, we do not observe substantial Fe in the interior of Cas A despite the fact that several lines are within our wavelength range. We believe that this is because the Fe is at too low a density to be easily observable. Observations from more sensitive instruments will be able to confirm or refute this hypothesis. Additionally, we will learn more about the interior conditions of the supernova explosion by observing interior Fe. We know, from models, the approximate pre-explosion density ratio between Fe and Si. If we could constrain the post-explosion Fe to Si density ratios in material that has not yet reached the Remnant Reverse Shock, we could determine how much the density of the Fe and Si were changed during the explosion itself. This would help us address issues such as the role of the Explosion Reverse Shock in modifying the structure of the star as it explodes.

More sensitive observations will also allow us to determine a larger fraction of the ejecta density distribution. We likely only sample the very densest material with our Spitzer observations. These ejecta were almost certainly strongly affected by Rayleigh-Taylor instabilities. Are these ejecta representative of all ejecta in Cas A, including those which have not been greatly affected by instabilities? We should be able to begin to address this important question with Herschel.

We could also create 3-dimensional maps of other young, easily resolved supernova remnants. The Tycho and Kepler supernova remnants are especially appealing targets. They are the result of Type Ia explosions, and comparing their 3-dimensional geometry to that of a core collapse supernova would be interesting. Models predict that we will not see as many large scale asymmetries in Type Ia explosions as compared to core collapse supernovae. To date, observations seem to support the models. For example, spectropolarimetric observations of Type Ia supernovae do not show nearly as much polarization, indicative of large asymmetries, as is observed in core collapse supernovae. But testing the degree of asymmetry in a supernova remnant is important since we have not observed a Type Ia supernova in our own galaxy in modern astronomy.

Finally, we can also create 3-dimensional maps in the X-ray. Chandra's High Resolution spectral grating has been used to create high resolution spectra of a handful of knots. These instruments have the spectral resolution necessary to accurately determine the Doppler velocities of the ejecta. Select areas of the remnant could be mapped using this instrument. It would be especially useful if we mapped regions from which we already had 3-dimensional infrared maps, so that we could compare the 3-dimensional structure of X-ray ejecta to that of the infrared ejecta.

5.2 Future Theory

On the reverse shock, we can use the 18.7μm and 33.48μm [S III] lines to determine the density of the ejecta as long as the ejecta have a density >100 e^- cm^{-3}. However, we cannot use the same line ratio in the interior of the remnant because the ejecta there are photoionized and beneath the lower density limit of the [S III] test. We need the appropriate photoionization models, which predict the strength of S and Si lines as a function of density, so that we can use observed line ratios as a density diagnostic.

A measurement of the interior density of Cas A is crucial because we have determined both the pre- and post-shock densities of the ejecta. A typical strong, adiabatic shock should have a pre to post-shock ratio of 1/4, but such a ratio can be modified by energy losses in practice. We could, in principle, indirectly detect cosmic ray production for the first time at a supernova remnant's reverse shock if we detected enhancements in density above that expected from a strong shock combined with radiative losses.

5.3 Funding

This work is based on observations made with the Spitzer Space Telescope, which is operated by the Jet Propulsion Laboratory, California Institute of Technology under NASA contract 1407. Additional funding for this work was provided by NASA/SAO Award No. AR5-6008X and NASA/JPL through award 1265552 to the University of Minnesota.

Chapter 6

References

Abdo, A.A., et al. (The Fermi LAT Collaboration) 2010, ApJL, 710, L92-L97

Anderson, M.C. & Rudnick, L. 1995, ApJ, 441, 307

Abrikosov, A.A. 1960, Sov. Phys. JETP, 12, 1254

Bell, A.R. 1978, MNRAS, 182, 147

Berezhko, E. G. & Ellison, D. C. 1999, ApJ, 526, 385

Bertschinger, E. 1986, ApJ, 304, 154

Bisnovatyi-Kogan, G. S., & Blinnikov, S. I. 1982, SvA, 26, 530

Blair, W. P., Morse, J. A., Raymond, J. C., Kirshner, R. P., Hughes, J. P., Dopita, M. A., Sutherland, R. S., Long, K. S., & Winkler, P. F. 2000, ApJ, 537, 667

Blinnikov, S.I., Dunina-Barkovskaya, N.V., & Nadayozhin, D.K. 1996, ApJS, 106, 118

Blondin, J.M., Mezzacappa, A., & DeMarino, C. 2003, ApJ, 584, 971

Borkowski, K. J., Lyerly, W. J., & Reynolds, S. P. 2001, ApJ, 548, 820

Braun, R. 1987, A&A, 171, 233

Burrows, A., Dessart, L., Ott, C. D., & Livne, E. 2007, PhR, 442, 23

Chatterjee, S. et al. 2005, ApJ, 630, L61

Chakrabarty, D., Pivovaroff, M.J., Hernquist, L.E., Heyl, J.S., & Narayan, R. 2001, ApJ, 548, 800

Chevalier, R. A., & Kirshner, R. P. 1978, ApJ, 219, 931

Chevalier, R. A., & Kirshner, R. P. 1979, ApJ, 233, 154

Chevalier, R. A., & Oishi, J. 2003, ApJ, 593L, 23

Chevalier, R. A., & Soker, N. 1989, ApJ, 341, 867

DeLaney, T.A, & Rudnick, L. 2003, ApJ, 589, 818

DeLaney, T.A. 2004, "A Multiwavelength Study of Cassiopeia A and Kepler's Supernova Remnants", Ph.D. thesis, University of Minnesota

DeLaney, T.A., Rudnick, L., Stage, M.D., Smith, J.D., Isensee, K., Rho, J., Allen, G.E., Gomez, H., Kozasa, T., Reach, W.T., Davis, J.E., & Houck, J.C. 2010, ApJ, 725, 2038

Ding, Y., Li, Z., & Diwu, Y. 1999, ChA&A, 23, 484

Douvion, T., Lagage, P. O., & Cesarsky, C. J. 1999, A&A, 352, L111

Ellison, D. C., Decourchelle, A., & Ballet, J. 2005, A&A, 429, 569

Ennis, J. A., Rudnick, L., Reach, W. T., Smith, J. D., Rho, J., DeLaney, T., Gomez, H., & Kozasa, T. 2006, ApJ, 652, 376

Eriksen, K. A., Arnett, D., McCarthy, D.W., & Young, P. 2009, ApJ, 697, 29

Feuchtgruber, H. et al. 1997, ApJ, 487, 962

Fesen, R. A. & Gunderson, K. S. 1996, ApJ, 470, 967

Fesen, R. A., Hammell, M. C.,Morse, J., Chevalier, R. A., Borkowski, K. J., Dopita, M. A., Gerardy, C. L., Lawrence, S. S., Raymond, J. C., & van den Bergh, S. 2006, ApJ, 645, 283

Fesen, R.A. 2001, ApJS, 133, 161

Fesen, R. A., Morse, J. A., Chevalier, R. A., Borkowski, K. J., Gerardy, C. L., Lawrence, S. S., & van den Bergh, S. 2001, AJ, 122, 2644

Flanagan, K. A., Canizares, C. R., Dewey, D., Houck, J. C., Fredericks, A. C., Schattenburg, M. L., Markert, T. H., & Davis, D. S. 2004 ApJ, 605, 230

Froese Fischer, C. 1983, J. Phys. B, 16, 157

Fryer, C. L., & Heger, A. 2000, ApJ, 541, 1033

Gotthelf, E. V., Koralesky, B., Rudnick, L., Jones, T. W., Hwang, U., & Petre, R. 2001, ApJ, 552, L39

Hamilton, A. J. S. & Sarazin, C. L. 1984, ApJ, 287, 282

Hamilton, A. J. S. & Fesen, R. A. 1998, ApJ, 327, 178

Hammer, N. J., Janka, H.-Th., & Mller, E. 2010, ApJ, 714, 1371

Heger, A., & Langer, N. 2000, ApJ, 544, 1016

Herant, M., & Woosley, S.E. 1994, ApJ, 425, 814

Hughes, J. P., Rakowski, C. E., Burrows, D. N., & Slane, P. O. 2000, ApJ, 528, L109

Hwang, U., Holt, S. S., & Petre, R. 2000, ApJ, 537, L119

Hwang, U., & Laming, J. M. 2003, ApJ, 597, 362

Hwang, U., et al. 2004, ApJ, 615, L117

Iglesias, F.A. & Rogers, F.J. 1996, ApJS, 464, 943

Isensee, K., Rudnick, L., DeLaney, T.A., Smith, J. D., Rho, J., Reach, W. T., Kozasa, T., & Gomez, H. 2010, ApJ, 725, 2059

Itoh, N., Hayashi, H., Nishikawa, A., & Kohyama, Y. 1996, ApJS, 102, 411

Janka, H.-Th., Langanke, K., Marek, A., Martnez-Pinedo, G., & Mller, B. 2007, PhR, 442,38

Joggerst, C.C., Woosley, S.E., & Heger, A. 2009, ApJ, 693, 1780

Jones, F. C. & Ellison, D. C. 1991, Space Sci. Rev., 58, 259

Kassim, N. E., Perley, R. A., Dwarakanath, K. S., & Erickson, W. C. 1995, ApJ, 455, L59

Heger, A., Woosley, S. E., Langanke, K., Kolbe, E., Rauscher, T., & Hoffman, R. D. 2003, NuPhA, 718, 159

Khokhlov, A. M., Hflich, P. A., Oran, E. S., Wheeler, J. C., Wang, L., & Chtchelkanova, A. Yu. 1999, ApJ, 524L, 107

Kidonidis, K., et al. 2006, A&A, 453, 661

Krause, O., Birkmann, S.M., Usuda, T., Hattori, T., Goto, M., Rieke, G. H., & Misselt, K. A. 2008, Science, 320, 1195

Laming, J. M., & Hwang, U. 2003, ApJ, 597, 347

Laming, J. M., Hwang, U., Radics, B., Lekli, G., & Takcs, E. 2006, ApJ, 644, 260

Lawrence, S. S., MacAlpine, G. M., Uomoto, A., Woodgate, B. E., Brown, L. W., Oliverson, R. J., Lowenthal, J. D., & Liu, C. 1995, AJ, 109, 2635

Lazendic, J. S., Dewey, D., Schulz, N. S., & Canizares, C. R. 2006, ApJ, 651, 250

Lequeux, J. 2005, *The Interstellar Medium*, Springer, Berlin

Long, K. S., Reynolds, S. P., Raymond, J. C., Winkler, P. F., Dyer, K. K., & Petre, R. 2003, ApJ, 586, 1162

Markert, T. H., Clark, G. W., Winkler, P. F., & Canizares, C. R. 1983, ApJ, 269, 134

Mazzotta, P., Mazzitelli, G., Colafrancesco, S., & Vittorio, N. 1998, A&AS, 133, 403

Miles, A.R. 2009, ApJ, 696, 498

Morse, J. A., Fesen, R. A., Chevalier, R. A., Borkowski, K. J., Gerardy, C. L., Lawrence, S. S., & van den Bergh, S. 2004, ApJ, 614, 727

Osterbrock, D.E. 1989, *Astrophysics of Gaseous Nebulae and Active Galactic Nuclei*, (Sausalito, California: University Science Books)

Osterbrock, D. E. & Ferland, G. J. 2006, Astrophysics of Gaseous Nebulae and Active Galactic Nuclei, 2nd. ed. (Sausalito, CA: Univ. Sci. Books)

Patnaude, D. J., Ellison, D. C., & Slane, P. 2009, ApJ, 696, 1956

Patnaude, D.J., & Fesen, R.A. 2007, AJ, 133, 147

Reed, J. E., Hester, J. J., Fabian, A. C., & Winkler, P. F. 1995, ApJ, 440, 706

Raymond, J.C. 2003, RevMexAA, 15, 258

Reynolds, S. P., Borkowski, Kazimierz K.J., Green, D. A., Hwang, U., Harrus, I., Petre, R.A. 2008, ApJ, 680L, 41

Rho, J., Kozasa, T., Reach, W. T., Smith, J. D., Rudnick, L., DeLaney, T., Ennis, J. A., Gomez, H., Tappe, A. 2009, ApJ, 673, 271

Rogers, F.J. & Iglesias, C.A. 1992, ApJS, 79, 507

Satterfield, J., DeLaney, T., Chatterjee, S. 2011, AAS Poster, 21725615S

Sedov, L.I. 1959, *Similarity and Dimensional Methods in Mechanics*, Academic Press, New York

Shklovskii, I. S. 1969, AZh, 46, 715

Smith, J. D., Armus, L., Dale, D. A., Roussel, H., Sheth, K., Buckalew, B. A., Jarrett, T. H., Helou, G., Kennicutt, R. C., Jr. 2007, PASP, 119, 1133

Smith, J. D., Rudnick, L., DeLaney, T.A., Rho, J., Gomez, H., Kozasa, T., Reach, W.T., Isensee, K.A 2009, ApJ, 693, 713

Tananbaum, H. 1999, IAU Circ. 7246

Thorstensen, J. R., Fesen, R. A., & van den Bergh, S. 2001, AJ, 122, 297

Timmes, F.X. & Swesty, F.D. 2000 ApJS, 126, 501

Vink, J., Kaastra, J. S., Bleeker, J. A. M. 1996, A&A, 307L, 41

Vishniac, E. T. 1983, ApJ, 274, 152

Wang, L., & Chevalier, R.A. 2001, ApJ, 549, 1119

Wang, L., & Wheeler, J. C. 2008, ARA&A, 46, 433

Wheeler, J. C., Akiyama, S., & Williams, P. T. 2005, Ap&SS, 298, 3

Wheeler, J. C., Maund, J.R., & Couch, S.M. 2008, ApJ, 677, 1091

Willingale, R. Bleeker, J. A. M., van der Heyden, K. J., Kaastra, J. S., & Vink, J. 2002, A&A, 381, 1039

Willingale, R., Bleeker, J. A. M., van der Heyden, K. J., & Kaastra, J. S. 2003, A&A, 398, 1021

Winkler, P. F., & Kirshner, R. P. 1985, ApJ, 299, 981

Winkler, P.F., Roberts, P.F., & Kirshner R.P. 1991, in Supernovae: The Tenth Santa Cruz Summer Workshop in Astronomy and Astrophysics, ed. S.E. Woosley (New York:Springer), 652

Winkler, P. F., & Long, K. S. 1997, ApJ, 491, 829

Woosley, S.E., Heger, A., & Weaver, T.A. 2002, RvMP, 74, 1015

Young, P. A., Fryer, C. L., Hungerford, A., Arnett, D., Rockefeller, G., Timmes, F. X., Voit, B., Meakin, C., & Eriksen, K. A. 2006, ApJ, 640, 891